NAM

Evolution of induced earthquake magnitude distributions with increasing stress in the Groningen gas field

Stephen Bourne and Steve Oates

Datum November 2019

Editors Jan van Elk & Dirk Doornhof

General Introduction

As part of the NAM-led studies program into induced seismicity in Groningen, a number of seismological models have been prepared for the Groningen gas field. In 2013, a strain-partitioning seismological model (SM V1) was presented in the technical addendum to the winningsplan 2013 (Ref. 1). This model is further described in a scientific peer-reviewed paper published in the Journal of Geophysical Research (Ref. 2). This model was used in the hazard assessment of Winningsplan 2013 (Ref. 3).

In 2015, as an alternative seismological model, the activity rate model (SM V2), was introduced (Ref. 4 and 5). Like the strain-partitioning seismological model, the new activity rate model was based on a statistical analysis of the historical earthquake record of Groningen, in combination with the measured subsidence. Both the strain-partitioning seismological model and the alternative activity rate seismological model have been reviewed by Ian Main, Professor Seismology & Rock Physics at the University of Edinburgh. The activity rate model was described in two scientific papers (Ref. 6 and 7). To be able to implement the new model in the hazard and risk assessment, the distribution of pareto sums needs to be computed. A new method using Laplace Transformation and the Stehfest inversion was developed to do this efficiently (Ref. 8 and 9). The activity rate model has been used in the hazard and risk assessment of November 2015 (Ref. 10) and winningsplan 2016 (Ref. 11).

Alternative seismological models were developed using two approaches; (1) geomechanical / statistical method and (2) machine learning. The effort to develop a seismological model using machine learning has been documented in reference 12 and 13. Although innovative methods were developed to forecasts seismicity in the Groningen field, the machine learning approach did not lead to an improved seismological model.

Based on geomechanical principles, a set of different seismological models based on extreme threshold failures off a thin-sheet were developed. These were trained on the earthquake catalogue until 2012. Based on their ability to forecast the earthquake record for the period 2012 to 2017 the best performing model was chosen for implementation into the hazard and risk assessment (SM V5). This was documented in two scientific papers (Ref. 14 and 15), which are also available in a reader (Fig. 16). Using Gaussian Process Optimisation an attempt was made to further improve the elastic thin-sheet seismological model (Ref. 17). This hazard and risk model (SM V5) was used in the hazard and risk assessment for the production schedule Basispad Kabinet in 2018 (Ref. 18) production schedule GTS-raming in 2019 (Ref. 19).

A number of studies were performed to test the hypothesis that apart from the gas volume produced, also the gas extraction rate impacts the seismic event rate (Ref. 20 to 23). Both statistical/geomechanical and machine learning approached showed the available data did not support this hypothesis. Due to the limited size of the seismic record for Groningen, the possibility of a limited effect cannot be excluded.

The development of the seismological model had to this point primarily focused on the forecasting of the spatial and temporal development of earthquake events. For the forecasting of the frequency-magnitude relationship a power law (Gutenberg-Richter) with a b-factor was used. The seismic catalogue for the Groningen field is relatively small compared to other seismically active regions. A maximum likelihood

estimate for the b-factor for the complete earthquake catalogue and for spatial and temporal sub-sets was estimated. The analysis of the maximum likelihood estimate for the b-factor indicates the b-factor varies over the field (Ref. 24). Another study investigated the correlation dimension of clusters of seismic events (Ref. 25).

These studies led to a renewed interest in the frequency-magnitude relationship. A foundational study for this effort investigated fibre-bundle models (Ref. 26). Insights from this study and other statistical mechanical theories of brittle failure within heterogeneous media, statistical seismology, and acoustic emissions experiments indicate the pure power-law may contain a stress dependent exponential taper. Incorporating such an exponential taper in the seismological model for Groningen improved its forecasting performance. The current report reviews the existing theoretical and observational evidence for a stress-dependent exponential taper to motivate a range of alternative frequency-magnitude models suitable for induced seismicity hazard and risk analysis. For a set of different models the forecast performance was assessed using Bayesian inference, hindcast evaluations and forward-model simulations. This shows that the stress-dependent taper model with constant b-factor likely offers higher performance forecasts, than the stress-dependent b-models.

References

1. Technical Addendum to the Winningsplan Groningen 2013 - Subsidence, Induced Earthquakes and Seismic Hazard Analysis in the Groningen Field and Supplementary information to the "Technical Addendum of the Winningsplan Groningen 2013, Jan van Elk, Dirk Doornhof, Stephen Bourne, Steve Oates, Julian Bommer, Clemens Visser, Rob van Eijs and Peter van den Bogert, NAM, Shell and Imperial College, Dec 2013.
2. A seismological model for earthquakes induced by fluid extraction from a subsurface reservoir, Bourne S.J., Oates S.J., van Elk J., Doornhof. D., 2014, Journal of Geophysical Research: Solid Earth 119, 8991-9015.
3. Winningsplan Groningen gas field, 2013, NAM.
4. An activity rate model of induced seismicity within the Groningen Field (Part 1), Stephen Bourne and Steve Oates, Shell, July 2015.
5. An activity rate model of induced seismicity within the Groningen Field (Part 2), Stephen Bourne and Steve Oates, Shell, July 2015.
6. A Monte Carlo method for probabilistic seismic hazard assessment of induced seismicity due to conventional gas production, 2015, Bourne S.J., Oates S.J., Bommer J.J., Dost B., van Elk J., Doornhof D., Bulletin of the Seismological Society of America 105(3), 1721-1738.
7. Development of statistical geomechanical models for forecasting seismicity induced by gas production from the Groningen field, 2017, Bourne S.J., Oates S.J., Netherlands Journal of Geosciences 96(5), s175–s182.
8. Computing the Distribution of Pareto Sums using Laplace Transformation and Stehfest Inversion, Chris Harris, Shell and NAM, Aug 2015.
9. Computing the distribution of Pareto sums using Laplace Transformation and Stehfest inversion, 2017, Harris C., Bourne S.J., Pure and Applied Geophysics 174(5), 2039-2075.
10. Hazard and Risk Assessment for Induced Seismicity in Groningen, Jan van Elk and Dirk Doornhof, NAM, Nov 2015.
11. Winningsplan Groningen 2016, NAM, April 2016.
12. Evaluation of a Machine Learning methodology to forecast induced seismicity event rates within the Groningen Field, J. Limbeck, F. Lanz, E. Barbaro, C. Harris, K. Bisdom, T. Park, W. Oosterbosch, H. Jamali-Rad and K. Nevenzeel, IBM/Shell, Aug 2018.
13. Evaluation of a Machine Learning methodology for spatio-temporal induced seismicity forecasts within the Groningen field - Machine Learning, F. Lanz, K. Bisdom, E. Barbaro, J. Limbeck, T. Park, C. Harris and K. Nevenzeel, IBM/Shell, Jan 2019.
14. Bourne S.J., Oates S.J., 2017. Extreme threshold failures within a heterogeneous elastic thin-sheet account for the spatial-temporal development of induced seismicity within the Groningen gas field, Journal of Geophysical Research: Solid Earth 122(12), 10299-10320.
15. The exponential rise of induced seismicity in the Groningen gas field and its implications for controlling seismic risk, 2018, Bourne S.J., Oates S.J., van Elk J., Geophysical Journal International 213(3), 1693-1700.
16. Reader for the Spatial and Temporal development of induced seismicity in the Groningen field, NAM/Shell, Stephen Bourne and Steve Oates, November 2017

17. Gaussian Process Optimisation of the Elastic Thin-Sheet Seismological Model for Depletion Induced Seismicity in the Groningen Gas Field, G. Joosten, J. Limbeck, G. Kaleta, S. Bourne, K. Nevenzeel, Shell Research and IBM Services, Feb 2019.
18. Seismic Risk Assessment for Production Scenario “Basispad Kabinet” for the Groningen field (Addendum to: Induced Seismicity in Groningen Assessment of Hazard, Building Damage and Risk (November 2017), Jan van Elk, Assaf Mar-Or, Leendert Geurtsen, Per Valvatne, Eddy Kuperus and Dirk Doornhof, NAM, July 2018.
19. Hazard and Risk Assessment - GTS raming 2019, Jan van Elk, Assaf Mar-Or, Leendert Geurtsen, Jeroen Uilenreef and Dirk Doornhof, NAM, Mar 2019.
20. Impact of Production Fluctuations on Groningen Seismicity - Geomechanical Modelling using Rate and State friction, Nora DeDontney and Suvrat Lele, ExxonMobil Upstream Research Company, Oct 2018.
21. Seasonality analysis for induced seismicity event rate time series within the Groningen Field - Machine Learning, Park T., H. Jamali-Rad, W. Oosterbosch, J. Limbeck, F. Lanz, C. Harris, E., Barbaro, K. Bisdom & K. Nevenzeel, Shell and IBM, Oct 2018.
22. Statistical methodology for investigating seasonal variation in rates of earthquake occurrence in the Groningen field, S. Bierman, R. Paleja and M. Jones, Shell, Oct 2018.
23. A Simulation Study into the Detectability Threshold for Seasonal Variations in Earthquake Occurrence Rates within the Groningen Field - Machine Learning, T. Park and K. Nevenzeel, IBM/Shell, Feb 2019.
24. Maximum Likelihood Estimates of b-Value for Induced Seismicity in the Groningen Gas Field, November 2015, Chris Harris and Stephen Bourne.
25. New Maximum-Likelihood Method for Determining the Correlation Dimension of Clusters of Seismic Events, Chris Harris and Stephen Bourne September 2018.
26. Characterization of Induced Seismicity using Fiber Bundle Models, Chris Harris and Stephen Bourne,

NAM

Title	**Evolution of induced earthquake magnitude distributions with increasing stress in the Groningen gas field**	**Date**	November 2019
		Initiator	NAM
Autor(s)	Stephen Bourne and Steve Oates	**Editors**	Jan van Elk Dirk Doornhof
Organisation	Shell P&T	**Organisation**	NAM
Place in the Study and Data Acquisition Plan	Study Theme: Seismological Model Comment: As part of the NAM-led studies program into induced seismicity in Groningen, a number of seismological models have been prepared for the Groningen gas field. In 2013, a strain-partitioning seismological model (SM V1) was presented in the technical addendum to the winningsplan 2013. This model is further described in a scientific peer-reviewed paper published in the Journal of Geophysical Research. This model was used in the hazard assessment of Winningsplan 2013. In 2015, as an alternative seismological model, the activity rate model (SM V2), was introduced. Like the strain-partitioning seismological model, the new activity rate model was based on a statistical analysis of the historical earthquake record of Groningen, in combination with the measured subsidence. Both the strain-partitioning seismological model and the alternative activity rate seismological model have been reviewed by Ian Main, Professor Seismology & Rock Physics at the University of Edinburgh. The activity rate model was described in two scientific papers. To be able to implement the new model in the hazard and risk assessment, the distribution of pareto sums needs to be computed. A new method using Laplace Transformation and the Stehfest inversion was developed to do this efficiently. The activity rate model has been used in the hazard and risk assessment of November 2015 and winningsplan 2016. Alternative seismological models were developed using two approaches; (1) geomechanical / statistical method and (2) machine learning. The effort to develop a seismological model using machine learning has been documented. Although innovative methods were developed to forecasts seismicity in the Groningen field, the machine learning approach did not lead to an improved seismological model. Based on geomechanical principles, a set of different seismological models based on extreme threshold failures off a thin-sheet were developed. These were trained on the earthquake catalogue until 2012. Based on their ability to forecast the earthquake record for the period 2012 to 2017 the best performing model was chosen for implementation into the hazard and risk assessment (SM V5). This was documented in two scientific papers, which are also available in a reader. Using Gaussian Process Optimisation an attempt was made to further improve the elastic thin-sheet seismological model. This		

	hazard and risk model (SM V5) was used in the hazard and risk assessment for the production schedule Basispad Kabinet in 2018 production schedule GTS-raming in 2019. A number of studies were performed to test the hypothesis that apart from the gas volume produced, also the gas extraction rate impacts the seismic event rate. Both statistical/geomechanical and machine learning approached showed the available data did not support this hypothesis. Due to the limited size of the seismic record for Groningen, the possibility of a limited effect cannot be excluded. The development of the seismological model had to this point primarily focused on the forecasting of the spatial and temporal development of earthquake events. For the forecasting of the frequency-magnitude relationship a power law (Gutenberg-Richter) with a b-factor was used. As the seismic catalogue for the Groningen field is relatively small compared to other regions, an improved methodology needed to be developed to estimate the unbiased b-factor for a small earthquake catalogue. This report also showed that for different areas of the Groningen field potentially different b-factors could be estimated. Another study investigated the correlation dimension of clusters of seismic events. These studies led to a renewed interest in the frequency-magnitude relationship. A foundational study for this effort investigated fibre-bundle models. Insights from this study and other statistical mechanical theories of brittle failure within heterogeneous media, statistical seismology, and acoustic emissions experiments indicate the pure power-law may contain a stress dependent exponential taper. Incorporating such an exponential taper in the seismological model for Groningen improved its forecasting performance. The current report reviews the existing theoretical and observational evidence for a stress-dependent exponential taper to motivate a range of alternative frequency-magnitude models suitable for induced seismicity hazard and risk analysis. For a set of different models the forecast performance was assessed using Bayesian inference, hindcast evaluations and forward-model simulations. This shows that the stress-dependent taper model with constant b-factor likely offers higher performance forecasts, than the stress-dependent b-models.
Directliy linked research	(1) Reservoir engineering studies in the pressure depletion for different production scenarios. (2) Seismic monitoring activities; both the extension of the geophone network and the installation on geophones in deep wells. (3) Geomechanical studies (4) Subsidence and compaction studies.
Used data	Catalogue of seismic events, KNMI.
Associated organisation	Shell P&T
Assurance	This report has been reviewed by Ian Main, Professor Seismology & Rock Physics at the University of Edinburgh, Torsten Dahm and Gert Zöller at the GFZ German Centre of Geosciences at Potsdam University, and Jean-Philippe Avouac at Caltech.

Evolution of induced earthquake magnitude distributions with increasing stress in the Groningen gas field

S.J. Bourne, S.J. Oates

20 November, 2019

RESTRICTED DRAFT

Abstract

Geological faults can fail and produce earthquakes under the increased stresses associated with hydrocarbon recovery, geothermal extraction, CO_2 storage or subsurface energy storage. The risks to containment of subsurface fluids and to the integrity of the built environment depend critically on the frequency and size of any induced seismicity. Within seismic hazard and risk analysis, the exceedance probability of seismic moments, $\mathcal{M}$, is treated as a pure power-law distribution, $\sim \mathcal{M}^{\beta}$, where the power-law exponent, β, may vary in time or space or with stress. Insights from statistical mechanics theories of brittle failure within heterogeneous media, statistical seismology, and acoustic emissions experiments all indicate this pure power-law may contain an exponential taper, $\sim \mathcal{M}^{\beta} e^{-\zeta \mathcal{M}}$, where the taper strength, ζ, decreases with increasing stress. The role of this taper is to significantly reduce the probability of earthquakes larger than ζ^{-1} relative to the pure power-law. This effect may appear as an apparent increase in β values with stress if taper effects are ignored.

We review the existing theoretical and observational evidence for a stress-dependent exponential taper to motivate a range of alternative frequency-magnitude models suitable for induced seismicity hazard and risk analysis. These include stress-invariant models with and without a taper, stress-dependent β models without a taper, stress-dependent ζ models, and a hybrid stress-dependent β-ζ model. For each of these models, we evaluated their forecast performance for induced seismicity within the Groningen gas field in the Netherlands. Through a combination of Bayesian inference, hindcast evaluations, and forward-model simulations we assessed the forecast performance capabilities of each model. Our results show that the stress-dependent ζ-model with constant β likely offer higher performance forecasts than the stress-dependent β-models with $\zeta = 0$ 75–85% of the time. This model also lowers the magnitude with a 10% and 1% chance of exceedance over the next 5 years of gas production from 4.3 to 3.7 and from 5.5 to 4.3 respectively.

1 Introduction

Induced seismicity may arise due to mining, geothermal energy production, artificial lakes, and fluid injection or production, including hydrocarbon production, water disposal or CO_2 storage. Most of these activities occur without inducing any noticeable earthquakes. Nonetheless, due to the quantity and scale of these activities, there is a growing number of notable occurrences of induced earthquakes. Several recent reviews comprehensively summarise the world-wide evidence for seismicity induced by human activities (Majer et al., 2007; Suckale, 2009; Evans et al., 2012; Davies et al., 2013; Ellsworth, 2013; Klose, 2013; NAS, 2013; IEAGHG, 2013; Foulger et al., 2018).

In such cases of induced seismicity, any exposure to the associated hazards of seismic ground motions or the risks of building damage must be assessed using probabilistic seismic hazard and risk analysis (*e.g.* Elk et al., 2019), and then if necessary mitigated. Induced seismicity is a transient non-stationary process in response to time-varying and significant increases in stress that are sufficient to destabilize previously inactive faults. Forecasting such failures within a geological material critically depends on its heterogeneity (Vasseur et al., 2015).

Heterogeneity falls into two classes. Resolvable heterogeneity that may be map and accounted for with deterministic models such as large-scale fault geometries. Unresolvable heterogeneities also influence failures and must be accounted for with statistical models. This approach led to the development of Extreme Threshold Failure models of induced seismicity occurrence where the resolvable heterogeneities are included in a deterministic poro-elastic thin-sheet stress model and the unresolvable heterogeneities are represented by the tail of a pre-stress probability distribution given by the universal form of a Generalized Pareto distribution (Bourne and Oates, 2017). This simple model explains the observed, non-stationary, space-time statistics of induced seismicity within the Groningen gas field and provides a physical explanation for the exponential-like increase in seismicity rates relative to stress rates (Bourne et al., 2018).

Current methods of forecasting induced earthquake magnitudes are empirical and lack a clear physical basis. Natural and induced seismicity hazard analysis for the United States assumes a stationary process with a stress-invariant pure power-law distribution of seismic moments (Petersen et al., 2018). Shapiro et al. (2010a) proposed a non-stationary model for fluid injection induced seismicity that includes a pre-stress disorder with a uniform distribution to model event occurrence but assumes a stress-invariant pure power-law distribution of seismic moments (Shapiro et al., 2010b; Langenbruch and Zoback, 2016; Shapiro, 2018). Hazard analyses for Groningen

induced seismicity also assume a pure power-law and takes an empirical approach to include apparent compaction- (Bourne et al., 2014) or stress-dependence (Bourne et al., 2018) of the power-law exponent. If this pure power-law assumption is not valid then all these models may be incomplete and biased in their earthquake magnitude forecasts especially under the significantly increasing stress loads often associated with induced seismicity.

This study seeks to extend the method of treating unresolvable heterogeneities as stochastic disorder to improve the seismological models used for forecasting induced earthquakes magnitudes for the purpose seismic hazard and risk analyse. We will build on previous work to incorporate the failure mechanics of disordered media into a statistical mechanics theory of natural earthquakes (*e.g.* Bak and Tang, 1989; Alava et al., 2006; de Arcangelis et al., 2016), and their seismic hazard analysis Main (1996). These statistical mechanic theories will be used to motivate the choice of models to evaluate, but not to rank or select them. Under many different theories the probability distribution of failure event sizes follows a power-law subject to an exponential taper where the power-law exponent is stress-invariant whilst the characteristic taper scale increases as a critical-point power-law with stress. However, under some other circumstances the power-law exponent may exhibit variation with stress. We reflect these possibilities by specifying 5 different classes of frequency-moment models for induced earthquakes:

1. Stress-invariant power-law with no taper
2. Stress-invariant power-law with a stress-invariant taper
3. Stress-dependent power-law with no taper
4. Stress-invariant power-law with a stress-dependent taper
5. Stress-dependent power-law with a stress-dependent taper

Using Bayesian inference we sample the full posterior distribution of possible models given the observed history of induced seismicity and induced stress within the Groningen gas field for a range of different parametrization choices within each of the 5 model classes. Our evaluation of the Groningen forecast performance for induced earthquake magnitudes reveals the best-performance requires a stress-dependent taper as anticipated by most statistical mechanics theories of brittle fracture.

After briefly stating the standard power-law formulation of seismic moments in statistical seismology (section 2), we will summarize the seismological literature that proposes (section 3) or opposes (section 4) evidence for stress-dependent variations of power-law exponent with stress. We will

then describe our model of intra-reservoir induced stress due to pore-pressure changes (section 5) followed by simple statistical analyses of the variations in observed earthquake magnitudes induced by Groningen gas production (section 6). Then after reviewing existing statistical mechanics theories of earthquakes (section 7) we specify our models for the stress-dependence of induced earthquake magnitude distributions (section 8), infer their parameter values (section 9), assess their behavioural characteristics (section 10), and evaluate their performance (section 11), before assessing their implications for seismic hazard and risk (sections 12 and 13).

2 Power-law distribution of seismic moments

The exceedance probability distribution of earthquake magnitudes typically takes the form:

$$P(>M|>M_{\min}) = 10^{-b(M-M_{\min})}, \tag{1}$$

where M is the earthquake moment magnitude conditional on $M \geq M_{\min}$ and b defines the negative slope of the exponential distribution (Gutenberg and Richter, 1954). Alternatively, this may be expressed according to the seismic moment, s, which scales with moment magnitudes as,

$$\log_{10} \mathcal{M} = (c + dM), \tag{2}$$

with, $c = 9.1$, and $d = 1.5$. Combining (1) and (2) leads to the equivalent power-law distribution,

$$P(>\mathcal{M}|>\mathcal{M}_{\min}) = \left(\frac{\mathcal{M}}{\mathcal{M}_{\min}}\right)^{-\beta}, \tag{3}$$

and $b = \beta d$.

Seismic hazard and risk analysis is highly influenced by the estimation of β-values. Lower β-values mean larger expected magnitudes and a larger expected maximum magnitude for a given population of earthquakes. In the next two sections we outline the existing evidence for two alternate hypotheses about the influence of stress on β-values.

3 β-values vary with stress

A number of observations and modelling results might suggest that earthquakes b-value depends on the stress level. Measured earthquake b-values decrease systematically from 1.2 to 0.8 with increasing depth in the brittle

crust from 5 to 15 km (Mori and Abercrombie, 1997; Spada et al., 2013). Similar measurements indicate earthquake b-values vary systematically with focal mechanism rake angle as a proxy for stress (Schorlemmer et al., 2005; Gulia and Wiemer, 2010). Lower stress, normal faulting b-values are typically 1.0–1.2. Whereas higher stress, thrust faulting b-values are typically 0.7–0.9. Intermediate stress, strike-slip b-values are in the range 0.9–1.0 (Wiemer and Wyss, 1997, 2002; Huang et al., 2018).

b-values also appear to be a proxy for shear stress and pore pressure (Scholz, 1968; Schorlemmer et al., 2005; Bachmann et al., 2012). Bachmann et al. (2012) observed b-values decrease with a decrease in pore-pressure for induced earthquakes of an Enhanced Geothermal System. Whilst systematically smaller b-values were measured for earthquakes induced by larger reservoir compaction (Bourne et al., 2014) or higher Coulomb stress (Bourne et al., 2018) associated with natural gas production. Variations in measured b-values are also used to indicate material heterogeneity (Mogi, 1962; Main et al., 1992; Mori and Abercrombie, 1997) or for fault asperity mapping (Tormann et al., 2014). The scale of fault heterogeneities appears to follow a power-law where its fractal dimension governs the b-value of seismic slip events within this fault population (Main et al., 1989, 1990, 1992). Initial heterogeneities in the form of a fractal distribution of fault sizes or fault asperities are one way to explain the Gutenberg-Richter law. Another explanation is that is arises from some distribution of strength.

Variations in observed b-values may also be precursors of future rupture areas and sizes (Schorlemmer et al., 2005). In this case, b-values decrease monotonically throughout the precursory phase, and then recovers abruptly after peak stress (marked by a sudden stress drop event). Scholz (1968) introduced a statistical model of brittle failure within an inhomogeneous elastic medium to explain the apparent decrease in b-values with increasing stress.

4 β-values do not vary with stress

In this hypothesis all observed b-values are consistent with a constant value in both space and time and any observed apparent variations are artefacts due to under-sampling (detection threshold and finite sample size effects), magnitude errors, non-homogeneous detection capabilities, and improper statistical tests (Shi and Bolt, 1982; Frohlich and Davis, 1993; Kagan, 1999, 2002b, 2010; Amorèse et al., 2010; Amitrano, 2012; Kamer and Hiemer, 2015). For example, observed variations in b-values with stress rely on the maximum likelihood estimator Aki (1965), with corrections for the magnitude binning

(Utsu, 1965; Bender, 1983; Tinti and Mulargia, 1987). This method implicitly assumes that the underlying distribution is a pure power-law above some threshold of completeness according to equation (3). If this is not the case, then this estimator will be biased and confounded with any non-power-law stress-dependent variations in the frequency magnitude distribution, as we will show later.

Recent developments in statistical fracture and earthquake mechanics theories indicate that a wide range of physical mechanisms and conditions all lead to the same frequency-magnitude distribution that is a stress-invariant power-law with a stress-dependent exponential taper. We will now review these theories as a physical basis for β-values that do not vary with stress and to introduce an alternative stress-dependence for the frequency distribution of earthquakes induced by Groningen gas production.

5 Poro-elastic thin-sheet stress model

The development of external loads on pre-existing weak fault structures within the Groningen gas field depends on the evolution of reversible reservoir deformations induced by pore pressure changes. Within the limit of small strains, these reservoir deformations are well-described by linear poro-elasticity. For thin reservoir geometries where the lateral extent of the reservoir greatly exceeds its thickness, the reservoir deforms predominately as a thin-sheet. Within the poro-elastic, thin-sheet approximation (Bourne and Oates, 2017), depletion-induced reservoir displacement vector field, $\mathbf{u}(\mathbf{x})$, is constrained by symmetry to vertical displacements, $u(\mathbf{x})\hat{\mathbf{z}}$, where $\hat{\mathbf{z}}$ is the unit vertical vector. From this approximation it follows that the vertically-averaged incremental Coulomb stress states are:

$$\Delta C(\mathbf{x}, t) = -\gamma H_p(\mathbf{x}) \Gamma(\mathbf{x}) \Delta P(\mathbf{x}, t) \tag{4}$$

where $\Delta P(\mathbf{x}, t)$ is the change in reservoir pore fluid pressure, $\Gamma(\mathbf{x})$ is the magnitude of lateral gradients in the elevation of the top surface bounding the thin-sheet, $\gamma = \nu/(1-2\nu)$ and ν is Poissons ratio taken to be 0.25. $H_p(\mathbf{x})$ is a poro-elastic material property defined as:

$$H_p(\mathbf{x}) = \frac{H_s}{H_s + H_r(\mathbf{x})} \tag{5}$$

where H_s is a constant related to the shear modulus of the skeleton material comprising the poro-elastic medium and estimated as a model parameter. $H_r(\mathbf{x})$ is the time-invariant ratio of the observed reservoir depletion to

the observed reservoir compaction strain, $\Delta P(\mathbf{x},t)/\epsilon_{zz}(\mathbf{x},t)$. Reservoir compaction strain is inferred from geodetic monitoring of surface displacements, and reservoir depletion is measured by in-well pressure gauges. For depletion, *i.e.* $\Delta P(\mathbf{x},t) < 0$, incremental Coulomb stresses increase towards frictional fault failure in locations where $\gamma H_p(\mathbf{x}) > 0$, otherwise depletion acts to increase frictional fault stability. In the presence of pre-existing faults that partially offset the thin-sheet, $\Gamma(\mathbf{x})$, is locally increased and acts to increase the sensitivity of Coulomb stress to pore-pressure changes. The deterministic reservoir map $-\gamma H_p(\mathbf{x})\Gamma(\mathbf{x})$ describes the time-invariant, local sensitivity of Coulomb stress to reservoir pore pressure changes, $\Delta C/\Delta P$, or stress susceptibility. This map was estimated by multiplying $\Gamma(\mathbf{x})$ and $-\gamma H_p(\mathbf{x})$ maps independently inferred from field observed quantities. $\Gamma(\mathbf{x})$ is computed from the top reservoir surface mapped by reflection seismic imaging.

Two modifications help to improve the performance of this thin-sheet model. First, we filter the contribution of individual faults to the topographic gradient field, $\Gamma(\mathbf{x})$, according to their juxtaposition geometry with the reservoir, by including fault segments according to the criterion:

$$r \leq r_{\max}, \tag{6}$$

where r is the local ratio of fault throw to reservoir thickness, and $r_{\max}$ is a model parameter. This represents the consequences of juxtaposition, where faults offset the reservoir against the overlying and ductile Zechstein salt formation. Increased juxtaposition of the reservoir interval against the Zechstein formation may limit induced seismicity by favouring ductile fault creep instead of a stick-slip behaviour. Second, we use a smoothed incremental Coulomb stress model, $\Delta\tilde{C}(\mathbf{x},t)$, evaluated as:

$$\Delta\tilde{C}(\mathbf{x},t) = \int_S \Delta C(\mathbf{x},t) G(\mathbf{x},\mathbf{x}') dS' \tag{7}$$

a surface integral over the entire model domain, S, where $G(\mathbf{x},\mathbf{x}')$ is the isotropic Gaussian kernel:

$$G(\mathbf{x},\mathbf{x}') = \frac{1}{\sqrt{2\pi}\sigma} e^{-\frac{(\mathbf{x}-\mathbf{x}')^2}{2\sigma^2}} \tag{8}$$

defined by the characteristic smoothing length-scale, σ.

This poro-elastic, thin-sheet stress model has three degrees of freedom $\{\beta_2, \beta_3, \beta_4\}$; the smoothing length-scale, $\beta_2 = \sigma$, the maximum juxtaposition ratio, $\beta_3 = r_{\max}$, and the poro-elasticity constant $\beta_4 = H_s$. These three parameters are optimized jointly with a given seismological models that defines the conditional probabilities of earthquake occurrence and size given

the smoothed incremental Coulomb stress field, $\Delta\tilde{C}(\mathbf{x}, t)$, and the observed catalogue of induced earthquakes, $\mathbf{D}$.

This model is applicable to any reservoir subject to pore-pressure changes that is thin relative to it's lateral extent and smoothing length-scale such that uni-axial displacements dominate. In the particular case of the Groningen reservoir the posterior distribution of thin-sheet models inferred given the observed history of pore-pressure depletion, reservoir compaction, and induced seismicity (Bourne and Oates, 2017). For $M \geq 1.5$ event occurrences observed from 1/1/1995 to 1/6/2019, the maximum posterior probability thin-sheet parameter values are $\beta_2 = 3$ km, $\beta_3 = 0.41$, $\beta_4 = 10^{5.3}$ MPa (Appendix C). For $M \geq 1.5$ event magnitudes observed from 1/1/1995 to 1/6/2019, the maximum posterior probability thin-sheet parameter values are obtained using the event locations and origin times from are $\beta_2 = 3.5$ km, $\beta_3 = 1.1$, $\beta_4 = 10^7$ MPa (Appendix C). The apparent difference between the optimal smoothing length-scales between these two models is not significant as both posterior distributions include both values within their 95% credible intervals. The larger apparent different in the juxtaposition parameter, β_3, nonetheless yields very similar coulomb stress models and reflects the previously observed bi-modal distribution with modes at both $\beta_3 = 0.4$ and $\beta_3 = 1.1$ (Bourne and Oates, 2017, Figure 12). The apparent difference in skeleton modulus β_4 may also reflect inference uncertainty. Inference of a single thin-sheet model given may allow better forecast performance by utilizing both the observed event occurrences and magnitudes to constrain a single stress model but this was outside the scope of our current study.

6 Observed seismicity

The Groningen field is located within the north-east of the Netherlands. The gas-bearing reservoir interval comprises the Upper Rotliegend Group (Permian) and the Limburg Group (Carboniferous) sediments, separated by the Saalian unconformity (Stauble and Milius, 1970). The depth of the Rotliegend reservoir is 2600-3200 m. The field extent is controlled primarily by fault closures with occasional local dip closures. The top seal is the Zechstein salt. Production of Groningen gas started in 1963 and pressure depletion rates increased rapidly until 1973 before reducing significantly to conserve Groningen gas reserves. From 2000 to 2014, depletion rates rose moderately in response to increased market demand and decreased capacity of other smaller gas fields. Starting in 2014, depletion rates were significantly reduced in response to induced seismicity.

The Royal Netherlands Meteorological Institute (KNMI) has monitored

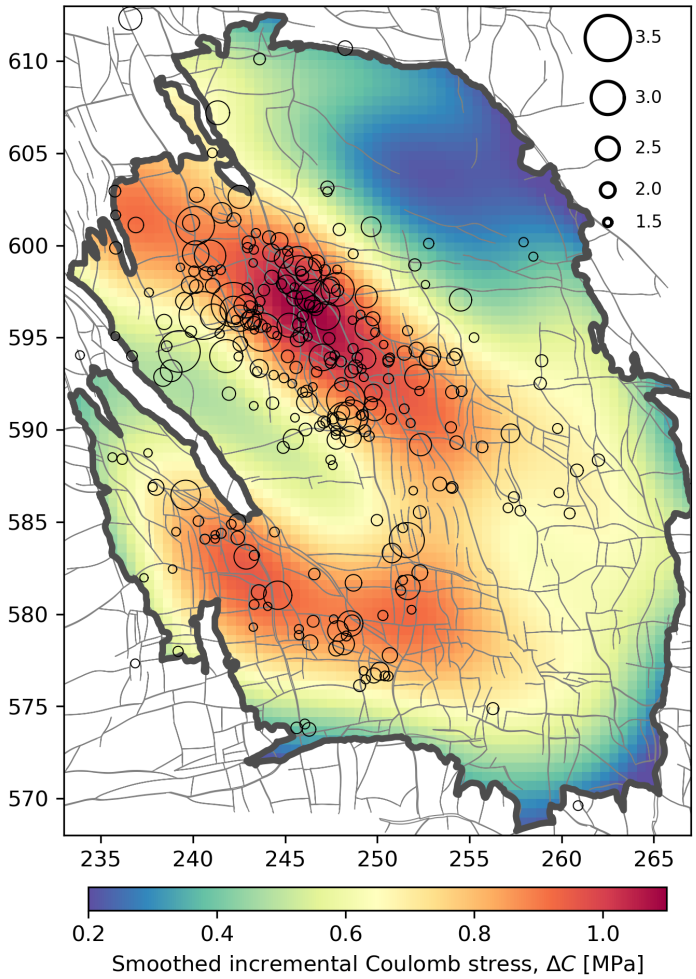

Figure 1: Observed distribution of epicentres and magnitudes of earthquakes induced by Groningen gas production since the monitoring of $M \geq 1.5$ events started in 1995. Colours denote the poro-elastic thin-sheet model of smoothed incremental maximum Coulomb within the reservoir induced by pore-pressure depletion from the start of production in 1965 until 2019. Circle denotes earthquakes and their area scales continuously with earthquake magnitude as indicate by the legend. Thin grey lines denote fault traces at the top of the reservoir. A dark grey polygon denotes the original gas-water contact respectively. Map coordinate units are kilometres.

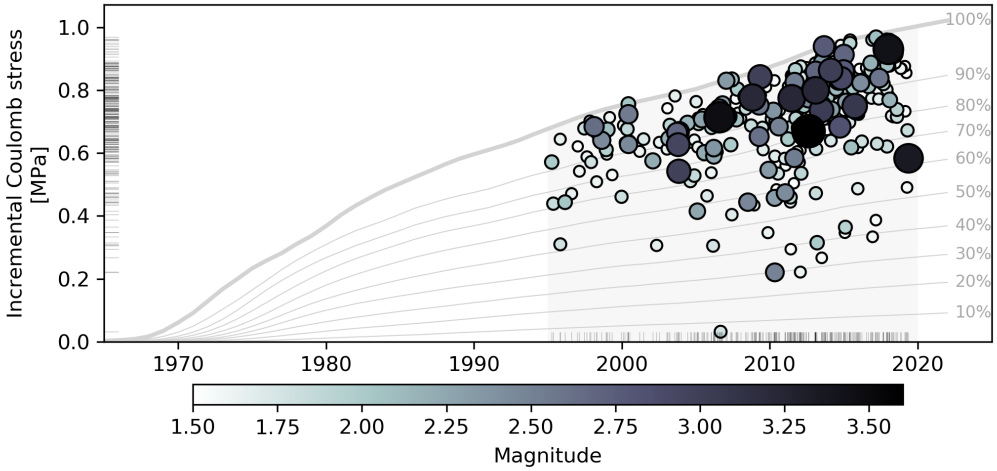

Figure 2: Time series of the incremental Coulomb stress and magnitude associated with the Groningen $M \geq 1.5$ events observed from 1995 to 2019 (grey panel). The area and colour of the circles denotes the magnitude of each event. Grey lines indicate the evolution of stress exposure within the reservoir according to the poro-elastic thin-sheet model and denote the reservoir volume fraction exposed to at most that stress state. Most events occur within the largest 20% of the exposed stress states (80%–100%).

seismicity in the Netherlands since at least 1986 (Dost et al., 2012). For the Groningen Field earthquake catalogue, the magnitude of completeness for located events is taken to be $M_L = 1.5$, starting in April 1995, with an event detection threshold of $M_L = 1.0$ (see **?**). Here we restrict our analyses to the 279 events with $M_L \geq 1.5$ recorded within the Groningen Field between 1^{st} January 1995 and 1^{st} June 2019. Epicentres of events in the catalogue are determined to within about 500-1000 m but, because of the sparseness of the monitoring array, depths were routinely estimated. For these events a depth of 3000 m–approximate reservoir depth–has been assumed. This is consistent with a limited number of reliable depth estimates from a reservoir-level borehole geophone array. Event magnitudes are reported as local magnitudes with a typical error of 0.1.

The spatial distribution of epicentres is localized within regions of the reservoir associated with larger incremental Coulomb stresses as represented by the poro-elastic thin-sheet model (Figure 1). Event origin times also appear to favour larger incremental Coulomb stress states (Figure 2) as most events occur at later times when incremental stresses are larger albeit subject to considerable variability. Likewise, larger magnitude events, *e.g.* $M \geq 2.5$,

appear mostly localised in the times and places associated with the largest 20% of the exposed reservoir stress states. The stress-dependence of event occurrence probability appears to follow an exponential-like trend consistent with an Extreme Threshold theory of initial frictional reactivations within a heterogeneous and disordered fault system (Bourne and Oates, 2017).

The observed frequency-magnitude distribution of events (Figure 3) shows clear evidence for under-reporting of $M < 1.5$ events and an apparent increase in variability with increasing magnitude due to finite sample effects.

The apparent b-values of these events also appear to decrease systematically with increasing Coulomb stress (Bourne et al., 2018) or compaction-induced strain (Bourne et al., 2014). However, the available surface displacements and seismicity observations cannot reliably distinguish between a stress or a strain driven process. Harris and Bourne (2017) demonstrated the observed frequency-magnitude distribution of 1995 to 2015 $M \geq 1.5$ events with epicentres inside a central elliptical region of the Groningen field is significantly different from those located outside this region with a statistical confidence exceeding 95% under the Kolmogorov-Smirnov test statistic. This elliptical region was centred close to the centroid of seismicity and oriented and sized to divide these events into approximately two equally-sized populations. Maximum likelihood estimates for the b-values were $b = 0.7$ and $b = 1.2$ for the inside and outside events respectively.Poro-elastic thin-sheet reservoir stress models indicate the region inside this ellipse experienced systematically higher maximum Coulomb stress states throughout this time period indicating these significantly lower b-value estimates are associated with a history of higher Coulomb stress states.

All these observations may however be an artefact of assuming a pure power-law frequency distribution of seismic moments without allowing for the possibility of other distributions such as a power-law with an exponential taper. All these previous observations also relied on catalogues of Groningen earthquake magnitudes reported to one decimal place. In the following sections we will assess the observable relationship between the distribution of earthquake magnitudes, now reported to 2 decimal places, and the reservoir stress history due to pore pressure depletion according to poro-elastic thin-sheet reservoir deformation model calibrated to the observed history of pore pressure depletion, surface displacements, and the space-time distribution of earthquake occurrences (Bourne and Oates, 2017; Bourne et al., 2018).

6.1 Frequency-magnitude stress dependence

To investigate stress-dependence of the frequency-magnitude distribution without making any assumptions about the particular form of this distri-

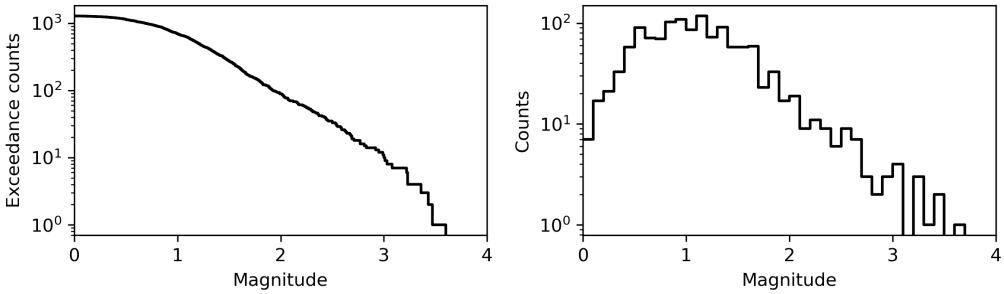

Figure 3: The frequency magnitude distribution of earthquakes from 1/1/1995 to 1/6/2019 associated with Groningen gas production. (left) Exceedance counts denotes the number of events with at least the given magnitude. (right) Counts denotes the number of events within magnitude bins of size 0.1. The magnitude of completeness for this catalogue is in the range 1.3–1.5.

bution we will use the Kolmogorov-Smirnov test statistic. First, we compute the incremental Coulomb stress, ΔC_i, at the origin time, t_i and epicentral location, $\mathbf{X}_i$ of each observed $M \geq 1.5$ event from 1995 to 2019, according to the poro-elastic thin-sheet reservoir model. Based on these values, we divide the events into two disjoint samples: a low stress sample, $\Delta C_i < \Delta C$, and a high stress sample, $\Delta C_i \geq \Delta C$. By increasing the stress threshold, ΔC, we compute the Kolmogorov-Smirnov test statistic p-value for all possible divisions of the events (Figure 4a), and repeat this procedure for alternative minimum magnitudes of completeness in the range $1 \leq M_{\min} \leq 2$ (Figure 4b). This p-value measures the probability that these two independent samples were drawn from the same underlying probability distribution.

The smallest p-values found are about 10^{-3} and correspond to $M_{\min} = 1.5$, a $\Delta C = 0.7$ MPa stress threshold, with about 100 and 200 events in the low- and high-stress samples respectively. This result appears robust to alternative values of $M_{\min}$ such that the 95% confidence threshold is exceeded also for $1.0 \leq M_{\min} \leq 1.7$. For $M_{\min} > 1.7$, the loss of statistical power due to the smaller number of these larger events likely predominates. Consequently we conclude there is a statistically significant stress dependence in the frequency-magnitude distribution of Groningen induced earthquakes. Figure 5 shows the empirical exceedance distribution functions and epicentral map locations for this optimal stress-based division of the observed events.

By simple visual inspection, the different distributions appear consistent with β-values decreasing with stress or ζ-values increasing with stress. Ergodicity is implicit within this stress covariate hypothesis. That is to say

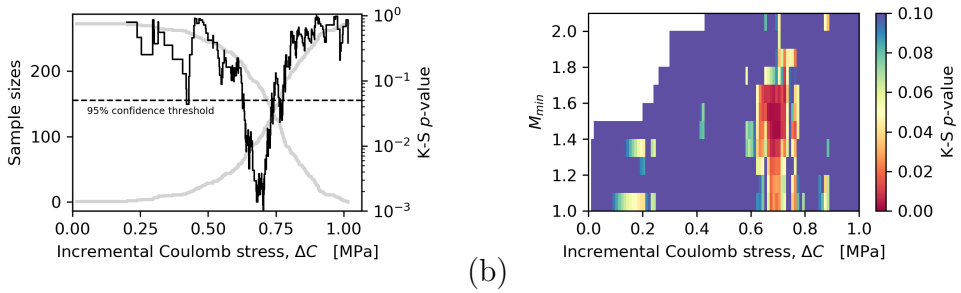

(a) (b)

Figure 4: (a) Kolmogorov-Smirnov test statistic p-values for each possible division of the observed $M \geq 1.5$ events since April 1995 into low and high incremental Coulomb stress, ΔC, groups according to the poro-elastic thin-sheet stress model ($\sigma = 3.5$ km, $r_{\max} = 1.12$, $H_s = 10^{13}$ Pa). The i^{th} event belongs to the low stress group if $\Delta C_i < \Delta C$; otherwise it belongs to the high stress group. (b) As (a), except for all $M \geq M_{\min}$ events over the range $1.0 \leq M_{\min} \leq 2.0$.

a temporal stress change is indistinguishable from a spatial stress change of the same amount. The separation of high and low-stress events in space (Figure 5) more than in time (Figure 2) might indicate the influence of some initial spatial heterogeneity (quenched disorder). However, closer inspection of the map shows spatial mixing with many low- and high-stress events occurring in similar locations. This means there are three distinct spatial domains. A low-stress domain that has never experienced incremental stress above the 0.7 MPa threshold over the period of observation. A high-stress domain that has never experienced incremental stress below the 0.7 MPa threshold over the period of observation. Finally, an intermediate stress domain that has experienced stress states that have crossed the 0.7 MPa threshold at some time during the period of observation.

Any continuous stress-dependence of the frequency-magnitude distribution implies both samples still represent a mixture of different distributions reflecting the range of stress states within each sample. In this case subdivision of the events into more than 2 disjoint samples fails to reveal any reliable evidence for this which we attribute to the reduction of statistical power which limits our resolution of this stress dependency under the Kolmogorov-Smirnov non-parametric test statistic.

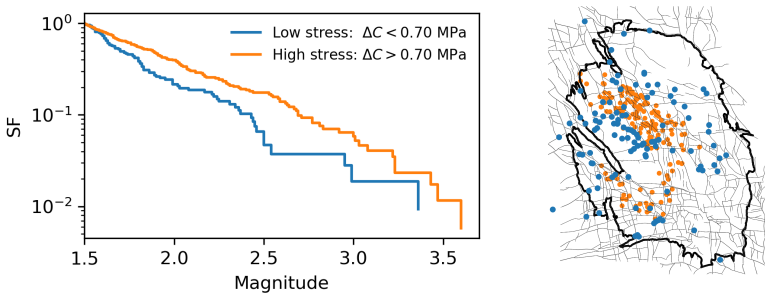

Figure 5: The observed earthquake size distribution and epicentral locations of low- and -high stress groups most likely to originate from different probability distributions.

6.2 Apparent stress dependence of β- and ζ-values

The significant stress-dependent differences found in the observed frequency-magnitude distribution may reflect a decrease in the power-law exponent, β, and the exponential taper exponent, ζ, with increased Coulomb stress. To measure any apparent variations of β- or ζ-values with Coulomb stress, we first ordered the $M \geq 1.5$ observed events from 1/4/1995 to 1/6/2019 according to the incremental maximum Coulomb stress at their time and place of occurrence within the poro-elastic thin-sheet reservoir deformation model. This yields a sequence of N incremental Coulomb stress values $\{\Delta C_1, \ldots, \Delta C_N\}$, and a paired sequence of event magnitudes $\{M_1, \ldots, M_N\}$. For the first k events in this paired sequence, we computed the posterior distribution of β-values for a constant β-value model with no exponential cut-off ($\zeta = 0$), and repeated this for every set of k consecutive events. Figure 6a shows the resulting β-value estimates and their uncertainties for $k = 20$ which tend to decrease with increasing Coulomb stress. A clear step-like decrease is evident at $\Delta C = 0.7$ MPa which is consistent with the previous Kolmogorov-Smirnoff test (Figure 4a). Such gradual evolution due to a mixing of different states has recently been demonstrated in lab data (Jiang et al., 2017) and also seen in volcanic seismicity (Roberts et al., 2016).

Repeating this procedure for a constant ζ-value model with fixed at its

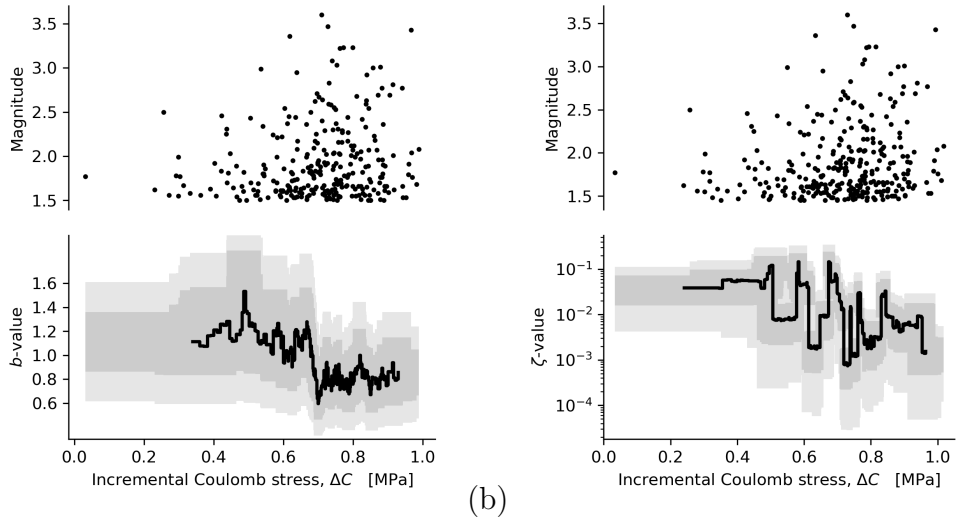

(a) (b)

Figure 6: Variation of posteriori (a) b-value and (b) ζ-value estimates with incremental Coulomb stress given $M_{\min} = 1.5$ and a constant population sample of 20 events. Light and dark grey bands denote the 67% and 95% confidence intervals, and $\beta = \frac{2}{3}b$.

presumed universal value ($\beta = 2/3$), yields a similar trend of decreasing values with increasing Coulomb stress (Figure 6b). These piece-wise constant estimates for the variation of β- or ζ-values with Coulomb stress depend in detail on the choice of sample size, k. Larger k-values allow reduce uncertainties in the estimated β- and ζ-values but lower their resolution of any stress dependency. Likewise, smaller k-values increases stress resolution at the expense of precision. Nonetheless, similar results were obtained over a wide range of k-values indicating an apparent general tendency for β- and ζ-values to decrease with increasing Coulomb stress under the poro-elastic thin-sheet model. Once more, there is evidence for mode switching or mixing under increased stress.

7 Statistical mechanics of earthquakes

We will now briefly review the statistical mechanics aspects of earthquakes that motivate our choice of possible models that are included in the evaluation (Figure 7). We will only use these theories for hypothesis identification and *not* for hypothesis testing, which we will do instead using the available observations of Groningen induced seismicity.

Heterogeneity is the key to forecasting failure events within geological materials as consistently demonstrated in the laboratory experiments (Vasseur et al., 2015, 2017). Statistical models distinguish themselves from deterministic models of fractures by incorporating the influence of unresolvable heterogeneities as stochastic disorder. Statistical theories of brittle rock strength originate with Weibull (1939) and now fall within a broad class of statistical models of fractures (*e.g.* Alava et al., 2006) and earthquakes (de Arcangelis et al., 2016).

Figure 8 illustrates this abstraction process of replacing the unknown distribution of fault heterogeneities (disorder) that influence the initiation and termination of frictional fault slip under an external stress with stochastic variables representing the probabilities of failure given the local stress states. These local stress states depend on the external stress and the redistribution of stresses due to previous failures.

Within these theories, the frequency-moment power-law may be derived in one of at least four different ways.

1. The geometric constraints associated with the number of permutations available for tiling rupture areas over a fault surface (Main and Burton, 1984).

2. Within the renormalisation group model for a wide-variety near-critical

physical systems (*e.g.* chapter 15 Turcotte, 1997).

3. Within percolation theory near the percolation threshold (*e.g.* Stauffer and Aharony, 1994).

4. Within self-organized criticality theory (Bak and Tang, 1989; Main, 1996).

Likewise, the frequency-moment distribution as a power-law with an exponential taper also has a physical basis in at least four different statistical mechanics theories.

1. Within fiber bundle models of brittle failure with equal-load sharing (*e.g.* Pradhan, 2010). See Appendix A for a more detailed review.

2. Within percolation theory below the percolation threshold (*e.g.* Stauffer and Aharony, 1994). See Appendix B for a more detailed review.

3. Within Ising models of brittle failure with local-load sharing.

4. Within interface theories of crack depinning in the presence of heterogeneity (*e.g.* Daguier et al., 1997).

5. Within information theory, using the concept of maximum entropy to find the least-informative probability distribution subject to observational constraints on the mean magnitude and mean total seismic moment rate (Main and Burton, 1984).

For earthquakes, we are concerned with the limit that these redistributed stress perturbations are small relative to the external stress known as damage mechanics. Damage mechanics models exist in two distinct classes (Figure 7). First, network models that address the evolution of failure across a distributed collection of interacting elements. Second, interface models that focus on the advance of a fracture tip line within a heterogeneous medium.

Network damage models take three key forms with respect to failures. Random fuse networks (Roux et al., 1988; de Arcangelis et al., 2007; Hansen, 2011), provide a model of brittle failure within a scalar central force network (Gilabert et al., 2007). Each fuse within the network has a randomly assigned and invariant failure threshold (quenched disorder). Increasing external voltage leads to failure of individual fuses and re-distribution of current across the network that potentially triggers additional failures at constant applied voltage. Mean field theory (Toussaint and Hansen, 2006) shows this is a percolation process in the limit of infinite disorder (Roux et al., 1988) where re-distributed loads are equally shared. Random spring networks (Nukala

et al., 2005) provide a model of brittle failure within a tensor central force network. Here, springs failure under a quenched random strain threshold and forces are re-distributed across the remaining spring network. Under simple shear loads, failure within this network is equivalent to random fuse networks.

Random block-spring networks (Burridge and Knopoff, 1967) represent

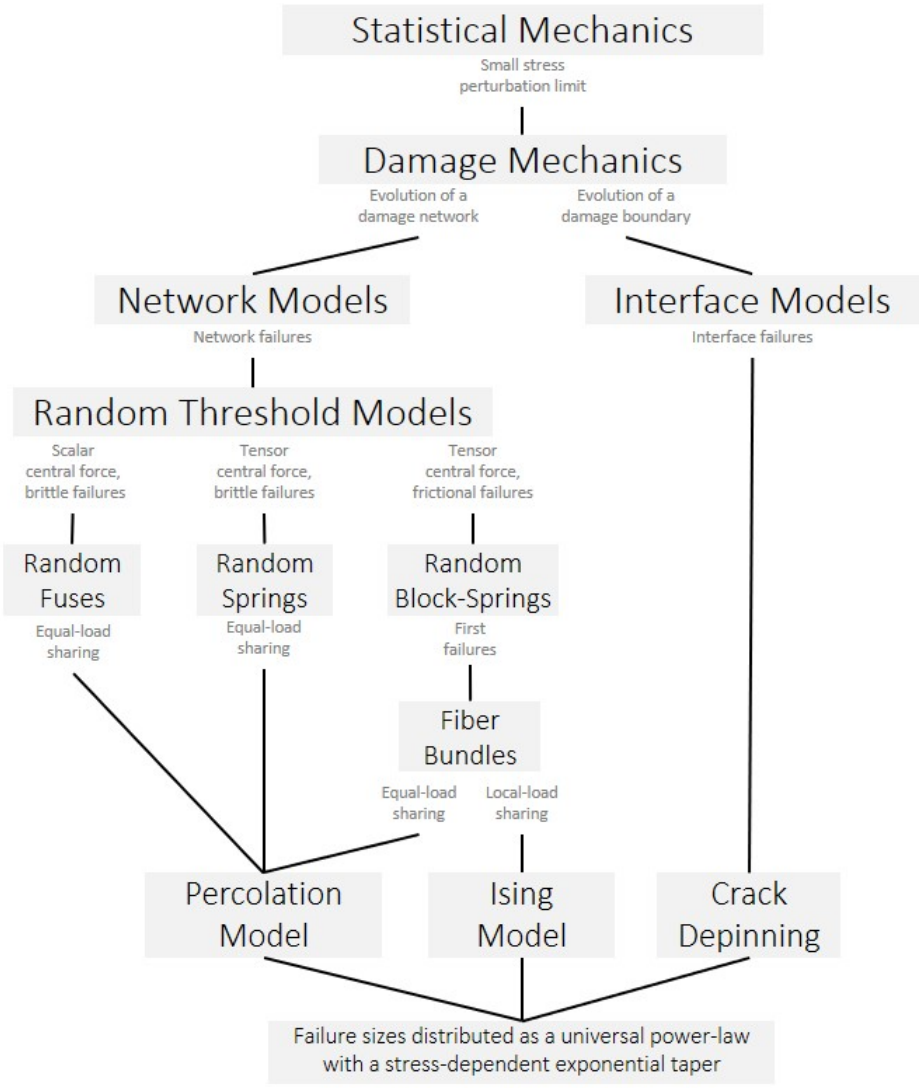

Figure 7: The network of statistical damage mechanics theories that seek to describe mechanical failure as a stochastic process. This different models all lead to failure sizes distributed according to a stress-invariant power-law with a stress-dependent exponential-like taper.

frictional failures within a tensor central force network. A network of slider-blocks in frictional contact with a rigid basal surface and are connected to each other and to a driver plate by a network of springs. Displacement of the driver plate loads the blocks which slide when the basal shear exceeds the frictional threshold. Basal shear stresses are initiated as a random quenched disorder. Within mean field theory (Sornette and Physique, 1992), the first cycle of failures is equivalent to the fiber bundle model (Hansen and Hemmer, 1994; Hemmer and Hansen, 1992; Kloster et al., 1997; Pradhan, 2010). Toussaint and Pride (2005) demonstrates an isomorphism of weak lattice damage models with fiber bundle model which in turn is isomorphic with percolation theory for equal load sharing or the Ising model for local load sharing. Using renormalisation group theory, Shekhawat et al. (2013) unified the theories of fracturing within a disorder brittle material for infinite disorder (percola-

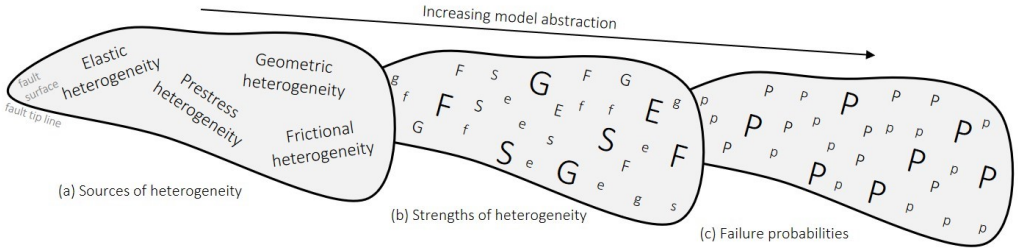

Figure 8: Schematic to illustrate (a) the different sources and (b) the different strengths of unresolved fault heterogeneity and (c) their stochastic representation as local failure probabilities that lead to the emergence of an exponentially tapered power-law distribution of failure sizes.

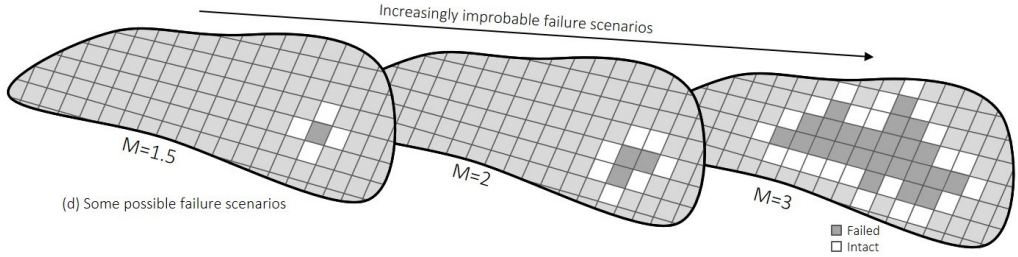

Figure 9: The probability-area distribution of fault failure events arising on a single fault with a network of uniform failure probabilities is an exponentially-tapered power-law. The lower probabilities of larger failure areas are governed by competition between the lower probability of a larger number of connected dark grey failed cells bordered by white intact cells and the larger number of alternative geometric configurations with the same failure area.

tion) and zero disorder (nucleation) to show a power-law failure avalanche size distribution with an exponential-like taper for finite disorder. Also using renormalisation group theory, (Coniglio and Klein, 1980) demonstrate a correspondence between percolation and Ising models.

An alternative theoretical approach is to represent an existing crack front as a deformable line that advances under an external stress through a random toughness medium (*e.g.* Daguier et al., 1997). This crack front advances episodically between equilibrium states in which heterogeneities temporarily resist crack propagation. The resulting size of crack growth events depends on the competition between distortions of the crack front due to the material's inhomogeneities and the elastic self-stress field that acts to straighten this front (Bonamy and Bouchaud, 2011). Within the theory elastic fracture mechanics and in the limit of quasi-static deformations, this crack depinning process leads to failure sizes distributed as a universal power-law with a stress-dependent exponential taper (Ponson et al., 2006). This observation that some many diverse models all collapse to the same failure-size distribution is remarkable and motivates the application of statistical mechanics to seismic hazard analysis Main (1996).

This phenomena is not limited to geological materials. A wide variety of physical systems exhibit crackling noise when driven towards failure slowly (J.P. Sethna et al., 2001) and the event-size distributions are power-laws with exponential-like tapers. Also with regard to fitting observed global natural seismicity, Kagan (2002b) strongly favours a power-law with an exponential taper and a universal value for β. He also finds no statistically significant evidence for any variations in β (Kagan, 2002a).

7.1 A generalized frequency-moment distribution

Following the common form of failure-size distributions found within a wide range statistical mechanics models of brittle failure, we follow Kagan (2002b) and write a generalized distribution for earthquakes according to the seismic moment, $\mathcal{M}$, exceedence probability (survival) function:

$$P(\geq \mathcal{M}|\mathcal{M} \geq \mathcal{M}_m) = \left(\frac{\mathcal{M}}{\mathcal{M}_m}\right)^{-\beta} e^{-\zeta(\frac{\mathcal{M}}{\mathcal{M}_m}-1)}, \tag{9}$$

where $\mathcal{M}_m$ is the lower threshold for completeness in the observed catalogue and the corner moment, $\mathcal{M}_c$, characterizing the exponential taper is $\mathcal{M}_c = \mathcal{M}_m/\zeta$. As expected, for $\mathcal{M} = \mathcal{M}_m$ the exceedance probability is 1.

Within these statistical mechanics models of a fault or fracture system being driven from stability towards critical instability β is a universal constant and $\mathcal{M}_c$ evolves as a power-law relative to the system's critical point,

such that

$$\mathcal{M}_c = \frac{\mathcal{M}_m}{\zeta} \sim (\epsilon_c - \epsilon)^{-\gamma}. \tag{10}$$

Figure 10 illustrates how this survival function evolves with increasing ζ. The maximum likelihood estimator Aki (1965), with corrections for the magnitude binning (Utsu, 1965; Bender, 1983; Tinti and Mulargia, 1987) assumes $\zeta = 0$. If this is not true, the estimator becomes biased upwards. Figure 11 illustrates this bias using magnitudes simulated according to (9). When ζ scales as a critical-point function of external strain then this bias appears as a systematic and non-linear decrease in b-values. To evaluate the observed stress-dependency of earthquake magnitudes within the Groningen field we now require a suitable model for the development of stress due to depletion of reservoir pore-pressures associated with gas production.

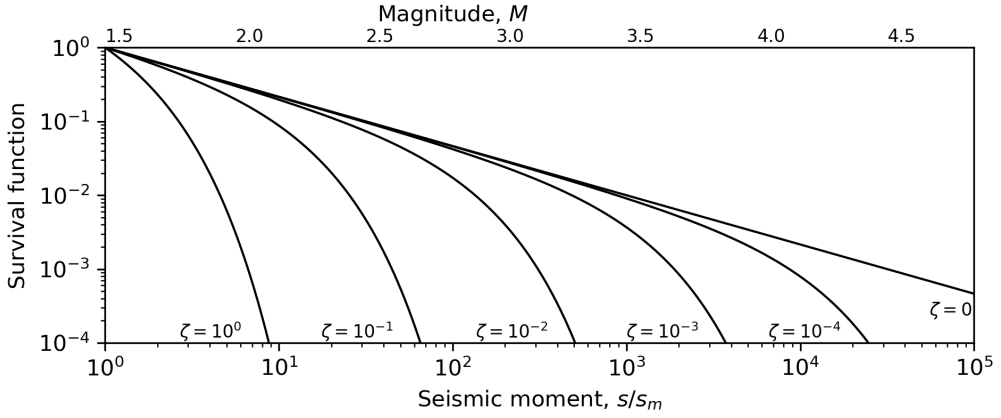

Figure 10: Seismic moment exceedance probability functions (survival functions, SF) as a power-law with an exponential cut-off according to according to equation (9) for a constant power-law exponent $\beta = \frac{2}{3}$, and a corner moment, s_c/s_m, varying from 10^{-1} to ∞, where $s_m = 2.2 \times 10^{11}$ Nm (M_{min}=1.5).

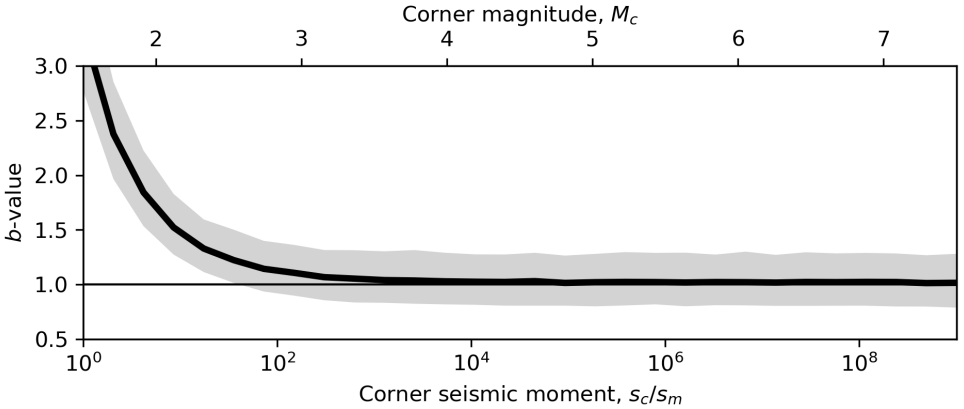

(a)

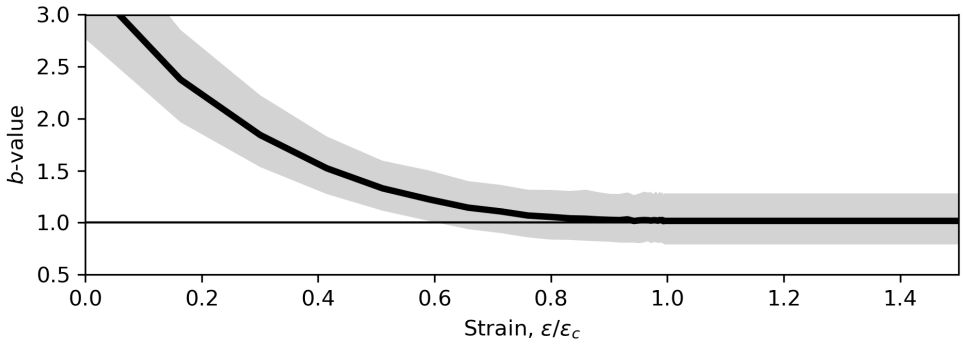

(b)

Figure 11: (a) Apparent decrease in b-value with increasing corner moment, $\mathcal{M}_c$. Based on 1000 simulated earthquake catalogues each with 50 $M \geq 1.5$ events for $\beta = \frac{2}{3}$ and a given $\mathcal{M}_c$, and then repeated for 30 different values of $\mathcal{M}_c$. The black line and grey band denote the ensemble average and 5% to 95% interval of these simulations. (b) Apparent decrease in b-value with increasing strain, ϵ relative to a critical strain, ϵ_c, according to a critical-point scaling law, $\mathcal{M}_c \sim (\epsilon_c - \epsilon)^{-\gamma}$. In this example, $\gamma = 2$.

8 Model specifications

8.1 Power-law distribution with an exponential taper

We start by representing the seismic moment, $\mathcal{M}$, as an independent random variable distributed according to a power-law distribution with an exponential taper according to:

$$P(\geq \mathcal{M}|\mathcal{M} \geq \mathcal{M}_m) = \left(\frac{\mathcal{M}}{\mathcal{M}_m}\right)^{-\beta} e^{-\zeta(\frac{\mathcal{M}}{\mathcal{M}_m}-1)}, \tag{11}$$

where β is the power-law exponent, and s_m/ζ is the corner moment of the exponential taper. For ζ=0 this distribution reduces to the power-law previously given by (3).

The associated probability density of the tapered power-law model is

$$p(\mathcal{M}|\mathcal{M} \geq \mathcal{M}_m)\, d\mathcal{M} = \frac{1}{\mathcal{M}_m}\left(\beta + \zeta\frac{\mathcal{M}}{\mathcal{M}_m}\right)\left(\frac{\mathcal{M}}{\mathcal{M}_m}\right)^{-\beta-1} e^{-\zeta(\frac{\mathcal{M}}{\mathcal{M}_m}-1)}\, d\mathcal{M}, \tag{12}$$

and the log-likelihood of this model given the set of seismic moment observations, $\mathcal{M}_i = \{\mathcal{M}_1, \ldots, \mathcal{M}_n\}$, follows as

$$\ell = \sum_{i=1}^{n}\left(\log(\beta_i + \zeta\frac{\mathcal{M}_i}{\mathcal{M}_m}) - (1+\beta_i)\log\frac{\mathcal{M}_i}{\mathcal{M}_m} - \zeta_i\left(\frac{\mathcal{M}_i}{\mathcal{M}_m} - 1\right) - \log\mathcal{M}_m + \log d\mathcal{M}\right), \tag{13}$$

as previously given by Kagan (2002b). If the observed seismic moments, $\mathcal{M}_i$, are computed from moment magnitudes according to (2) and these magnitudes are binned within intervals of size, ΔM, then the minimum seismic moment, $\mathcal{M}_m$, must be computed as

$$\log\mathcal{M}_m = \left(c + d(M_c - \frac{1}{2}\Delta M)\right)\log 10, \tag{14}$$

where M_c is the magnitude of completeness above which all events within the region of interest are reliably detected and located. We will use this one general form of the log-likelihood function for the inference and evaluation of all the different possible earthquake magnitude models considered in this study.

A complete seismological model also requires a model for event occurrence, which we shall model according to the Extreme Threshold Failure model (Bourne and Oates, 2017). Within the Extreme Threshold Failure

model, the occurrence rate of $M \geq 1.5$ events induced inside the Groningen reservoir are well-described by the Poisson intensity function

$$\lambda = h\Delta\dot{C}\theta_0 e^{\theta_1 \Delta C}. \tag{15}$$

Here, λ corresponds to the expected number of events per unit surface area and unit time. The apparent dependence on the local reservoir thickness, h, and stress rate $\Delta\dot{C}$ is not fundamental to this stress-dependent process. To clarify this, the corresponding expected event rate per unit volume and per unit of incremental Coulomb stress, χ_m, may be written as

$$\chi_m = \theta_0 e^{\theta_1 \Delta C}. \tag{16}$$

Here, χ_m characterises the stress susceptibility of the system for inducing events of at least seismic moment $\mathcal{M}_m$. Multiplying (16) and (11), yields the generalised stress susceptibility, χ, for events of at least seismic moment $\mathcal{M}$ given $\mathcal{M} \geq \mathcal{M}_m$, such that:

$$\chi = \chi_m \left(\frac{\mathcal{M}}{\mathcal{M}_m} \right)^{-\beta} e^{-\zeta(\frac{\mathcal{M}}{\mathcal{M}_m} - 1)}. \tag{17}$$

Equation (17) defines a family of seismological models for induced seismicity conditioned maximum incremental Coulomb stress field, $\Delta C(\mathbf{x}, t)$, according to the poro-elastic thin-sheet equation (4). All that remains now is to specify the functional form of any magnitude stress dependence according $\beta = \beta(\Delta C)$ and $\zeta = \zeta(\Delta C)$. We will do this by specify four distinct and physically plausible model classes: stress-invariant magnitudes, stress-dependent β-values, stress-dependent ζ-values, and stress-dependent β and ζ values.

8.2 Stress-invariant distributions

This class of stress-invariant models has up to 2 degrees of freedom, $\{\beta, \zeta\}$ where the log-likelihood function (13) takes the special case where:

$$\begin{aligned} \beta_i &= \beta, \\ \zeta_i &= \zeta. \end{aligned} \tag{18}$$

Also of interest are two special cases with single degrees of freedom. The first case is an unknown invariant power-law with zero taper, specified as

$$\begin{aligned} \beta_i &= \beta, \\ \zeta_i &= 0. \end{aligned} \tag{19}$$

The second case is an unknown invariant taper with a known universal power-law, such that

$$\begin{aligned} \beta_i &= \frac{2}{3}, \\ \zeta_i &= \zeta. \end{aligned} \tag{20}$$

These basic invariant magnitude-frequency models are all unable to explain the significant difference observed between the low- and high-stress partitions of the Groningen earthquake catalogue (Figures 4 and 5). Nonetheless, they provide useful performance references for the following two alternative classes of stress-dependent models.

8.3 Stress-dependent β-values

Within this class of models we represent the stress-dependence of the frequency-magnitude distribution according to (11) given $\zeta_i = 0$ and $\beta_i = f(\Delta C_i)$, where ΔC_i, is the maximum incremental Coulomb stress state at the occurrence time, t_i, and epicentral location, $\mathbf{x}_i$ of each event such that $\Delta C_i = \Delta C(t_i, \mathbf{x}_i)$.

As a first possible parametrization of $f(\Delta C_i)$, we will consider an inverse power-law of the form:

$$\begin{aligned} \beta_i &= \theta_0 + \left(\frac{\Delta C_i - \theta_1}{\theta_2} \right)^{-\theta_3}, \\ \zeta_i &= 0. \end{aligned} \tag{21}$$

To avoid implausibly large β-values we include the constraint $\beta_i = \min(\beta_i, 1)$. This model has 4 degrees of freedom $\{\theta_0, \theta_1, \theta_2, \theta_3\}$ where $\theta_1, \theta_2, \theta_3$ are non-negative. In general, β-values decrease with increasing Coulomb stress to the lower bound θ_0. This model has an asymptote at $\Delta C_i = \theta_1$ and so its range of physical validity is restricted to $\Delta C_i > \theta_1$. The scale and shape of the stress dependence are given by θ_2 and θ_3 respectively which are both restricted to be non-negative. For $\theta_3 = 0$ the model is stress invariant, and for $\Delta C_i \ll \theta_1 \forall i$ the model reduces to a linear function of ΔC_i equivalent to the theoretical model proposed by Scholz (1968), whilst also limiting the extent of this linear region to avoid the non-physical possibility of negative β-values.

We will also consider an alternative parametrisation of $f(\Delta C_i)$ to represent a smooth step-like transition from an upper to a lower bound with increasing stress without increasing the degrees of freedom. This is motivated by Figure 6a and previous observations of mode switching in volcanic seismicity (Roberts et al., 2016).

$$\begin{aligned} \beta_i &= \theta_0 + \theta_1 \left(1 - \tanh(\theta_2 \Delta C_i - \theta_3)\right), \\ \zeta_i &= 0. \end{aligned} \tag{22}$$

In this case, the smallest and largest possible β-values are bounded such that, $\beta_{\min} = \theta_0$, and the largest possible decrease in the β-value with increasing stress is $\beta_{\max} - \beta_{\min} = \frac{1}{2}\theta_1$. The shape and location of this smooth step down in β-values are governed by θ_2 and θ_3 respectively. The observable performance of these two stress-dependent β-value models is not greatly sensitive to the these alternative parametrization choices as they both represent a smooth non-linear approach to a lower bound. They will differ in extrapolation to earlier times with lower stress as only the second model has an upper bound. However, under extrapolation to later times with higher stress the two models become equivalent as they approach a common lower bound. For seismic hazard and risk analysis we only require this second type of extrapolation.

8.4 Stress-dependent ζ-values

Within this alternative class of stress dependent models we represent the stress-dependence of the frequency-magnitude distribution according to (11) given $\beta_i = \beta$ and $\zeta_i = f(\Delta C_i)$. As a first parametrization, we model the stress dependence of ζ according to a critical-point power-law scaling motivated by statistical fracture mechanics (Alava et al., 2006, *e.g.*), such that

$$\begin{aligned} \beta_i &= \theta_0, \\ \zeta_i &= \begin{cases} \theta_1(\theta_3 - \Delta C_i)^{\theta_2} & \text{if } \Delta C_i \leq \theta_3, \\ 0 & \text{otherwise }, \end{cases} \end{aligned} \tag{23}$$

where θ_3 is the critical stress of the system corresponding to the divergence of failure correlation length-scales and the onset of global failure. θ_2 is the non-negative critical exponent of this power-law, and θ_1 is a proportionality constant. So, as $\Delta C \to \theta_3$, then $\zeta \to 0$. This means seismic moments initiated under critical stress states are distributed as a power-law, whereas sub-critical stress states involve power-law with an exponential taper. Within this model, the power-law exponent, β, is a universal constant whilst the strength of the exponential taper decreases as stress states approach the critical point, as previously argued by Main (1995, 1996).

Given this parametrization choice, $\theta_1 = 0$ corresponds to the power-law distribution without any exponential taper, and $\theta_2 = 0$ corresponds to an exponential taper independent of the stress state. This model has 4 degrees of

freedom $\{\theta_0, \theta_1, \theta_2, \theta_3\}$. The joint posterior distribution of these parameters given the Groningen events and stress model exhibit a trade off between parameters. This may be avoided by fixing θ_1 to its maximum a posteriori probability (MAP) value, but doing so may also inadvertently bias the model.

Motivated by these findings, we consider an alternative positive definite parametrization of the ζ stress function with just 2 degrees of freedom which still allows for rapid decrease of ζ-values with increasing stress towards the critical point ($\zeta = 0$) in the form of an exponential trend:

$$\begin{aligned} \beta_i &= \theta_0, \\ \zeta_i &= \theta_1 e^{-\theta_2 \Delta C_i}. \end{aligned} \tag{24}$$

This alternative model has 3 degrees of freedom $\{\theta_0, \theta_1, \theta_2\}$. With this parametrization choice, $\theta_1 = 0$ corresponds to a pure critical-state power-law with no exponential taper for all stress states as also postulated in Main (1995, 1996).

Then for $\theta_1 = 0$, and $\theta_2 = 0$, then exponential taper is present but independent of the stress state. If both parameters are non-zero, then the exponential taper depends on the stress state, and for $\theta_2 > 0$ is follows that $\zeta \to 0$ as $\Delta C \to \infty$. So we see that this reduced parametrization if equivalent to the previous power-law choice in the limit that the critical stress point is much larger than the presently observed stress states. Although Taylor expansion of the power-law (23) under these conditions leads to a linear trend, *i.e.* $\zeta_i = \theta_1 + \theta_2 \Delta C_i$, this is not guaranteed to be positive definite without an additional constraint that creates a discontinuity in the first derivative leading to increased instability during inference. This linear form also lacks the requirement for non-linear growth in ζ with increasing sub-critical stress states. For these reasons we do not include an explicit linear parameterization for stress-dependent of ζ-values.

8.5 Stress-dependent β-ζ-values

Within this hybrid class of models we consider a 5-parameter combination of the hyperbolic-tangent stress-dependent β-model and the exponential stress-dependent ζ-model defined here as

$$\begin{aligned} \beta_i &= \theta_0 + \theta_1 \left(1 - \tanh \theta_2 \Delta C_i\right), \\ \zeta_i &= \theta_3 e^{-\theta_4 \Delta C_i}. \end{aligned} \tag{25}$$

Joint inference of the model parameters $\{\theta_0, \theta_1, \theta_2, \theta_3, \theta_4\}$ in-principle allows for competition between the two paradigms of stress-dependent β with $\zeta = 0$

and stress-dependent ζ with some universal fixed β. In practise, the limited number of observed events, the uncertainties in their magnitudes and reservoir stress states, and biased sampling of higher stress states may critically limit the statistical power of this most-complex model.

9 Bayesian inference

Adopting the established methods of Bayesian inference we will estimate the set of parameters, $\mathbf{\Theta}_i$, for each of the specified models, M_i* (Table 1), given the observed earthquake data set, $\mathbf{D}$. According to Bayes theorem:

$$\Pr(\mathbf{\Theta}_i|\mathbf{D}, M_i) = \frac{\Pr(\mathbf{D}|\mathbf{\Theta}_i, M_i)\Pr(\mathbf{\Theta}_i|M_i)}{\Pr(\mathbf{D}|M_i)}, \tag{26}$$

where $\Pr(\mathbf{\Theta}_i|\mathbf{D}, M_i \equiv P(\mathbf{\Theta}_i)$ is the posterior probability distribution of the model parameters, $\Pr(\mathbf{D}|\mathbf{\Theta}_i, M_i) \equiv L(\mathbf{\Theta}_i)$ is the likelihood distribution, $\Pr(\mathbf{\Theta}_i|M_i) \equiv \pi(\mathbf{\Theta}_i)$ is the prior distribution of parameter values, and $\Pr(\mathbf{D}|M_i) \equiv \mathcal{Z}_i$ is the normalization factor or Bayesian evidence. As $\mathcal{Z}_i$ is independent of $\mathbf{\Theta}_i$ it may be ignored for the purposes of model inference. Using standard MCMC methods provided by the Python library PyMC3 (Salvatier et al., 2015), we sample each model's parameter space distributed according to its un-normalised posterior using equilibrium Markov chains. This sampled posterior constitutes a complete joint inference of all parameter values, and may be marginalised over each parameter to yield individual parameter value estimates.

Relative to earlier studies (Bourne and Oates, 2017; Bourne et al., 2018), our MCMC sampling methods incorporate three improvements. First, the adaptive Metropolis Hastings sampler was replaced with the No-U-Turn (NUTS) sampler that provides automatic tuning of the Hamiltonian sampler and uses symbolic derivatives of the likelihood function to improve sampling efficiency and reduce correlations between successive samples. Second, single trace sampling was replaced by multiple independent trace sampling in parallel on multiple CPU and, when possible, GPU cores. Third, sample chains are initiated by random draws from the prior distribution, $\pi(\mathbf{\Theta}_i)$, rather than at the parameter values that maximize the posterior distribution, $P(\mathbf{\Theta}_i)$. This last change avoids sampling bias and assists confirmation of sample repeatability between the independent Markov chains.

*Although models and magnitudes are both denoted by the same symbol M, they may be distinguished as models are always associated with an integer subscript, M_i, whereas any magnitude subscripts are restricted to M_c and M_t representing the completeness and threshold magnitudes respectively.

In addition, the earthquake data set, $\mathbf{D}$, incorporates two improvements relative to Bourne et al. (2018). First, the seismological survey, KNMI, reduced the rounding of reported earthquake magnitude values from 0.1 to 0.01. Second, the observed time period increased by 18 months from 1/1/1995–1/1/2018 to 1/1/1995–22/5/2019 (6% increase), to incorporate another 20 $M \geq 1.5$ events within the Groningen catalogue (7% increase).

For model inference from these data, we aim to use uninformative uniform prior distributions that honour non-negative conditions where applicable. The range of these distributions are sufficiently large such that further increases do not influence the posterior distributions.

$\mathbf{M_i}$	**Equations**	**Parameters**	**Label**
Stress invariant models			
M_1	(19)	$\boldsymbol{\Theta}_1 = \{\beta\}$	uni1
M_2	(20)	$\boldsymbol{\Theta}_2 = \{\zeta\}$	uni1.z
M_3	(18)	$\boldsymbol{\Theta}_3 = \{\beta, \zeta\}$	uni2
Stress-dependent, inverse-power-law β-models			
M_4	(21)	$\boldsymbol{\Theta}_4 = \{\theta_0, \theta_1, \theta_2, \theta_3\}$	ets0.ipc4
M_5	(21$\vert\theta_1$=0)	$\boldsymbol{\Theta}_5 = \{\theta_0, \theta_2, \theta_3\}$	ets0.ipc3
Stress-dependent, hyperbolic tangent β-models			
M_6	(22)	$\boldsymbol{\Theta}_6 = \{\theta_0, \theta_1, \theta_2, \theta_3\}$	ets0.htc4
M_7	(22$\vert\theta_3$=0)	$\boldsymbol{\Theta}_7 = \{\theta_0, \theta_1, \theta_2\}$	ets0.htc3
M_8	(4), (22$\vert\theta_3$=0)	$\boldsymbol{\Theta}_8 = \{\beta_2, \beta_3, \beta_4, \theta_0, \theta_1, \theta_2\}$	ets3.htc3
Stress-dependent, critical-point scaling ζ-models			
M_9	(23)	$\boldsymbol{\Theta}_9 = \{\theta_0, \theta_1, \theta_2, \theta_3\}$	ets0.cps4
M_{10}	(23$\vert\theta_1$=10^{-4})	$\boldsymbol{\Theta}_{10} = \{\theta_0, \theta_2, \theta_3\}$	ets0.cps3
Stress-dependent, exponential trend ζ-models			
M_{11}	(24)	$\boldsymbol{\Theta}_{11} = \{\theta_0, \theta_1, \theta_2\}$	ets0.ltc3
M_{12}	(4), (24)	$\boldsymbol{\Theta}_{12} = \{\beta_2, \beta_3, \beta_4, \theta_0, \theta_1, \theta_2\}$	ets3.ltc3
Stress-dependent β-ζ-models			
M_{13}	(25)	$\boldsymbol{\Theta}_{13} = \{\theta_0, \theta_1, \theta_2, \theta_3, \theta_4\}$	ets0.b3.z2
M_{14}	(4), (25)	$\boldsymbol{\Theta}_{14} = \{\beta_2, \beta_3, \beta_4, \theta_0, \theta_1, \theta_2, \theta_3, \theta_4\}$	ets3.b3.z2

Table 1: Summary of the different seismological magnitude-frequency models, M_i, evaluated according to their posterior, out-of-sample, predictive performance. The labels are composed by string to represent a model type and a following digit to denote the associated degree of freedom. For instance, ets0.htc3 denotes the MAP elastic thin-sheet model with zero degrees of freedom combined with the hyperbolic tangent of incremental Coulomb stress model with 3 degrees of freedom to represent a stress-dependent β-value.

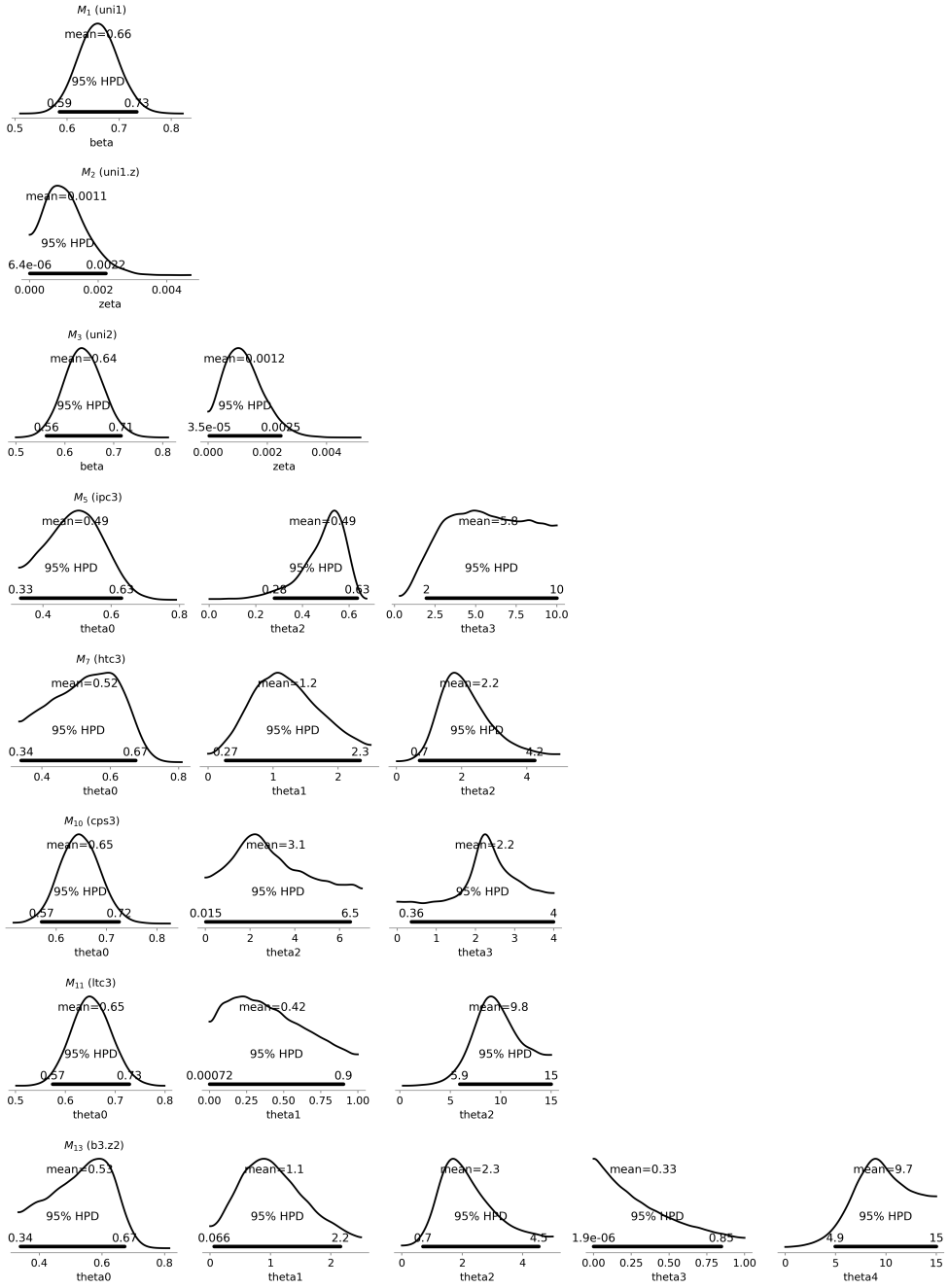

Figure 12: Marginal posterior probability density distributions inferred for each model given the observed magnitudes of $M \geq 1.5$ events from 1995 to 2019. Thick horizontal lines denote the 95% credible interval defined by the highest posterior density (HPD) interval.

9.1 Stress-invariant models

We trained the power-law distribution with an exponential taper model with constant β- and ζ-values as specified by (18) with uniform prior distributions: $0.3 \leq \beta \leq 1$, and $0 \leq \zeta \leq 1$. The resulting joint posterior probability density (Figure 13) indicates a β value consistent with its typically observed value, $\beta = 2/3$, and a non-zero ζ-value consistent with the presence of an exponential-taper on the power-law distribution of seismic moments within the Groningen catalogue. The posterior distribution obtained is characterized by the following mean values and 95% credible intervals defined by the highest posterior density:

$$\begin{aligned} \bar{\beta} &= 0.64 && (0.56 < \beta < 0.71) \\ \bar{\zeta} &= 1.2 \times 10^{-3} && (3.5 \times 10^{-5} < \zeta < 2.5 \times 10^{-3}) \end{aligned} \tag{27}$$

This is consistent with the usually-observed value of $\beta = 2/3$ and the presence of an exponential taper ($\zeta > 0$). The joint posterior probability density distribution (Figure 13) indicates no evidence for any strong covariance between the inferred β- and ζ-values that would appear as a clear diagonal trend in the distribution. That is lower than average β-values are equally likely to be paired with lower or higher than average ζ-values and vice-versa.

9.2 Stress-dependent β-models

9.2.1 Inverse power-law β-model

The posterior distribution of parameter values for the inverse power-law β-model specified according to (21) was sampled subject to uniform prior distributions, $1/3 \leq \theta_0 \leq 1$, $\theta_1 = 0$, $0 \leq \theta_2 \leq 1$, and $0 \leq \theta_3 \leq 10$. Our choice of this θ_0 lower bound reflects the absence of lower values in prior observations of stress-dependent b-values reported elsewhere (Mori and Abercrombie, 1997; Wiemer and Wyss, 1997, 2002; Schorlemmer et al., 2005; Gulia and Wiemer, 2010; Spada et al., 2013; Huang et al., 2018). The joint posterior probability density distribution (Figure 14) indicates a bounded distribution with well-sampled and highly correlated uncertainties, and localised MAP values.

The posterior distribution obtained is characterized by the following mean values and 95% credible intervals (HPD).

$$\begin{aligned} \bar{\theta}_0 &= 0.49 && (0.33 < \theta_0 < 0.63) \\ \bar{\theta}_2 &= 0.49 && (0.28 < \theta_2 < 0.63) \\ \bar{\theta}_3 &= 5.77 && (1.96 < \theta_3 < 10.0) \end{aligned} \tag{28}$$

This apparent variation with stress may be a statistical artefact of neglecting stress variations in ζ as illustrated in Figure 11. The posterior ensemble β function of incremental Coulomb stress (Figure 19a) are consistent with the previous finding of a significant difference between the frequency-magnitude distribution of events occurring under stress states below and above $\Delta C = 0.7$. Joint optimization of this magnitude-frequency model and the poro-elastic thin-sheet model with its three degrees of freedom (σ, $r_{\max}$, H_s), yields a similar ensemble function (Figure 19c) albeit with a broader prediction interval reflecting the additional variabilities within this ensemble stress model.

9.2.2 Hyperbolic tangent β-model

The posterior distribution of parameter values for the hyperbolic tangent β-model specified according to (22) was sampled subject to uniform prior distributions, $1/3 \leq \theta_0 \leq 1$, $0 \leq \theta_1 \leq 2.5$, $0 \leq \theta_2 \leq 5$, and $\theta_3 = 0$. The joint posterior probability density distribution (Figure 15) once again indicates a bounded distribution with singular MAP values.

The posterior distribution obtained is characterized by the following mean values and 95% credible intervals (HPD).

$$\begin{aligned} \bar{\theta}_0 &= 0.52 \qquad (0.34 < \theta_0 < 0.67) \\ \bar{\theta}_1 &= 1.2 \qquad\quad (0.27 < \theta_2 < 3.2) \\ \bar{\theta}_2 &= 2.2 \qquad\quad (0.7 < \theta_3 < 4.2) \end{aligned} \tag{29}$$

Under this alternative parametrization of the stress-dependent β-model, the correlation structures between the parameters do differ but a lead to similar evidence of apparent stress-dependence. The associated ensemble β-function of stress (Figure 19b) appears broadly similar to the inverse-power law model, with the largest differences limited to the lowest stress states. We attribute this to sampling bias as the observed events are significantly more prevalent under the higher stress states leaving few observations to constrain this low-stress response. Joint optimization of this magnitude-frequency model with the thin-sheet stress model leads to similar results once more (Figure 19d), and again with increased variability associated with counting the uncertainty in our knowledge of the stress states associated with each event.

9.3 Stress-dependent ζ-models

9.3.1 Power-law ζ-model

For the power-law ζ-model specified by (23), and given the constraint $\theta_1 = 1$, the posterior distribution obtained is characterized by the following mean values and 95% credible intervals (HPD).

$$\begin{aligned} \bar{\theta}_0 &= 0.65 \qquad (0.57 < \theta_0 < 0.72) \\ \bar{\theta}_2 &= 3.15 \qquad (0.02 < \theta_2 < 6.48) \\ \bar{\theta}_3 &= 2.24 \qquad (0.36 < \theta_3 < 4.00) \end{aligned} \tag{30}$$

We set the constraint $\theta_1 = 1$ to avoid a trade-off found with θ_2 that is likely due to the limitations of finite sample size and under-sampling of the seismogenic response to lower stress states (see $\Delta C < 0.5$ in Figure 2). This constraint does not affect the subsequent out-of-performance of this model, but simplifies the posterior distribution. The estimated β-value, θ_0, is consistent with a universal value of $\beta = 2/3$. The posterior distribution of θ_3 takes values that are mostly larger than ΔC_i corresponding to $\zeta > 0$ reflecting the presence of an exponential taper to the power-law distribution of seismic moments. Furthermore, as the 95% confidence interval for θ_2 excludes $\theta_2 = 0$, there is significant evidence for ζ decreasing with increasing Coulomb stress in accord with the critical point scaling laws of statistical fracture mechanics.

9.3.2 Exponential ζ-model

Within the exponential ζ-model defined by (24) the sampled posterior distributions (Figure 17) yield mean values and 95% credible intervals (HPD) as follows.

$$\begin{aligned} \bar{\theta}_0 &= 0.65 \qquad (0.57 < \theta_0 < 0.73) \\ \bar{\theta}_1 &= 0.42 \qquad (0.001 < \theta_1 < 0.93) \\ \bar{\theta}_2 &= 9.33 \qquad (5.9 < \theta_2 < 14.8) \end{aligned} \tag{31}$$

These results are insensitive to our choice of uniform prior distributions. The estimated β-value, θ_0, is once more consistent with the usually observed β-value of 2/3. These results also reveals significant evidence for $\theta_1 > 0$ which again reflects confidence about the presence of an exponential taper of the power-law seismic moment distribution. In addition, $\theta_2 > 0$ is a significant finding consistent with a stress-dependent exponential taper where ζ decreases under increasing Coulomb stress (Figure 20).

9.4 Stress-dependent β-ζ-models

Within the hybrid model that combines both β- and ζ stress dependence as defined by (24) the sampled posterior distributions remain stable with unique and localized MAP values (Figure 17). The associated mean values and 95% credible intervals:

$$\begin{aligned} \bar{\theta}_0 &= 0.53 \qquad (0.34 < \theta_0 < 0.67) \\ \bar{\theta}_1 &= 1.1 \qquad (0.07 < \theta_1 < 2.2) \\ \bar{\theta}_2 &= 2.3 \qquad (0.7 < \theta_2 < 4.5) \\ \bar{\theta}_3 &= 0.33 \qquad (0 < \theta_3 < 0.85) \\ \bar{\theta}_4 &= 9.7 \qquad (4.9 < \theta_4 < 15) \end{aligned} \tag{32}$$

indicate significant in-sample evidence for stress dependence of both β- and ζ-values.

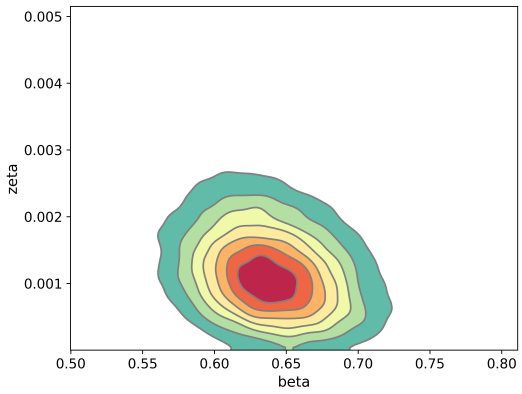

Figure 13: The joint posterior distribution of the stress-invariant β- and ζ-model (M_3, uni2) obtained given the observed magnitudes of $M \geq 1.5$ events from 1995 to 2019. These sampled distributions are represented by Gaussian kernel densities that introduce some data-adaptive smoothing.

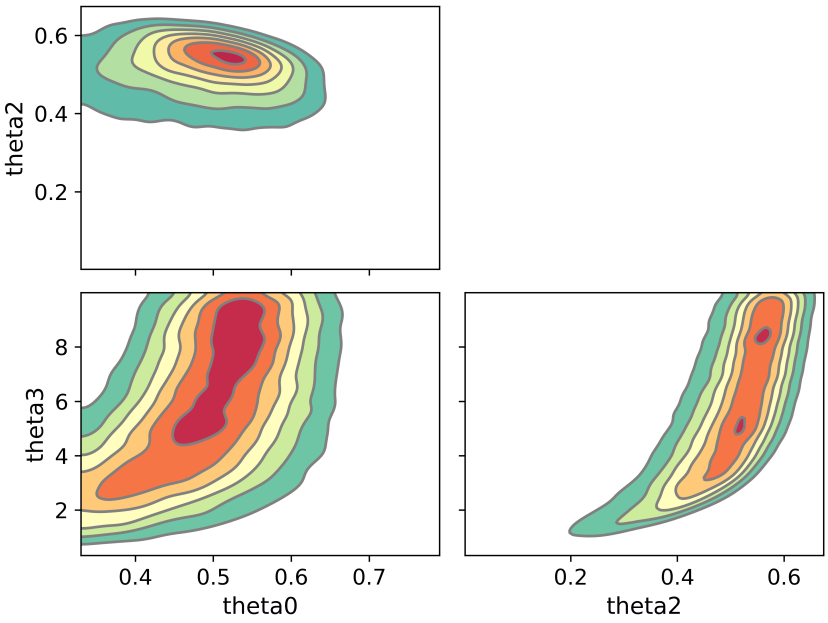

Figure 14: Pairwise joint posterior distributions of the inverse power-law β-model parameters given (M_5, ets0.ipc3) inferred given $\theta_1 = 0$ and the MAP poro-elastic thin-sheet model ($\sigma = 3.5$ km, $r_{\max} = 1.1$, $H_s = 10^7$ MPa) and the observed catalogue of $M \geq 1.5$ earthquakes from 1-Jan-1995 to 1-Jan-2019. There is stronger evidence of covariance given the less-than-circular joint density maps.

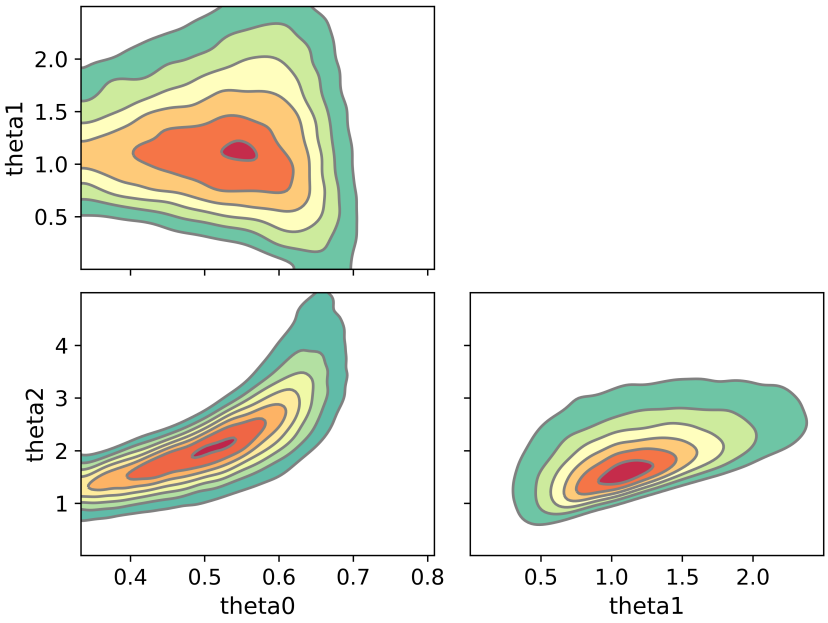

Figure 15: Pairwise joint posterior distributions of the hyperbolic tangent β-model parameters (M_7, ets0.htc3) inferred given $\theta_3 = 0$ and the MAP poro-elastic thin-sheet model ($\sigma = 3.5$ km, $r_{\max} = 1.1$, $H_s = 10^7$ MPa) and the observed catalogue of $M \geq 1.5$ earthquakes from 1-Jan-1995 to 1-Jan-2019.

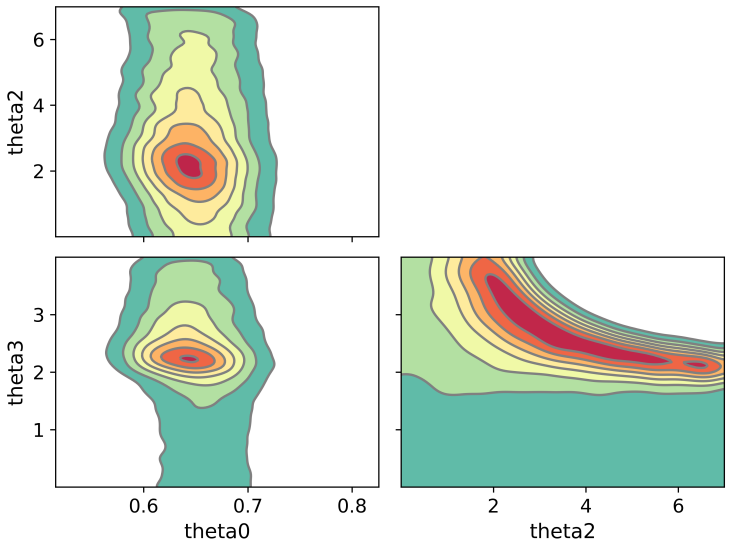

Figure 16: Pairwise joint posterior distributions of inverse power-law stress-dependent ζ-model parameters (M_{10}, ets0.cps3) defined according to (23) given the additional constraint $\theta_1 = 0$.

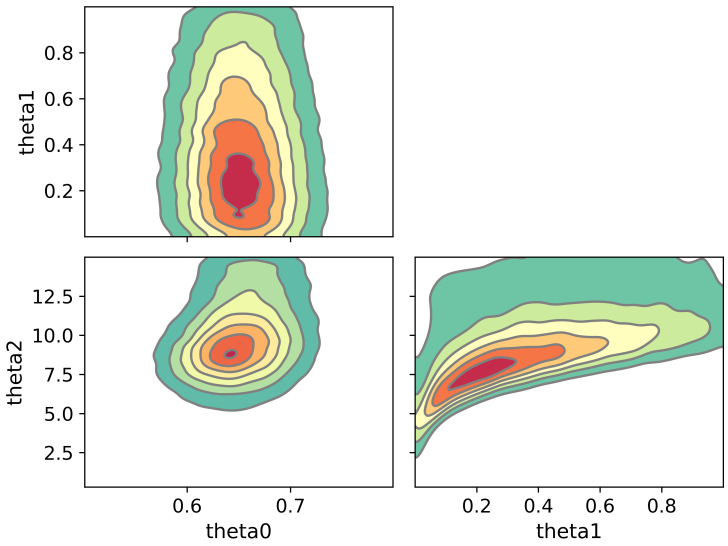

Figure 17: Pairwise joint posterior distribution of the exponential stress dependent ζ-model parameters (M_{11}, ets0.ltc3) defined according to (24).

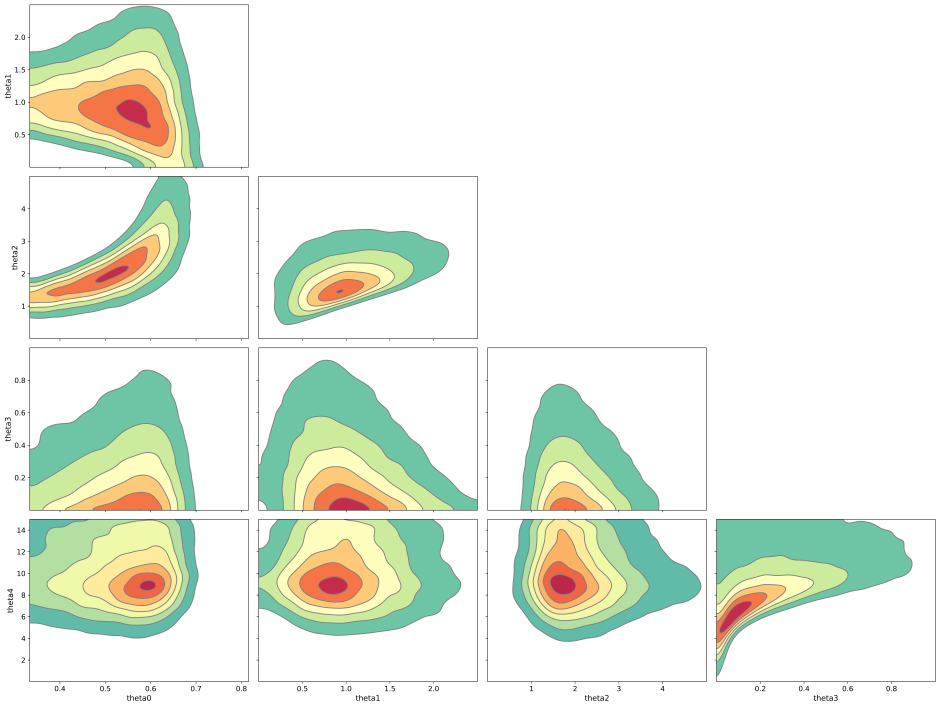

Figure 18: Pairwise joint posterior distributions of the stress-dependent β-ζ-model parameters (M_{13}, ets0.b3.z2) defined according to (25).

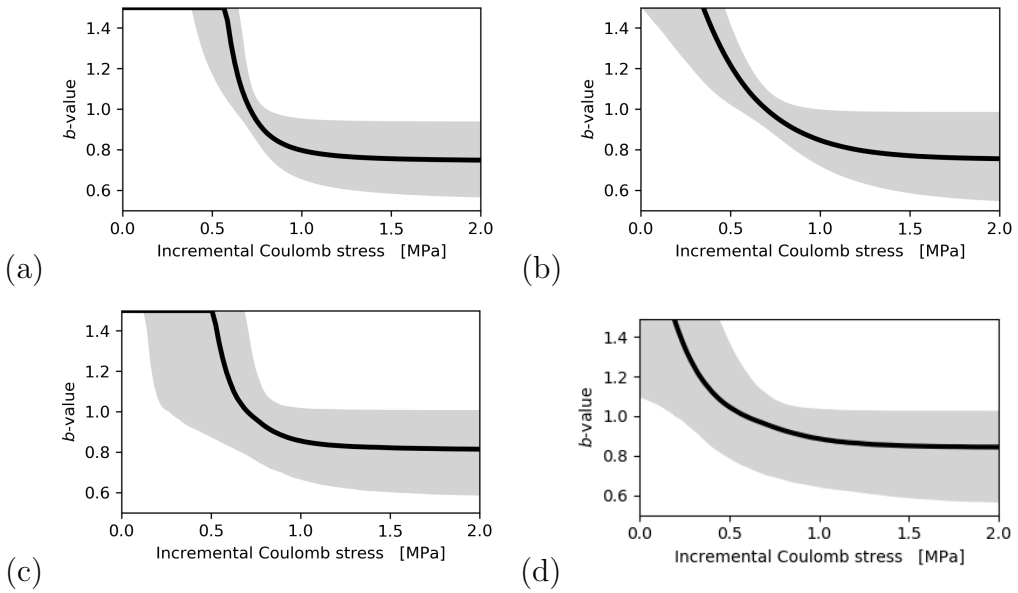

Figure 19: Posterior ensemble b-value functions of incremental Coulomb stress according to (a) the inverse power-law (M_5, ets0.ipc3), and (b) the hyperbolic tangent (M_7, ets0.htc3) model distributions shown by Figures 14 and 15 respectively. (c) As (a), except including the full posterior distribution of pore-elastic thin-sheet parameters, σ, $r_{\max}$, H_s (ets3.ipc3). (d) As (c), except for the hyperbolic tangent model (M_8, ets3.ipc3). Note that b-values are shown instead of β-values, where $b = 1.5\beta$. Black curves and grey shading denote the median and 95% prediction intervals respectively.

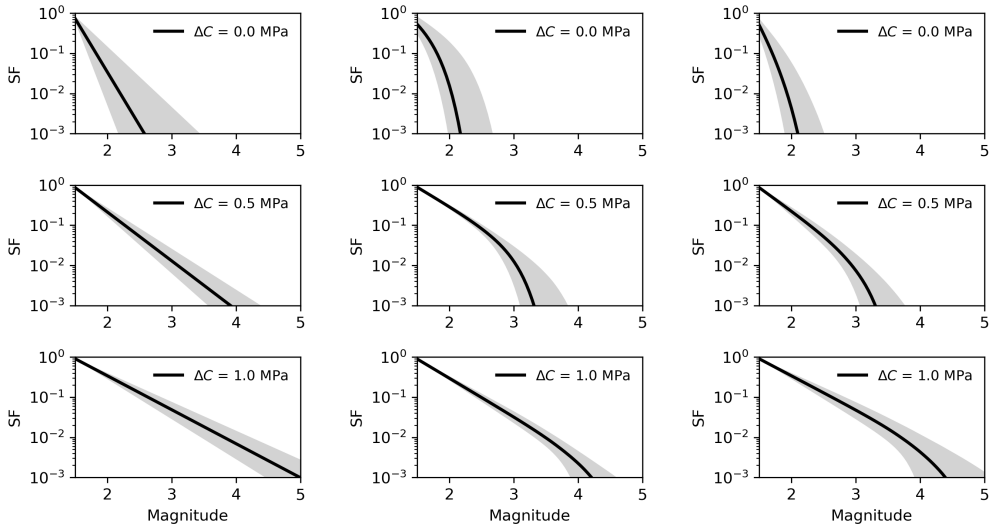

Figure 20: Evolution of the modelled magnitude survival function, SF, illustrated by three stress states, $\Delta C = 0, 0.5, 1$ MPa for a stress-dependent β-model (left, M_7), stress-dependent ζ-model (middle, M_{11}), and the stress dependent β-ζ-model (right, M_{13}). These ensemble functions are summarized by their medians (black), and 95% prediction intervals (grey).

10 Model characteristics

Figure 21 illustrates how the stress susceptibility, χ_s defined by equation (17), varies with Coulomb stress, ΔC, according to the different magnitude-frequency models. The particular instance of each model was selected according to MAP parameter values given the observed Groningen events and poro-elastic thin-sheet stress model. The different lines in each plot show how stress susceptibility varies for different magnitude thresholds. All models share the fundamental property of monotonic increases in susceptibility with stress, so in all plots every line moves up to the right. Looking beyond this similarity, there are key and distinguishing differences between each of these magnitude-frequency models.

For the simplest magnitude-frequency model of a constant β and no exponential taper, $\zeta = 0$ (Figure 21a), all susceptibility lines are straight, parallel

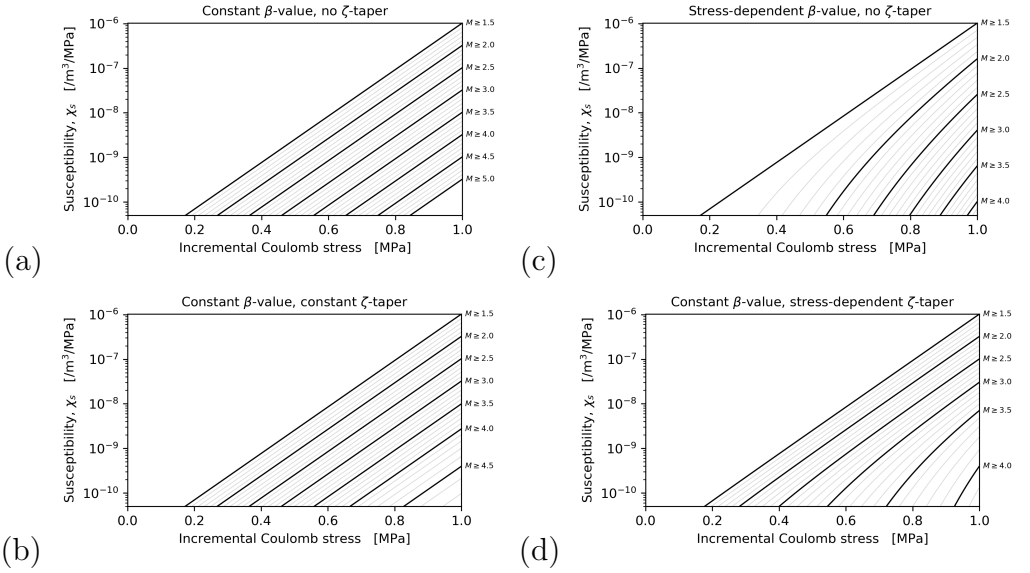

Figure 21: The expected rate, χ, of events of at least magnitude, M per unit reservoir volume and stress increment increases with incremental Coulomb stress under four alternative models: (a) stress-invariant model with $\beta = 2/3$ and $\zeta = 0$ (M_1), (b) stress-invariant model with $\beta = 2/3$ and $\zeta > 0$ (M_3), (c) stress-dependent β with $\zeta = 0$ (M_7), (d) stress-dependent ζ with $\beta = 2/3$ (M_{12}). Lines denote different magnitude thresholds from 1.5 to 5.0 in intervals of 0.1 (grey) and 0.5 (black). Each model (Table 1) is based on its MAP values inferred using the observed 1995–2019 $M \geq 1.5$ events and the poro-elastic thin-sheet stress model.

and equally-spaced on this log-linear plot. These lines remain straight and parallel because the model is invariant under increasing stress, and they remain equally spaced because frequency-moment distribution is a pure power-law. With the introduction of a stress-invariant exponential taper, $\zeta > 0$ (Figure 21b), these lines remain parallel reflecting the stress invariance of the model, but the line spacing increases with the magnitude threshold and rapidly so above the corner magnitude as the exponential tail dominates. In this example the corner magnitude is 3.5. The key difference between these two stress-invariant magnitude-frequency models is the expected rate of larger magnitude events at larger incremental stress states (lower right corner of these plots). For example, the emergence of $M \geq 4.5$ susceptibility rates above 0.5×10^{-10} /m^3/MPa (stress-axis intercept) increases from 0.75 MPa to 0.85 MPa by including the exponential taper. This highlights the importance of any non-zero taper for induced seismicity hazard and risk analysis that are typically driven by larger than previously seen magnitudes under larger than previously experienced stress states.

Under both stress-dependent models (Figure 21c, d), these lines are neither straight, nor parallel nor equally spaced. The only common feature is the top line corresponding to the rate of $M \geq 1.5$ events which follows the same Extreme Threshold exponential trend given by (16) in all models. The stress-dependent β-model with no taper (Figure 21c) has a constant line space for any given incremental stress. This is most easily recognized on the right side of the plot but is true everywhere. This line spacing decreases with stress, reflecting the smaller β-values at larger stresses. This means the largest line spacings occur for the smallest magnitudes at the smallest stress states (lower left corner). Consequently, look along the stress axis, $\chi_s = 0.5 \times 10^{-10}$ /m^3/MPa, the line spacing decreases with stress. This means the additional stress required to exceed the next magnitude threshold becomes progressively *smaller* as the system evolves to higher stress states.

The opposite is true for the stress-dependent ζ-model with a constant β-value (Figure 21d). Along the stress-axis, line spacings increase with stress. This indicates the additional stress required to exceed the next magnitude threshold becomes progressively *larger* as the system evolves to higher stress states. Consequently the largest line spacings occur for the largest magnitude thresholds at the largest stress states (lower right corner). The key distinguishing feature of these two stress-dependent models is the intercept of each line on the incremental Coulomb stress axis.

11 Model evaluation

We take two complimentary approaches to evaluating model performance for forecasting event magnitudes. The first compares out-of-sample posterior model likelihood distributions for the most recent subset of observed events (2012–2019). The second compares the observed and model-based simulations of maximum magnitude and total seismic moment time series over the entire history of gas production (1965–2019).

11.1 Out-of-sample likelihoods

We favour out-of-sample over in-sample likelihoods as a better measure of the forecast performance required by seismic hazard and risk analysis. Typical hazard and risk analysis periods for Groningen induced seismicity are 5 to 10 years and are always beyond the current observation period (Elk et al., 2019). This means seismicity forecasts rely on near-term extrapolations of the seismological models conditioned on a given gas production scenario. We therefore choose to exclude all in-sample model evaluation methods, such as the Bayesian Information Criterion, as these do not properly reflect this out-of-sample forecast requirement.

The most reliable measure of forecast performance is a blind prediction made prior to the observations required to evaluate forecast performance. In our case, this means waiting for at least 5 years. To avoid such a delay, we evaluate out-of-sample model performance using the existing observations. To do this, we divide the observed earthquake data set, $\mathbf{D}$, into two disjoint, time-contiguous parts, $\mathbf{D}_1$ and $\mathbf{D}_2$, corresponding to a training period, $\mathcal{T}_1$, and an evaluation period, $\mathcal{T}_2$. In this study, when not specified otherwise, these periods are $\mathcal{T}_1 = 1/1/1995$ to $31/12/2012$, and $\mathcal{T}_2 = 1/1/2013$ to $1/6/2019$. This choice splits the data into approximately two equal parts, and also ensures the evaluation period covers at least 5 years to represent the typical forecast demand for these seismological models. This is a form of cross-validation where the choice of out-of-sample data is restricted to reflect the forecast requirement. This is a retrospectively blind test where the choice of the start time for the out of sample future events was made prior to, and independent from, the later analysis. Nonetheless there remains a residual possibility of unconscious researchers' bias influencing our analysis. Indeed, true forecast performance typically lags behind hindcast performance within meteorological models.

To evaluate out-of-sample model performance we first sample the posterior joint model parameter distribution, $P(\mathbf{\Theta}_i)$, given $\mathbf{D}_1$ according to (26). Then we sample the out-of-sample posterior predictive distribution of like-

lihood values, $L(\mathbf{D}_2|\mathbf{\Theta}_i)$, for the $\mathbf{D}_2$ data set given the sampled posterior distribution $P(\mathbf{\Theta}_i)$ obtained in the first step. These results are summarized by the distribution of log-likelihood values evaluated as

$$\ell_i = \log L(\mathbf{D}_2|\mathbf{\Theta}_i). \tag{33}$$

By this measure, every model has zero degrees of freedom to explain the out-of-sample observations, $\mathbf{D}_2$, as it is not fitted to these data. Models with too many degrees of freedom will tend to yield posterior distributions that overfit the in-sample observations, $\mathbf{D}_1$, with highly variable parameter values. This likely increases bias and reduces precision in model-based forecasts for the out-of-sample observations, $\mathbf{D}_2$, which systematically reduces the out-of-sample log-likelihood values obtained according to equation (33). Likewise, models with too few degrees of freedom, will likely fail to fit enough of the observed variations within $\mathbf{D}_1$ and carry-over this deficiency. Limitations associated with small sample sizes may confound this evaluation due to chance effects that increase performance variability and broaden the measured out-of-sample log-likelihood distribution. This limits our ability to reliably rank the model when their log-likelihood distributions overlap.

Instead, we use these distributions to measure the probability, P_{ij}, of one model, M_i, out-performing another model, M_j, according to the probability of ℓ_i exceeding ℓ_j:

$$P_{ij} = \Pr(\ell_i > \ell_j). \tag{34}$$

This probability P_{ij} is estimated by the fraction of randomly sampled pairs from their respective distributions that satisfy this criterion. Posterior distribution sample sizes are made large enough to ensure sampling errors, ΔP_{ij} are insignificant when comparing models (*e.g.* $\Delta P_{ij} < 0.01$). This was verified but increasing the sample size to demonstrate the results at this level of precision are reproduced. Accordingly, self-comparison of any model yields $P_{ii} = 0.5$.

Figure 22a shows the out-of-sample log-likelihood distributions obtained for the three stress invariant models. Better performance appears as larger log-likelihood values so the best and worst versions of a model are found in the upper and lower tails of these distributions respectively. As the distributions all overlap the ranking of model performance is somewhat ambiguous. So although the best performances are associated with the upper tail of the M_3, the upper tails of M_1 and M_2 still exceed the performance of the lower tail of M_3. Nonetheless, the two models that allow for the presence of an exponential taper, $\zeta \neq 0$ (M_2, M_3), are both capable of better performance than the baseline model without any exponential taper ζ=0 (M_1) as shown by the locations of their upper tails. Likewise, all stress-dependent models

also exhibit better performance than the baseline model M_1 (Figure 22b) as their upper tails all exceed the upper tail of M_1. However, within these models the performance gain of an exponential taper appears much less clear as the three models with the best performing upper tails include two with $\zeta = 0$ (M_5, M_7), and one that combines stress-dependent β and ζ effects (M_{13}).

The complete $\mathbf{D}_2$ data are dominated by the smallest magnitude events, so for instance half of the observed events are in the range $1.5 \leq M \leq 1.8$ compared to the largest observed magnitude at $M = 3.6$. Since these models are intended for probabilistic seismic hazard and risk assessment their performance in forecasting larger magnitude events must be considered. We start to do this by increasing the magnitude threshold, M_t, for the events admitted into the $\mathbf{D}_2$ data set to obtain the subset $\mathbf{D}_{2t}$. Then the out-of-sample likelihood analysis is repeated using the same posterior distributions of parameter values as before, $P(\mathbf{\Theta}_i)$, to evaluate the out-of-sample likelihood values $L_t(\mathbf{D}_{2t}|\mathbf{\Theta}_i)$. The modified likelihood function, L_t, is given by equations (13) and (14) where $M_c = M_t$. In this manner the models are still trained by all $M \geq 1.5$ events within the training data but then evaluated only on the larger $M \geq M_t$ events within the out-of-sample evaluation data.

Figure 23 shows the likelihood distributions obtained for magnitude thresholds $M_t = \{1.75, 2.0, 2.5\}$. Once more, the better performing models are

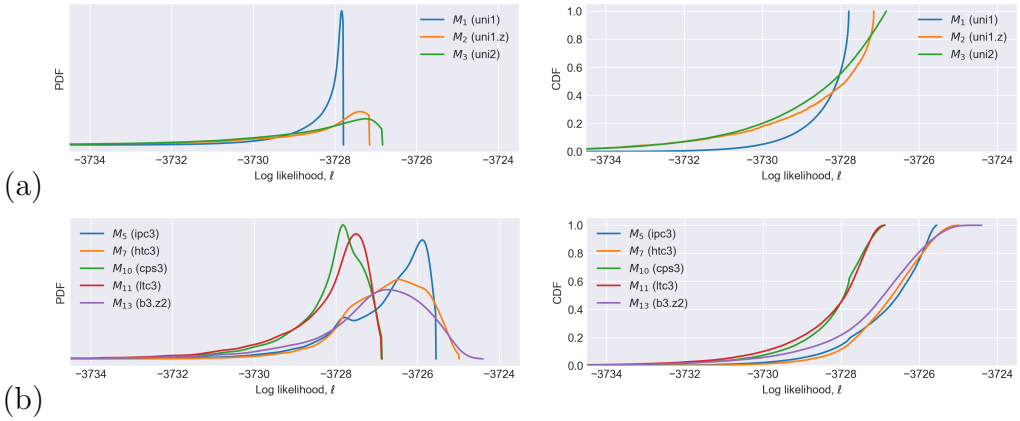

Figure 22: Out-of-sample forecast performance of each alternative magnitude-frequency models (Table 1) measured as the log likelihood distribution, ℓ, of the 1/1/2012 to 1/6/2019 observed $M \geq 1.5$ events, given the posterior distribution of models inferred from the observed 1995–2012 events. (a) Stress invariant models $\{M_1, M_2, M_3\}$. (b) Stress-dependent models $\{M_5, M_7, M_{10}, M_{11}, M_{13}\}$.

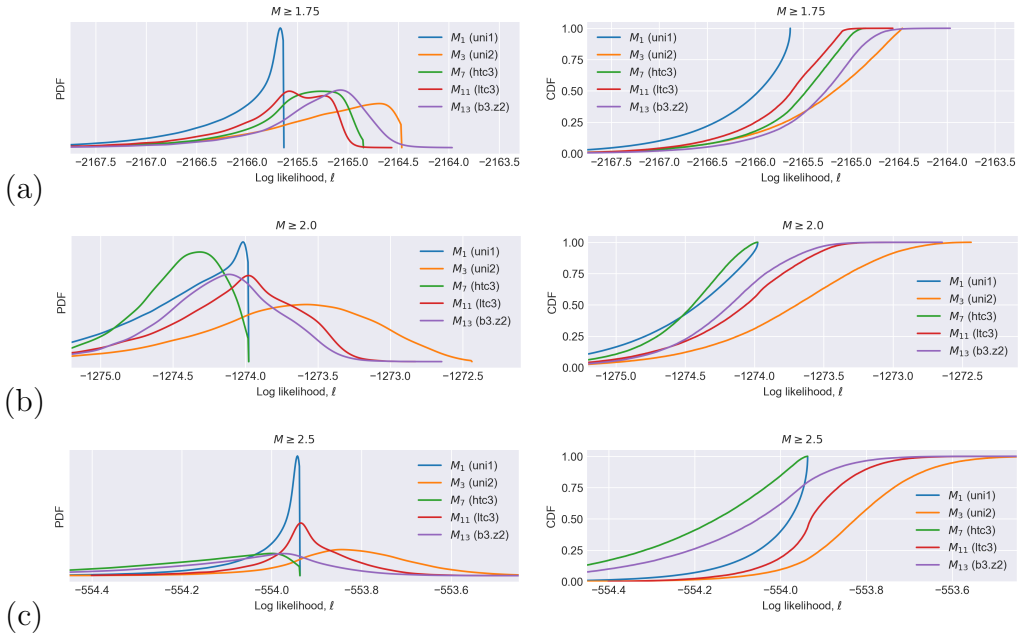

Figure 23: Out-of-sample forecast performance of each magnitude-frequency models (Table 1) measured as the the log likelihood distribution, ℓ, of the 1/1/2012 to 1/6/2019 observed (a) $M \geq 1.75$, (b) $M \geq 2.0$, and (c) $M \geq 2.5$ events, given the posterior distribution of models inferred given the observed 1995–2012 events.

Model class		M_i	P_{i1}, Probability of M_i out-performing M_1			
			$M \geq 1.5$	$M \geq 1.75$	$M \geq 2.0$	$M \geq 2.5$
Stress invariant	uni1	M_1	0.500	0.500	0.500	0.500
	uni1.zeta	M_2	0.587	0.950	0.955	0.996
	uni2.zeta	M_3	0.516	0.839	0.846	0.891
Stress-dependent β	ets0.ipc3	M_5	0.909	0.874	0.454	0.157
	ets0.htc3	M_7	0.901	0.836	0.571	0.212
Stress-dependent ζ	ets0.cps3	M_{10}	0.638	0.698	0.666	0.695
	ets0.ltc3	M_{11}	0.692	0.768	0.726	0.748
Stress-dependent β-ζ	ets0.b3.z2	M_{13}	0.872	0.899	0.754	0.414

Table 2: Out-of-sample magnitude forecast performance measured according to the probability of each model out-performing the baseline model of a stress-invariant β-values with ζ=0 (M_1). Models were trained using the observed 1/2012–6/2019 $M \geq 1.5$ events and evaluated using the observed 1/2012–6/2019 $M \geq M_t$ events, where $M_t = \{1.5, 1.75, 2.0, 2.5\}$. Colours vary from red to yellow to green denoting probabilities from 0 to 0.5 to 1 respectively.

located within the upper tails of each distribution. Table 2 summarise the performance of all models relative to the baseline model, M_1, according to the P_{i1} metric as specified by (34). As the magnitude threshold increases, it is clear that the performance of ζ=0 models significantly decreases from a top-ranked performance for $M \geq 1.5$ to a bottom-ranked performance for $M \geq 2.5$. Furthermore, the only models that fail to exceed the baseline model performance ($P_{i1} \leq 0.5$) are those with a stress-dependent β-values (M_5, M_7, M_{13}). This indicates that β-values which decrease with increasing Coulomb stress do not describe the tail of the observed magnitude distribution as well as any of the other models which all possess stress-invariant β-values.

In contrast, the performance of $\zeta \neq 0$ models with constant β-values either improve (M_2, M_3) or remain stable (M_{10}, M_{11}) under increasing magnitude thresholds. As expected, the presence of an exponential taper measurably improves the out-of-sample forecast performance for $M_t \geq 2$ events. However, within this analysis, there is no evidence for stress-dependent ζ-values as stress-invariant $\zeta \neq 0$ models perform marginally better against the baseline model for $M_t \geq 2$.

11.2 Simulated seismic moments and magnitudes

Simulation of event catalogues using the different magnitude-frequency models allows their performance to be evaluated regarding the time series of maximum magnitudes and total seismic moment time series. Such an evaluation differs from the previous consideration of out-of-sample likelihood given the observed magnitudes by testing the simulation results and placing greater emphasis on forecasting the larger magnitudes that most-influence seismic hazard and risk analysis. The time series of total seismic moments represents the cumulative sum of seismic moments for all prior $M \geq 1.5$ events. Likewise, the time series of maximum magnitudes represents the largest magnitude observed so far. These simulated time series depend on both the simulated number and magnitude of events. Over the typical range of β-values associ-

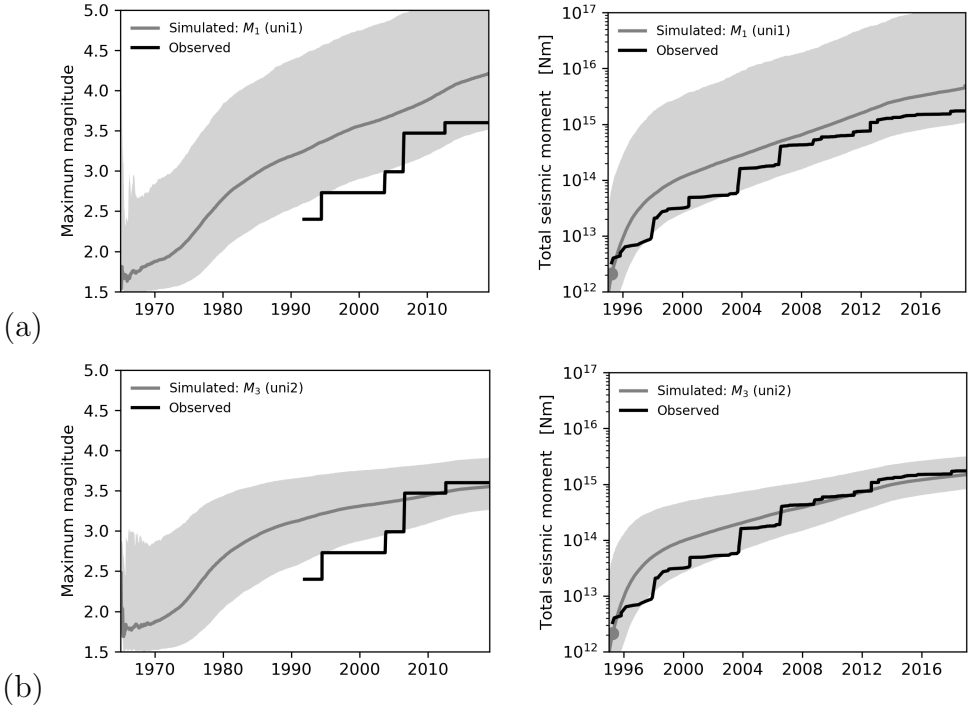

Figure 24: Time series of observed and simulated maximum magnitudes (left) and total seismic moments (right) for two stress-invariant models: (a) stress-invariant β given ζ=0, M_1, and stress-invariant β-ζ-model, M_3. Given the absence of field-wide $M \geq 1.5$ earthquake monitoring until 1995, the total seismic moment time series start in 1995. Dark grey lines, and light grey regions denote the simulated median values and 95% prediction intervals respectively.

ated with this seismicity most of the total seismic moment is contributed by the maximum magnitude event. As such, both time series are closely related, but with one key distinction. The total seismic moment in 1995 is unknown whereas the maximum magnitude is known to be $M_{\max} = 2.4$ from a regional monitoring network reporting all $M \geq 2$ events.

Figures 24 and 25 compare the observed and simulated time series of maximum magnitudes and total seismic moments for 2 stress invariant and 3 stress-dependent magnitude-frequency models. All these results share the same event occurrence simulations based on the posterior distribution of Extreme Threshold Failure models (Bourne and Oates, 2017). The posterior distribution of all models were obtained using the just $\mathbf{D}_1$ so the out-of-sample observations in this case occur prior to 1/1/1995 and from 1/1/2013. The simulations were run from 1965 to 2019 using the reservoir pore pressure model.

...Are these just fits to the whole data set, or are these fit on date from 1993-2012 and then run forward and back in time with the reservoir compaction model for seismicity generation? This needs to be made explicit. It is interesting that the uncertainty diminishes with time on the lower plots as more data are obtained, and that the lower right plot has the greatest accuracy and precision in recent years.

The model of stress-invariant β-values given ζ=0 (M_1, uni) systematically over-predicts both time series for all observed events and exceeds the 95% prediction interval for maximum magnitudes. Maximum magnitude time series residuals (Figure 26) indicate the absolute mean residual ($\Delta M_{\max} = -0.5$) is significantly larger than the expected magnitude measurement error ($\pm$ 0.1–0.2). The upper bound of the 95% prediction interval is always about 2 magnitude units above the observed maximum magnitude. A similar over-prediction bias is seen in the total seismic moments time series where the median time series always exceeds the observed total seismic moment after 1996. Including a stress-invariant taper of the frequency-magnitude distribution (M_3) significantly reduces the simulation bias whilst also significantly increasing its precision. This is shown by the reduced width of the 95% prediction interval that still contains all the variability in the observed total seismic moment time series although the first half of the time series (1995-2007) is systematically over-predicted. This early over-prediction bias is also seen in the maximum magnitudes time series and even exceeds the 95% prediction interval. The appearance of increasing precision with time does not reflect the increase observational constraints but instead appears due to the influence of the stress-invariant exponential taper that starts to significantly lower the probability of $M \geq 3.5$ events.

The inverse power-law model for stress-dependent β-values with ζ=0 (M_5,

ets0.ipc3), exhibits the same systematic tendency for over-prediction of both maximum magnitudes and total seismic moments albeit to a lesser extent and without exceeding the 95% confidence interval. The absolute mean maximum magnitude bias ($\Delta M_{\max} = 0.4$) is still significant relative to the magnitude measurement errors. In contrast, the exponential stress-dependent ζ-model with $\beta = 2/3$ (M_{11}, ets0.ltc3) exhibits no bias in either maximum magnitudes or total seismic moments and does not exceed the 95% prediction interval despite this interval being significantly smaller than the previous two models. Moreover, the observed variability approaches both the upper and lower bounds of the simulated variability. As such this model demonstrates zero bias and a simulated variability consistent with the observed variability.

Figure 27 shows the distributions of out-of-sample likelihood, $L_s(\mathbf{D}_{2t}|\mathbf{\Theta}_i)$, for observed maximum magnitudes, $\mathbf{D}_{\max,2}$, given the simulated maximum magnitude time series. We obtained the maximum magnitudes data set, $\mathbf{D}_{\max}$ by selecting the subset of events within the complete data set, $\mathbf{D}$, that are larger than all previous events. This data set is then partitioned according to event origin times to yield the out-of-sample maximum magnitudes data set $\mathbf{D}_{\max,2}$.

We estimate the out-of-sample likelihoods, L_s, using the distribution of simulated maximum magnitude time series according to the posterior model distribution, $P(\mathbf{\Theta}_i|\mathbf{D}_1)$. We performed these simulations in a nested manner to yield simulated maximum magnitude time series, $\mathcal{S}_{ijk}$, where i denotes the model, j denotes a single random sample from the posterior distribution, $P(\mathbf{\Theta}_i|\mathbf{D}_1)$, and k denotes the simulation index. In this manner, time series $\mathcal{S}_{ijk}$ represents the k^{th} simulation of the j^{th} posterior sample from the i^{th} model.

For each i and j, and observed event within $\mathbf{D}_{\max,2}$, we select the set of simulated maximum magnitudes at the observed origin times. Using a Gaussian kernel density estimate for the probability density function of these simulated maximum magnitudes, we compute the likelihood of this observed maximum magnitude. Repeating this for all $\mathbf{D}_{\max,2}$ events L_s is estimated as the product of these single-event likelihood values. Repeating this for all values of j yields the posterior distribution of likelihood value for model M_i. Repeating all of these steps for all values of i results in the collection of likelihood distributions shown by Figure 27. Better performing models appear with likelihood distributions located to the right of poorer performing models. However, as all these distributions overlap with different tail shapes the relative performance ranking is not completely clear. Nonetheless it is clear the top two models are both include stress-dependent ζ-values.

As these distributions substantially overlap, we summarize the overall relative performance according to the probability of one model yielding a better

out-of-sample likelihood than another model, P_{ij}, according to (34). Table 3 shows the pairwise probabilities P_{ij} that model M_i out-performs model M_j given their respective out-of-sample maximum magnitude likelihood distributions. If the models are listed in rank order of performance then this matrix, P_{ij} would show monotonically increasing values as i increases (moving top to bottom in each column of Table 3) and as j decreases (moving right to left in each row of Table 3). In this case, the results are less clear

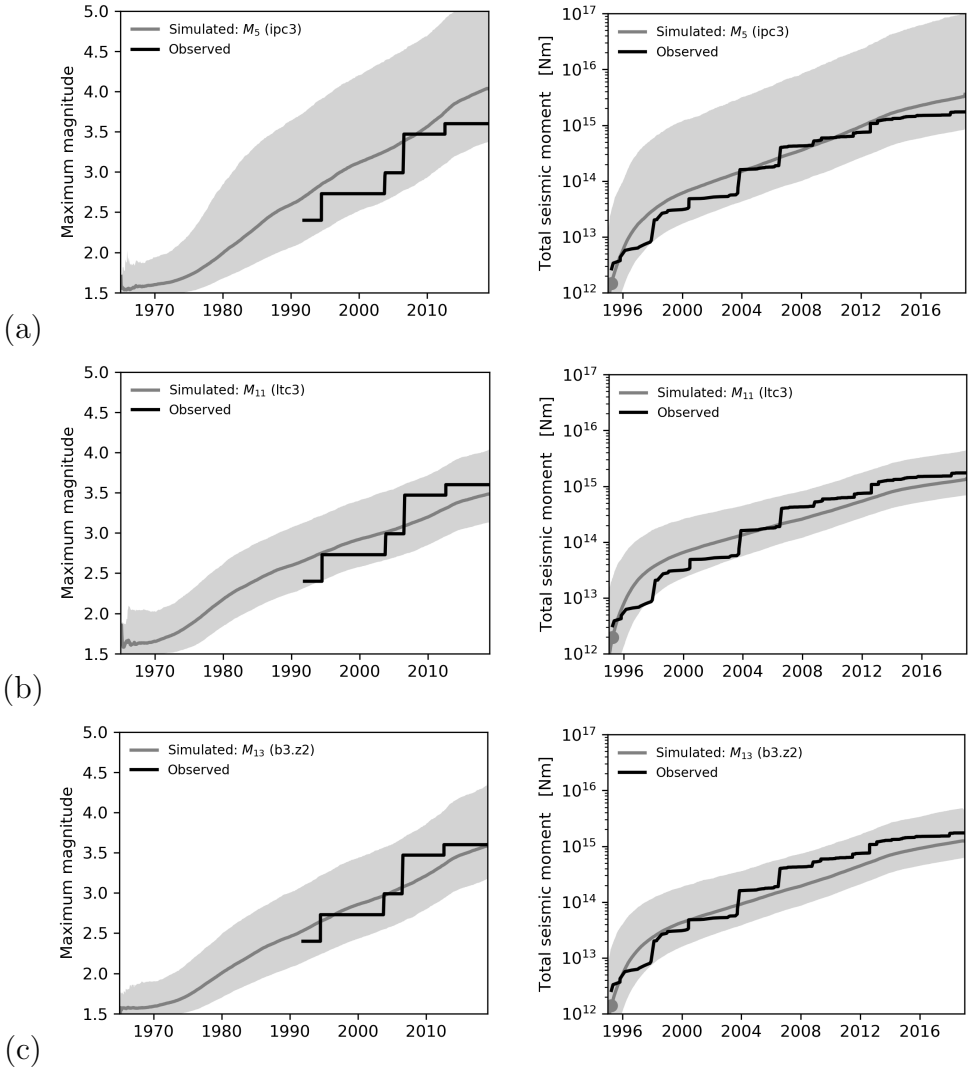

Figure 25: As Figure 24, except for three stress-dependent magnitude-frequency models: (a) stress-dependent β-values, M_5, (b) stress-dependent ζ-values, M_{11}, and (c) stress-dependent β-ζ-values, M_{13}.

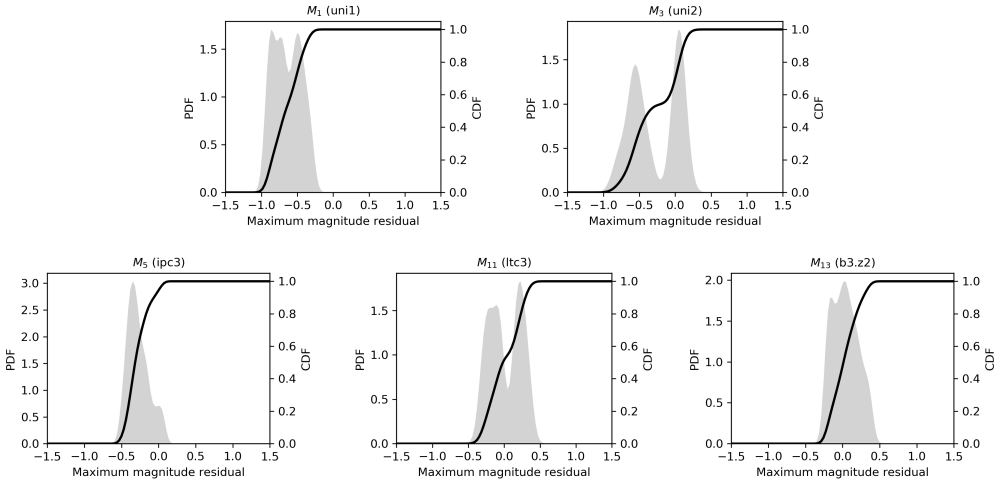

Figure 26: The distribution of all residuals between the observed and simulated time series of maximum magnitudes.

in the sense that no such complete and unambiguous ranking exists. This is because the relative performance of several middle-ranking models are so similar, likely due to the small out-of-sample size available. Nonetheless, we may still confidently identify the best-performing models.

The baseline model (M_1) is out-performed by all other models, although none exceed 95% probability, although two models (M_{11}, M_{13}) are close with a 94% chance of exceeding the baseline performance. The only common feature of these two models is a stress-dependent ζ variation. One stress-dependent β model (M_7) does indicate a 91% chance of exceeding the baseline performance, but its chances of out-performing the leading two models are just 25% and 19% respectively. Ranking all models by increasing performance based on this metric yields $\{M_1, M_2, M_3, M_5, M_{10}, M_7, M_{11}, M_{13}\}$. This is essentially the numerical model sequence shown in Table 3 except the best-performing stress-dependent β-model, M_7, exchanges places with the worst performing stress-dependent ζ-model, M_{10}. We attribute this to a poor parametrization choice for M_{10} resulting in a large trade-off between the θ_2 and θ_3 parameters shown in Figure 16 associate with insufficient information to constrain the location of the critical point, θ_3.

As previously discussed in section 10, a key diagnostic is the time series of counts for events that exceed a given magnitude threshold (see Figure 21), especially the early time evolution. To revisit this, we compute the mean simulated cumulative event count time series over a range of magnitude exceedance thresholds. Figure 28 compares these simulated time series with

the observed events from 1995 to 2019. The simulated $M \geq 1.5$ cumulative counts are identical for all models as this depends on the activity rate model alone which is shared by all magnitude-frequency models. For larger magnitude exceedance thresholds, the simulated time series differ between the different magnitude-frequency models.

For the stress-invariant β-model with ζ=0 (M_1, Figure 28a), the simulated count time series is systematically over-predicted for magnitudes $M \geq 2.5$ during their early time evolution. This error increases with magnitude threshold, such that the simulated $M \geq 4$ counts are comparable to the observed

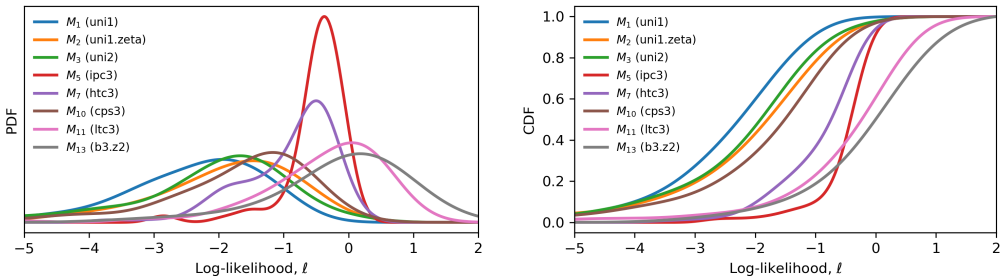

Figure 27: Out-of-sample forecast performance for the maximum magnitude time series. Training period 1995 to 2012. Simulation period 1965 to 2019. Evaluation period before 1995 and after 2012.

Model class		M_i	P_{ij}, Probability of M_i out-performing M_j							
Stress invariant	uni1	M_1	0.500	0.400	0.370	0.283	0.091	0.343	0.060	0.060
	uni1.zeta	M_2	0.600	0.500	0.580	0.374	0.192	0.424	0.110	0.080
	uni2.zeta	M_3	0.630	0.420	0.500	0.364	0.162	0.394	0.110	0.120
Stress-dependent β	ets0.ipc3	M_5	0.717	0.626	0.636	0.500	0.273	0.576	0.152	0.111
	ets0.htc3	M_7	0.909	0.808	0.838	0.727	0.500	0.727	0.253	0.192
Stress-dependent ζ	ets0.cps3	M_{10}	0.657	0.576	0.606	0.424	0.273	0.500	0.141	0.121
	ets0.ltc3	M_{11}	0.940	0.890	0.890	0.848	0.747	0.859	0.500	0.400
Stress-dependent β-ζ	ets0.b3.z2	M_{13}	0.940	0.920	0.880	0.889	0.808	0.879	0.600	0.500
			M_1	M_2	M_3	M_5	M_7	M_{10}	M_{11}	M_{13}
			M_j							

Table 3: Relative pairwise model forecast performance for the observed out-of-sample maximum magnitude time series as measured by the probability, P_{ij}, of model M_i out-performing model M_j. Colours vary from red to yellow to green denoting probabilities from 0 to 0.5 to 1 respectively. By definition, $P_{ij} + P_{ji} = 1$, so the above diagonal cells contain the same information as their below diagonal counterparts.

$M \geq 3.5$ counts. A similar bias is also apparent in the stress-dependent β model (Figure 29a), although in this case over-prediction is only apparent for magnitudes $M \geq 3.0$. The stress-invariant beta-zeta model (M_3, Figure 28b) improves the fit for larger magnitudes ($M > 3$) at the end of the time period but also over-predicts for magnitudes $M \geq 2.5$ during their early time evolution.

The stress-dependent β model (M_{11}, Figure 29a) slightly improves the early time prediction of $M \leq 2.5$ events relative to the stress-invariant models, but systematically over-predicts events counts for $M \geq 3.5$ events. The stress-dependent ζ model (M_{11}, Figure 29b) shows the best match to the observed rates with no apparent bias for any of the observed magnitude thresholds especially at later times when the fractional count errors are smallest. The higher dimensional, hybrid model with stress-dependent β- and ζ-values (M_{13}, Figure 29c) clearly under-predicts the numbers of $M \geq 2.5$ and $M \geq 3$ events. This result would be counter-intuitive if model performance was evaluated on the same data used for model inference. In this case, the extra degrees of freedom should give a better fit. However, we evaluate the model on data not previously used for model inference. This means any over-fitting

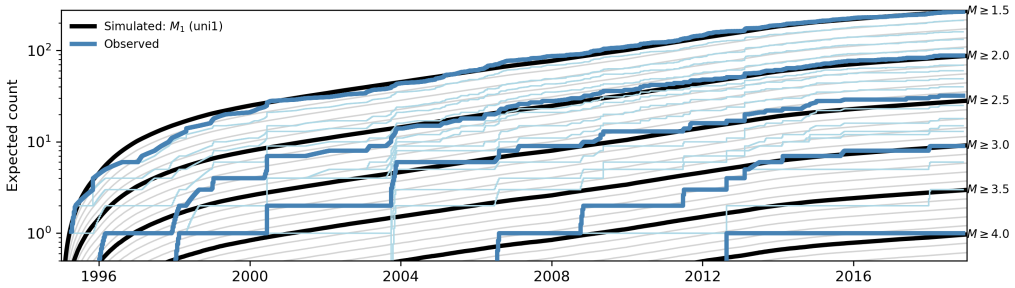

(a)

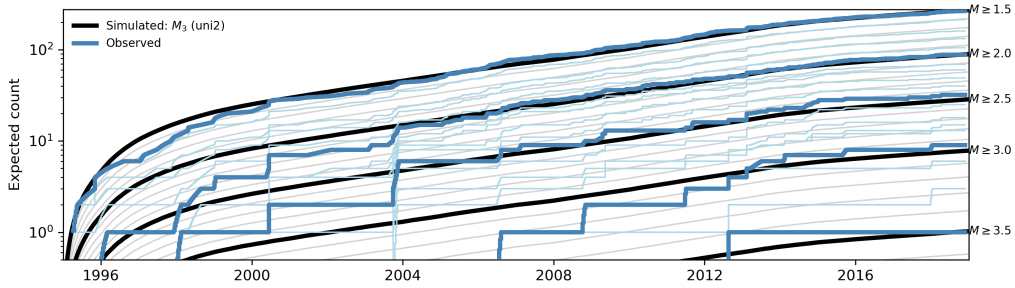

(b)

Figure 28: Observed event count time series compared to expected event counts obtained by model simulations from 1995 to 2019 for (a) stress-invariant β-values,M_1, and (b) stress-invariant β-ζ-values, M_3. See Table 1 for model details.

associated with too many degrees of freedom will likely appear as bias in this out-of-sample evaluation.

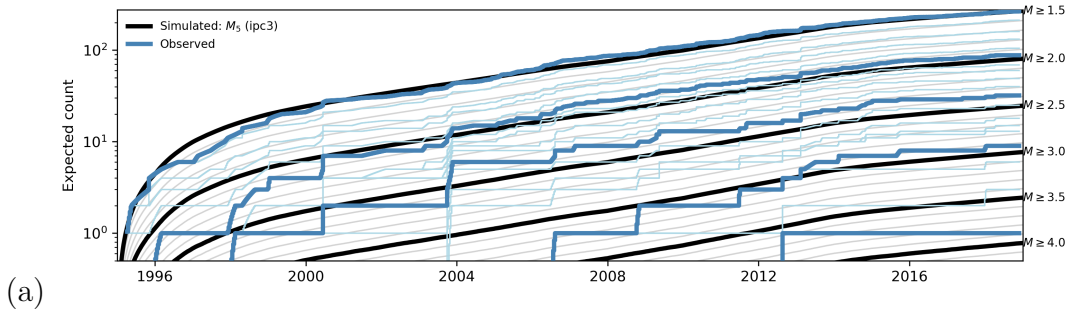

(a)

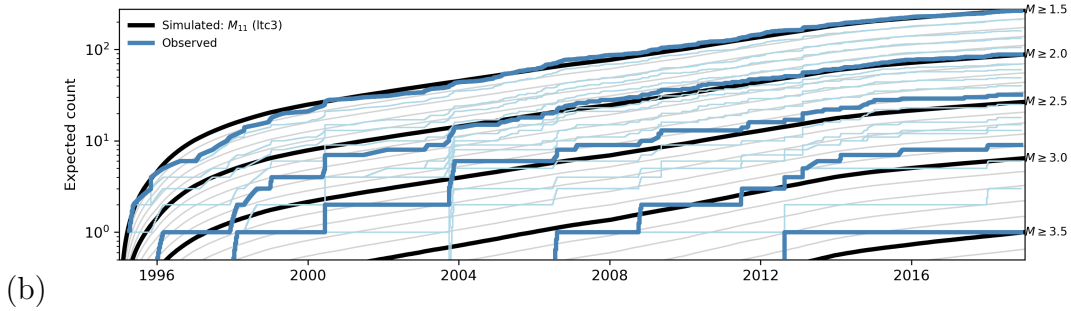

(b)

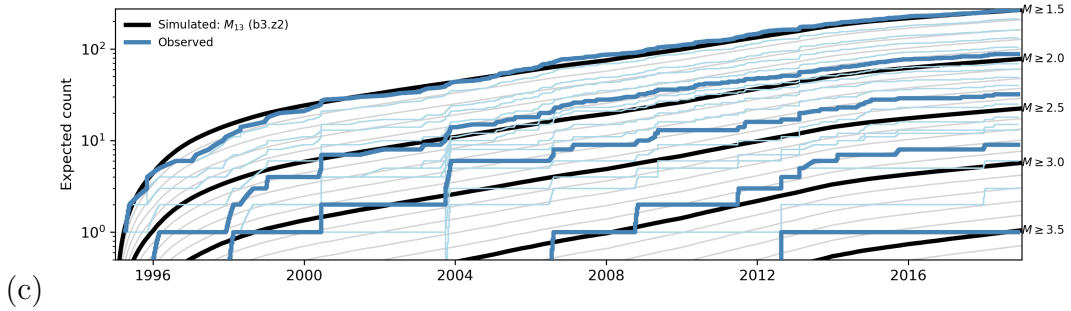

(c)

Figure 29: As Figure 28, except for (a) stress-dependent β-values, M_7, (b) stress dependent ζ-values, M_{11}, and (c) stress-dependent β- and ζ-values, M_{13}. See Table 1 for model details.

12 Discussion

12.1 Probabilities of larger magnitudes

Central to the analysis of seismic hazard and risk induced by Groningen gas production is the reliable forecasting of larger than previously experienced magnitudes. Probabilistic analyses for Groningen show magnitudes in the range 4.5–5.5 provide the largest contribution to seismic hazard and risk metrics associated with public safety within the built environment (Bourne et al., 2015; Elk et al., 2019). Smaller magnitudes are always too small to influence the hazard and risk metrics, whilst larger magnitudes are too infrequent to influence the hazard and risk metrics.

Using the gas production history and a single future gas production scenario (2019 GTS Raming) we simulated earthquakes catalogues for the entire history of gas production (1965–2019), and the next 5 years of future gas production (2019–2024). Earthquake occurrence was simulated used the posterior distribution of Extreme Threshold Failure models (Bourne and Oates,

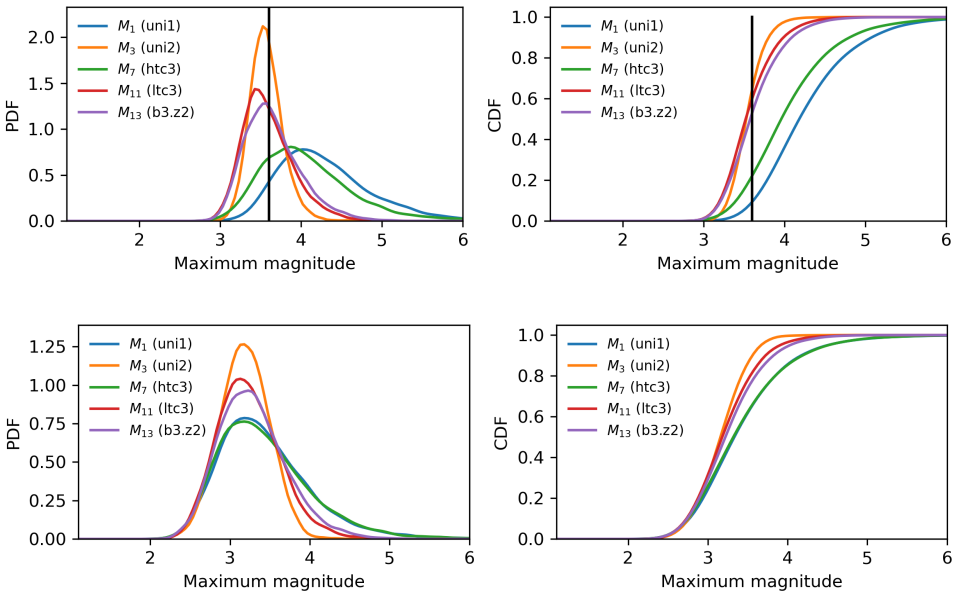

Figure 30: The distribution of maximum magnitudes according to model simulations for the periods (a) 1965–2019, and (b) 2019–2024. The vertical black line denotes the observed $M = 3.6$ maximum magnitude. The expected maximum magnitudes are 4.3, 3.6, 4.1, 3.6, 3.7 for the M_1, M_2, M_7, M_{11}, and M_{13} models respectively.

2017) inferred using the 1995–2019 $M \geq 1.5$ events and a poro-elastic thin-sheet Coulomb stress model (section 5). Earthquake magnitudes were simulated using the $M_1, M_3, M_7, M_{11}, M_{13}$ magnitude-frequency models in turn.

Figure 30 shows the distribution of maximum simulated magnitudes associated with the first 54 years (1965–2019) and the next 5 years (2019–2024) according to the different magnitude-frequency models. Over the observed period (1965–2019) the exponentially-tapered ζ-models (M_3, M_{11}, M_{13}) most closely match the observed maximum magnitude, $M = 3.6$. Models that lack such a taper (M_1, M_7) over-predicted this magnitude 80–90% of the time with a mean over-prediction bias of 0.5–0.7 in magnitude. Maximum magnitudes are an important model performance metric as they typically form part of traffic light systems used to trigger interventions as is the case for Groningen induced seismicity.

Simulation-based forecasts for the next 5 years yield different distributions for the maximum magnitude event all with the same mode $M = 3.2$ and similar medians (Table 4, 50%, M=3.2–3.5). However, hazard and risk are driven by larger, less-likely magnitudes in the upper tail of these distributions and differences between these upper tails are considerable. Table 4 shows models with an exponential taper ($M_2, M_3, M_{10}, M_{11}, M_{13}$) exhibit much lower magnitudes with a 1% chance of exceeding (3.9–4.5) than the other models (M_1, M_5, M_7, M_{11}) that lack an exponential taper (5.3–5.5). This is a difference of 0.8–1.6 in magnitude.

Forecasts over longer periods necessarily face increasing uncertainties associated with larger extrapolations of the pore-pressure depletion model given the observed depletion history, and also larger extrapolations of the seismological model given the observed seismicity history. Limiting forecast periods to 5 years or less limits our exposure to extrapolation related uncertainties.

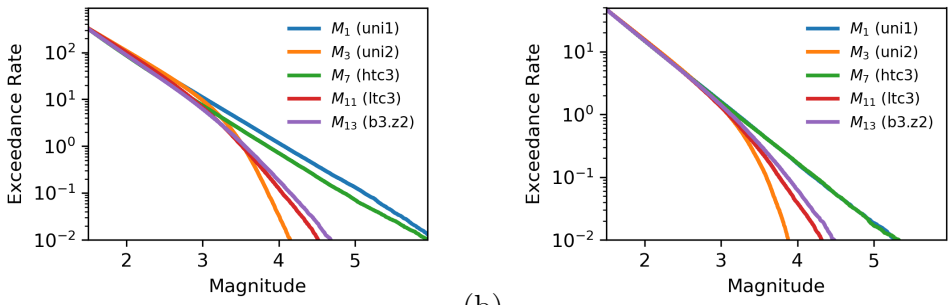

Figure 31: Magnitude exceedance rate according to model simulations over the periods (a) 1965 to 2019, (b) 2019 to 2024.

Model	50%	10%	1%
M_1 (uni1)	3.36	4.18	5.29
M_2 (uni1.zeta)	3.16	3.58	3.95
M_3 (uni2)	3.18	3.58	3.88
M_5 (ipc3)	3.33	4.25	5.48
M_7 (htc3)	3.34	4.21	5.32
M_{10} (cps3)	3.29	3.81	4.45
M_{11} (ltc3)	3.20	3.74	4.32
M_{13} (b3.z2)	3.24	3.84	4.47

Table 4: Comparison of the magnitudes with a 50%, 10%, and 1% chance over exceedance between 2019 and 2024 according to simulations of the different magnitude-frequency models without imposing an upper bound, $M_{\max}$, to these probability distributions. These results are based on the *2019 GTS Raming* production scenario.

12.2 Including an upper bound

The magnitudes models, as formulated so far, do not include an upper bound, corresponding to a maximum possible magnitude, $M_{\max}$. For any finite system there must be a finite limit on the magnitude of earthquakes within that system. This quantity is not directly observable within the Groningen earthquake catalogue, but we are still able to incorporate a prior distribution for $M_{\max}$ within the magnitude-frequency models. Following Cornell and Van Marke (1969), the survival function of a magnitude distribution may be truncated to reflect some prior belief in a maximum possible seismic moment, $\mathcal{M}_{\max}$, providing an upper bound to the distribution, according to

$$P(\geq \mathcal{M}|\mathcal{M}_m \leq \mathcal{M} \leq \mathcal{M}_{\max}) = \frac{P(\mathcal{M}) - P(\mathcal{M}_{\max})}{1 - P(\mathcal{M}_{\max})} \tag{35}$$

where the un-truncated survival function $P(\mathcal{M})$ is given by (11). In the case of Groningen induced seismicity, van Elk et al. (2017) reported a collective expert-judgement based prior discrete distribution of maximum possible magnitudes with a 3.75–7.25 range and a 4.8 median and 5.0 mean. For the most-part, the influence of the posterior distribution of exponential tapers occurs at significantly lower magnitudes than this prior distribution of $M_{\max}$.

For the data analysed in this study, incorporating stress-dependent exponential tapering of the power-law seismic moment distribution alongside an upper bound in earthquake magnitude-frequency models used for probabilistic hazard and risk analysis of induced seismicity within the Groningen gas field reduces bias that may otherwise in this case over-state the hazard

and risk. Utilizing data-driven, stress-dependent ζ-models also reduces the impact of imposing a maximum magnitude based on an expert judgement. This procedure is therefore more robust to possibility of expert bias.

13 Conclusions

In summary, the stress-dependent ζ-model with constant β (M_{10}, M_{11}) offer higher performance magnitude-frequency forecasts than the stress-dependent β-models with $\zeta = 0$ (M_5, M_7) 75–85% of the time (Table 3) and lower the magnitude with a 10% and 1% chance of exceedance from 4.3 to 3.8 and from 5.5 to 4.5 respectively. Likewise, stress-dependent ζ-models outperform stress-invariant ζ-models (M_2, M_3) about 90% of the time, although in this case the stress-dependence of ζ increases the magnitude with 1% chance of exceedance from 3.9 to 4.4–4.5. The hybrid model with stress-dependent β and ζ values, M_{13}, includes all these possibilities in one joint posterior distribution, resulting in a 1% magnitude of 4.6, which is much closer to the stress-dependent ζ models than any of the other frequency-magnitude distributions (Figure 31).

There are two possibilities for incorporating these alternative magnitude-frequency models into a probabilistic seismic hazard and risk analysis.

1. Treat these model selection uncertainties as aleatory and rely on the M_{13} model alone to represent all possible models within the Monte Carlo simulations of induced seismicity, hazard and risk.

2. Treat model selection as an epistemic uncertainty and include each independent model class as different branches on a logic tree of alternative Monte Carlo simulations. To do this, we may use the evidence-based weight factors given by Table 3. So for the mutually independent and collectively exhaustive model set $\{M_1, M_2, M_7, M_{11}\}$ would be represented by the logic tree branch weights $\{0.04, 0.08, 0.18, 0.7\}$. Given, the small weights attached to the first two models, and the need to limit the computational cost of probabilistic seismic hazard and risk assessments we recommend truncating this to the top two models $\{M_7, M_{11}\}$ with weights $\{0.2, 0.8\}$.

We recommend the second option, as it explicitly includes both the current seismological model used for hazard and risk analysis (M_7) and the new model (M_{11}) with its likely improved performance. Including both on the logic tree would allow the influence of each model on hazard and risk to be independently assessed. The new stress-dependent exponential-taper

power-law model introduced here likely offers better forecast performance and better represents the physical processes of failure size distributions within a heterogeneous material under increasing stress. The limited sample size of Groningen earthquakes means we cannot be definitive in our preference for a single frequency-magnitude model. Instead, we represent our currently limited knowledge using a range of different models weighted by their measured performance evidence rather than expert judgement. Over time, further earthquake observations within Groningen, other analogue fields, or laboratory experiments may be decisive.

Acknowledgements

We gratefully acknowledge our colleagues from Nederlandse Aardolie Maatschappij, Rob van Eijs, Onno van der Wal, Jan van Elk, Dirk Doornhof, Assaf Mar-Or, and from Shell Global Solutions International, Stijn Bierman, Phil Jonathan for their ongoing support during this study. The implementation of these seismological models made use of SciPy (Jones et al., 2001) and PyMC3 (Salvatier et al., 2015) and most of the figures were created using Matplotlib (Hunter, 2007).

References

Aki, K., 1965. Maximum likelihood estimation of b in the formula logN=a-bM and its confidence limits. Bulletin of the Earthquake Research Institute of Tokyo University 43, 237–239.

Alava, M.J., Nukala, P.K.V.V., Zapperi, S., 2006. Statistical models of fracture. Advances in Physics 55, 349–476.

Amitrano, D., 2012. Variability in the power-law distributions of rupture events. The European Physical Journal Special Topics 205, 199–215.

Amorèse, D., Grasso, J.R., Rydelek, P.A., 2010. On varying b-values with depth: Results from computer-intensive tests for Southern California. Geophysical Journal International 180, 347–360.

de Arcangelis, L., Godano, C., Grasso, J.R., Lippiello, E., 2016. Statistical physics approach to earthquake occurrence and forecasting. Physics Reports 628, 1–91.

de Arcangelis, L., Redner, S., Herrmann, H., 2007. A random fuse model for breaking processes. Journal de Physique Lettres 46, 585–590.

Bachmann, C.E., Wiemer, S., Goertz-Allmann, B.P., Woessner, J., 2012. Influence of pore-pressure on the event-size distribution of induced earthquakes. Geophysical Research Letters 39.

Bak, P., Tang, C., 1989. Earthquakes as a Self-Organized Critical Phenomenon. Journal of Geophysical Research 94, 15635–15637.

Bender, B., 1983. Maximum likelihood estimation of b values grouped data. Bulletin of the Selsmologmal Socmty of America 73, 831–851.

Bonamy, D., Bouchaud, E., 2011. Failure of heterogeneous materials: A dynamic phase transition? Physics Reports 498, 1–44.

Bourne, S.J., Oates, S.J., 2017. Extreme threshold failures within a heterogeneous elastic thin-sheet and the spatial-temporal development of induced seismicity within the Groningen gas field. Journal of Geophysical Research: Solid Earth 122, 10,299–10,320.

Bourne, S.J., Oates, S.J., Bommer, J.J., Dost, B., Elk, J.V., Doornhof, D., 2015. A Monte Carlo Method for Probabilistic Hazard Assessment of Induced Seismicity due to Conventional Natural Gas Production. Bull. Seis. Soc. Am. 105.

Bourne, S.J., Oates, S.J., van Elk, J., Doornhof, D., 2014. A seismological model for earthquakes induced by fluid extraction from a subsurface reservoir. Journal of Geophysical Research: Solid Earth 119, 8991–9015.

Bourne, S.J., Oates, S.J., Elk, J.V., 2018. The exponential rise of induced seismicity with increasing stress levels in the Groningen gas field and its implications for controlling seismic risk. Geophysical Journal International 213, 1693–1700.

Burridge, R., Knopoff, L., 1967. Model and theoretical seismicity. Bulletin of the Seismological Society of America 57, 341–371.

Coniglio, A., Klein, W., 1980. Clusters and Ising critical droplets: A renormalisation group approach. Journal of Physics A: Mathematical and General 13, 2775–2780.

Cornell, C.A., Van Marke, E.H., 1969. The major influences on seismic risk, in: Proc. 4th World Conf. on Earthquake Engineering, Santiago, Chile, pp. A–1, 69–93.

Daguier, P., Nghiem, B., Bouchaud, E., Creuzet, F., 1997. Pinning and Depinning of Crack Fronts in Heterogeneous Materials. Phys. Rev. Lett. 78.

Davies, R., Foulger, G., Binley, A., Styles, P., 2013. Induced seismicity and hydraulic fracturing for the recovery of hydrocarbons. Marine and Petroleum Geology 45, 171–185.

Dost, B., Goutbeek, F., Eck, T.V., Kraaijpoel, D., 2012. Monitoring induced seismicity in the North of the Netherlands: status report 2010. Technical Report. Koninklijk Nederlands Meteorologisch. de Bilt, The Netherlands.

Dublanchet, P., Bernard, P., Favreau, P., 2013. Interactions and triggering in a 3-D rate-and-state asperity model. Journal of Geophysical Research: Solid Earth 118, 2225–2245.

van Elk, J., Mar-Or, A., Doornhof, D., 2017. Assessment of Building Damage based on Production Scenario Basispad Kabinet for the Groningen field: Addendum to "Induced Seismicity in Groningen Assessment of Hazard, Building Damage and Risk". Technical Report November. Nederlandse Aardolie Maatschappij B.V.. Assen, The Netherlands.

Elk, J.V., Bourne, S.J., Oates, S.J., Bommer, J.J., 2019. A Probabilistic Seismic Risk Model to Inform Decision-Making in Response to Induced

Earthquakes in the Groningen Gas Field. Earthquake Spectra 35, 537–564.

Ellsworth, W., 2013. Injection-induced earthquakes. Science 341, 250–260.

Evans, K., Zappone, A., Kraft, T., Deichmann, N., Moia, F., 2012. A survey of the induced seismic responses to fluid injection in geothermal and CO2 reservoirs in Europe. Geothermics 41, 30–54.

Foulger, G.R., Wilson, M.P., Gluyas, J.G., Julian, B.R., Davies, R.J., 2018. Global review of human-induced earthquakes. Earth-Science Reviews 178, 438–514.

Frohlich, C., Davis, S., 1993. Teleseismic b Values; Or, Much Ado About 1.0. Journal of Geophysical Research 98, 631–644.

Gilabert, A., Vanneste, C., Sornette, D., Guyon, E., 2007. The random fuse network as a model of rupture in a disordered medium. Journal de Physique 48, 763–770.

Gould, H., Tobochnik, J., 2010. Statistical and Thermal Physics with Computer Applications. Princeton University Press, New Jersey.

Gulia, L., Wiemer, S., 2010. The influence of tectonic regimes on the earthquake size distribution: A case study for Italy. Geophysical Research Letters 37, n/a–n/a.

Gutenberg, B., Richter, C., 1954. Seismicity of the Earth and Associated Phenomena. Princeton University Press, Princeton, New Jersey. 2nd edition.

Hansen, A., 2011. Random Fuse Networks: A Review. Physical Aspects of Fracture , 59–72.

Hansen, A., Hemmer, P.C., 1994. Burst avalanches in bundles of fibers: Local versus global load-sharing. Physics Letters A 184, 394–396.

Harris, C., Bourne, S.J., 2019. Fiber Failure Avalanches in Fiber Bundle Models with Global Load Sharing Extension to New Fiber Threshold Strength Distributions Exhibiting Anomalous Behavior. Physical Review E Publication (submitted) .

Harris, C.K., Bourne, S.J., 2017. Computing the Distribution of Pareto Sums using Laplace Transformation and Stehfest Inversion. Pure and Applied Geophysics .

Hemmer, C., Hansen, A., 1992. The distribution of simultaneous fiber failures in fiber bundles. J. Applied Mechanics 92, 909–914.

Huang, H.H., Huang, T.C., Wu, Y.M., Koulakov, I., Chen, S.K., Chao, W.A., 2018. Relationship Between Earthquake b -Values and Crustal Stresses in a Young Orogenic Belt. Geophysical Research Letters 45, 1832–1837.

Hunter, J.D., 2007. Matplotlib: A 2D graphics environment. Computing In Science & Engineering 9, 90–95.

IEAGHG, 2013. INDUCED SEISMICITY AND ITS IMPLICATIONS FOR CO2 STORAGE RISK. Technical Report June. International Energy AgencyEnvironmental Projects Ltd. (IEAGHG). Cheltenham, UK.

Jiang, X., Liu, H., Main, I.G., Salje, E.K., 2017. Predicting mining collapse: Superjerks and the appearance of record-breaking events in coal as collapse precursors. Physical Review E 96, 1–7.

Jones, E., Oliphant, T., Peterson, P., 2001. SciPy: Open source scientific tools for Python. http://www.scipy.org/.

J.P. Sethna, K.A. Dahmen, C.R. Myers, 2001. Crackling noise: Preprint. Nature 410, 242–250.

Kac, M., 1968. Mathematical Mechanisms of Phase Transitions, in: Chretilin, M., Gross, E., Dresser, S. (Eds.), Statistical Mechanics of Phase Transitions and Superfluidity. Gordon and Breach Science Publishers, New York.

Kagan, Y.Y., 1999. Universality of the seismic moment-frequency relation. Pure and Applied Geophysics 155, 537–573.

Kagan, Y.Y., 2002a. Seismic moment distribution revisited : II. Moment conservation principle. Geophys. J. Int 149, 731–754.

Kagan, Y.Y., 2002b. Seismic moment distribution revisited: I. Statistical results. Geophysical Journal International 148, 520–541.

Kagan, Y.Y., 2010. Earthquake size distribution: Power-law with exponent $\beta 1/2$? Tectonophysics 490, 103–114.

Kamer, Y., Hiemer, S., 2015. Data-driven spatial b value estimation with applications to California seismicity: To b or not to b. J. Geophys. Res. Solid Earth 120,, 5191–5214,.

King, G., 1983. The accommodation of large strains in the upper lithosphere of the earth and other solids by self-similar fault systems: the geometrical origin of b-Value. Pure and Applied Geophysics PAGEOPH 121, 761–815.

Klose, C.D., 2013. Mechanical and statistical evidence of the causality of human-made mass shifts on the Earth's upper crust and the occurrence of earthquakes. Journal of Seismology , 109–135.

Kloster, M., Hansen, A., Hemmer, P.C., 1997. Burst avalanches in solvable models of fibrous materials. Physical Review E - Statistical Physics, Plasmas, Fluids, and Related Interdisciplinary Topics 56, 2615–2625.

Langenbruch, C., Zoback, M.D., 2016. How will induced seismicity in Oklahoma respond to decreased saltwater injection rates? Science Advances 2, 1–9.

Luther, S., Mertens, S., 2011. Counting lattice animals in high dimensions. Journal of Statistical Mechanics: Theory and Experiment 2011. `arXiv:1106.1078v2`.

Main, I., Sammonds, P., Meredith P.R., Jones, C., 1990. Influence of fractal flaw distributions on rock deformation in the brittle field, in: Knipe, R. J. & Rutter, E.H. (Ed.), Deformation Mechanisms, Rheology and Tectonics,. Geological Society Special Publication No. 54, pp. 71–79.

Main, I.G., 1995. Earthquakes as Critical Phenomena: Implications for Probabilistic Seismic Hazard Analysis 85, 1299–1308.

Main, I.G., 1996. Statistical Physics, Seismogenesis and Seismic Hazard. Reviews of Geophysics , 433–462.

Main, I.G., Burton, P.W., 1984. Information theory and the earthquake frequency-magnitude distribution. Bulletin of the Seismological Society of America 74, 1409–1426.

Main, I.G., Meredith, P.G., Jones, C., 1989. A reinterpretation of the precursory seismic bvalue anomaly from fracture mechanics. Geophysical Journal International 96, 131–138.

Main, I.G., Meredith, P.G., Sammonds, P.R., 1992. Temporal variations in seismic event rate and b-values from stress corrosion constitutive laws. Tectonophysics 211, 233–246.

Majer, E., Baria, R., Stark, M., Oates, S., Bommer, J., Asanuma, H., 2007. Induced seismicity associated with enhanced geothermal systems. Geothermics 36, 185–222.

Mogi, K., 1962. Magnitude frequency relation for elastic shocks accompanying fractures of various materials and some related problems in earthquakes. Bull. Earthquake Res. Inst. Tokyo Univ. 40, 831–853.

Mori, J., Abercrombie, R., 1997. Depth dependence of earthquake frequency-magnitude distributions in California: Implications for rupture initiation. Journal of Geophysical Research 102, 15,081–15,090.

NAS, 2013. Induced seismicity potential in energy technologies. National Academy of Sciences, Washington, DC, USA.

Nukala, P.K.V., Zapperi, S., Åimunović, S., 2005. Statistical properties of fracture in a random spring model. Physical Review E - Statistical, Nonlinear, and Soft Matter Physics 71, 1–11.

Petersen, M.D., Mueller, C.S., Moschetti, M.P., Hoover, S.M., Rukstales, K.S., McNamara, D.E., Williams, R.A., Shumway, A.M., Powers, P.M., Earle, P.S., Llenos, A.L., Michael, A.J., Rubinstein, J.L., Norbeck, J.H., Cochran, E.S., 2018. 2018 one-year seismic hazard forecast for the central and eastern United States from induced and natural earthquakes. Seismological Research Letters 89, 1049–1061.

Ponson, L., Bonamy, D., Bouchaud, E., 2006. Two-Dimensional Scaling Properties of Experimental Fracture Surfaces. Phys. Rev. Lett. 96, 035506.

Pradhan, S., 2010. Failure Processes in Elastic Fiber Bundles. Rev. Mod. Phys. 82, 449–. arXiv:0808.1375v3.

Roberts, N.S., Bell, A.F., Main, I.G., 2016. Mode switching in volcanic seismicity: El Hierro 2011-2013. Geophysical Research Letters 43, 4288–4296.

Roux, S., Hansen, A., Herrmann, H., Guyon, E., 1988. Rupture of heterogeneous media in the limit of infinite disorder. Journal of Statistical Physics 52, 237–244.

Salvatier, J., Wiecki, T., Fonnesbeck, C., 2015. Probabilistic Programming in Python using PyMC , 1–241507.08050.

Scholz, C., 1968. Microfractures, Aftershocks, and Seismicity. Bulletin of the Seismological Society of America 58, 1117–1130.

Schorlemmer, D., Wiemer, S., Wyss, M., 2005. Variations in earthquake-size distribution across different stress regimes. Nature 437, 539–542.

Shapiro, S., Dinske, C., Langenbruch, C., 2010a. Seismogenic index and magnitude probability of earthquakes. The Leading Edge March.

Shapiro, S., Dinske, C., Langenbruch, C., 2010b. Seismogenic index and magnitude probability of earthquakes induced during reservoir fluid stimulations. The Leading Edge .

Shapiro, S.A., 2018. Seismogenic Index of Underground Fluid Injections and Productions. Journal of Geophysical Research: Solid Earth 123, 7983–7997.

Shekhawat, A., Zapperi, S., Sethna, J.P., 2013. From damage percolation to crack nucleation through finite size criticality. Physical Review Letters 110, 1–5.

Shi, Y., Bolt, B.A., 1982. The standard error of the magnitude-frequency b-value. Bulletin of the Seismological Society of America 72, 1677–1687.

Sornette, D., Physique, J.D., 1992. Mean-field solution of a block-spring model of earthquakes. Journal de Physique I, EDP Sciences 11, 2089–2096.

Spada, M., Tormann, T., Wiemer, S., Enescu, B., 2013. Generic dependence of the frequency-size distribution of earthquakes on depth and its relation to the strength profile of the crust. Geophysical Research Letters 40, 709–714.

Stauble, A., Milius, G., 1970. Geology of Groningen Gas Field, Netherlands, in: Halbouty, M. (Ed.), Geology of giant petroleum fields. American Association of Petroleum Geologists, Tulsa, Memoir 14 edition. pp. 359–369.

Stauffer, D., Aharony, A., 1992. Introduction To Percolation Theory. Taylor & Francis. second edition.

Stauffer, D., Aharony, A., 1994. Introduction To Percolation Theory. Taylor & Francis, London. second edition.

Suckale, J., 2009. Induced Seismicity in Hydrocarbon Fields. Advances in Geophysics 51, 55–106.

Tinti, S., Mulargia, F., 1987. Confidence intervals of b values for grouped magnitudes. Bull. Seismol. Soc. Am. 77, 2125–2134.

Tormann, T., Wiemer, S., Mignan, A., 2014. Journal of Geophysical Research : Solid Earth Systematic survey of high-resolution b value imaging along Californian faults : Inference on asperities. Journal of Geophysical Research: Solid Earth 119, 2029–2054.

Toussaint, R., Hansen, A., 2006. Mean-field theory of localization in a fuse model. Physical Review E - Statistical, Nonlinear, and Soft Matter Physics 73.

Toussaint, R., Pride, S.R., 2005. Interacting damage models mapped onto Ising and percolation models. Physical Review E - Statistical, Nonlinear, and Soft Matter Physics 71.

Turcotte, D., 1997. Fractals and Chaos in Geology and Geophysics. Cambridge University Press, Cambridge, United Kingdom. second edition.

Utsu, T., 1965. A method for determining the value of b in a formula log n = a - bM showing the magnitude-frequency relation for earthquakes. Geophys. Bull. Hokkaido Univ. 13, 103.

Vasseur, J., Wadsworth, F.B., Heap, M.J., Main, I.G., Lavallée, Y., Dingwell, D.B., 2017. Does an inter-flaw length control the accuracy of rupture forecasting in geological materials? Earth and Planetary Science Letters 475, 181–189.

Vasseur, J., Wadsworth, F.B., Lavallée, Y., Bell, A.F., Main, I.G., Dingwell, D.B., 2015. Heterogeneity: The key to failure forecasting. Scientific Reports 5, 1–7.

Weibull, W., 1939. A statistical theory of the strength of materials. Ingvetensk. Akad. Handl. 149.

Wiemer, S., Wyss, M., 1997. Mapping the frequency-magnitude distribution in asperities: An improved technique to calculate recurrence times? Journal of Geophysical Research: Solid Earth 102, 15115–15128.

Wiemer, S., Wyss, M., 2002. Mapping spatial variability of the frequency-magnitude distribution of earthquakes. Advances in Geophysics 45.

A Brittle failure as a weak damage process

In this appendix we review the key theoretical results that find the frequency-size distribution of weak damage failure events with long-range (mean field) interactions follow a power-law distribution with a stress-dependent exponential taper. Following the formulation of Toussaint and Pride (2005), a weak damage model is specified as:

1. Regular lattice of dimension d, with N cells at locations, x.
2. Each lattice cell possess a local stress and strain, experiences isotropic elastic interactions with other cells, and is in one of two damage states: intact, $\varphi_x = 0$, or failed, $\varphi_x = 1$.
3. Homogeneous elastic moduli and homogeneous initial damage field $\varphi = 0$ at zero strain and stress.
4. Strain is progressively applied by a uniform monotonic displacement l of the external boundaries of the lattice.
5. A cell breaks at constant applied l when the reduction in total stored elastic energy, ΔE_p, due to the break exceeds the cell's breaking energy, e_x.
6. The configuration of cell breaking energies, $\{e_x\}$ is an random quenched threshold field sampled independently from a probability density function $p(x)$.
7. Stress is re-distributed from the failed cell to the other cells according to elastic interactions across the lattice.
8. Elastic interactions are assumed to be sufficiently weak that interactions between three or more cells are negligible (first Born approximation). This is valid whenever the stress change due to a failed cell is much less than the mean lattice stress.

The elastic potential energy, E_p, of this system is

$$\begin{aligned} E_p[\varphi, l] &= (C_0 + C_1 + C_2)\, l^2, \\ C_0 &= N, \\ C_1 &= -c \sum_x \varphi_x, \\ C_2 &= -\epsilon \sum_{x,y} J_{xy\varphi_x\varphi_y}, \end{aligned} \tag{36}$$

where c is a constant in the range $0 < c \leq 1$ that describes the fraction of a cell's energy reduced by its failure, ϵ is a constant in the range $0 < \epsilon \ll c$ that determines the mean strength of stress interactions between cells, and J_{xy} are linear coupling constants for stress redistribution between cells at positions x and y when at least one of these cells has failed. This energy state does not depend on the prior sequence of failures, but only on the current failure configuration, φ, and the applied relative displacement, l.

For $J_{xy} = 0$, failed cells transfer stress to all other cells in a global load sharing model. Local load sharing models correspond to $J_{xy} \neq 0$. For nearest-neighbour local load sharing, $J_{xy} \sim 1$ for nearest neighbour xy cell pairs but otherwise $J_{xy} = 0$. For elastic load sharing, $J_{xy} \sim (\ell/|x-y|)^d$, where ℓ is the lattice cell size. However, if elastic load sharing is mediated via cells connections to an elastic plate, in which case $d = 2$ and $J_{xy} \sim (\ell/|x-y|)$.

As the applied relative displacement, l, is monotonically increased, the evolution of damage follows Griffiths principle. For a system in damage state φ^F under displacement l, the cell at location x will fail if the release in potential energy, E_p, under constant l is equal to the surface energy cost of this failure. This means:

$$\Delta E_p[\varphi^F, l, x] = e_x, \tag{37}$$

where

$$\Delta E_p[\varphi^F, l, x] = (C_1 + C_2)\, l^2. \tag{38}$$

If this single cell fail occurs, then the damage state advances from φ^F to φ^E through the inclusion of x in the list of failed cell locations.

While the external displacement, l, is kept constant, there will be further failure due to stress transferred from the previous failure if there is some intact cell y such that

$$\Delta E_p[\varphi^E, l, x] \geq e_y. \tag{39}$$

If more than one cell location meets this failure criterion, then the cell that maximizes the potential energy reduction fails next (first Born approximation). This process continues under constant l until the failure configuration is stable. Then the cycle repeats by increasing l until the next cell fails according to (37). This cascading failure process yields a probability distribution of failure sizes that evolves with the external strain load. These energy-based failure criteria could equivalently be expressed as stress-based failure criteria.

Within the weak damage model, the failure size distribution depends on the interaction strength relative to the threshold disorder, and the range of these interactions. For weak or infinite range interactions (mean field)

this weak damage model becomes equivalent to a percolation model. For non-negligible, nearest-neighbour interactions the damage model becomes an Ising model, whereas if interactions decay as an inverse-power law of separation it becomes a fully-interacting Ising model (Gould and Tobochnik, 2010) otherwise named the Curie-Weiss model (Kac, 1968).

One possible physical realization of a weak damage model is the fibre bundle model, such as a set of N elastic beam fibers are connected between two elastic half spaces (Figure 32). The relative shear displacement of these half-spaces, l, controls the external shear strain that loads the fibers. As fibers break, elastic interactions between fibers occur via the elastic half-spaces. The assumption of weak damage process is satisfied if the elastic half-spaces are much stiffer than their connecting fibers.

Another possible realization is the slider-block model limited to the first failures of each lattice site and in the mean field limit this model is equivalent to the global load sharing fiber bundle model (Sornette and Physique, 1992). The distribution of simultaneous fiber failures within a global load sharing fiber bundle model is known analytically (Hemmer and Hansen, 1992; Hansen and Hemmer, 1994; Kloster et al., 1997; Pradhan, 2010).

A.1 Fiber bundle model with global load sharing

Analytic solutions for the failure size distribution exist for fiber bundle models under monotonic strain loads with global load sharing (Hemmer and Hansen, 1992; Hansen and Hemmer, 1994; Kloster et al., 1997; Pradhan, 2010). External relative displacement, l, of the fiber ends creates an applied fiber stress, σ. The quenched random distribution of fiber failure stress thresholds is defined by the probability density $p(\sigma)$ and the associated cumulative distribution function, $P(\sigma)$. For any $p(\sigma)$ distribution with a single mode, failures of size Δ occurring within the load interval $(0, \sigma)$ are dis-

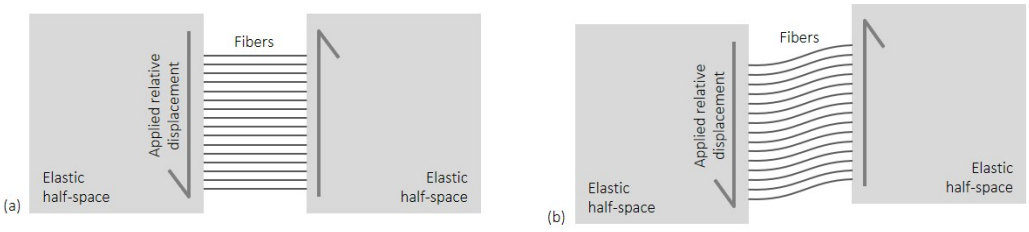

Figure 32: Representation of brittle failures on a pre-existing fault under an external shear load as a fiber-bundle model.

tributed as $D(\Delta)$ such that (Pradhan, 2010, equation 147).

$$\begin{aligned} \frac{D(s,\sigma)}{N} &= C_1 \Delta^{-\frac{5}{2}} e^{-\frac{1}{2} m'(\sigma_c)^2 \frac{\Delta}{\Delta_\zeta}} \\ \Delta_\zeta &= (\sigma_c - \sigma)^{-\frac{1}{2}} \end{aligned} \tag{40}$$

where σ_c is the critical load corresponding to peak stress within the fiber bundle where σ_c solves the equation

$$p(\sigma_c)\sigma_c = 1 - P(\sigma_c), \tag{41}$$

and $m(\sigma)' = dm(\sigma)/d\sigma$, and $m(\sigma)$ is a function of the quenched random threshold distribution such that:

$$m(\sigma) = 1 - \frac{\sigma p(\sigma)}{1 - P(\sigma)}, \tag{42}$$

and C_1 is a constant of threshold distribution defined as

$$C_1 = \frac{\sigma_c p(\sigma_c)^2}{\sqrt{2\pi}(\sigma_c p'(\sigma_c) + 2p(\sigma_c)}. \tag{43}$$

This is a power-law distribution with an exponential taper characterised by two universal constants. At the critical state, $sigma = \sigma_c$, this distribution is a pure power-law, $\Delta^{-\frac{5}{2}}$, with a universal exponent of 5/2. Below this critical state, $\sigma < \sigma_c$, the stress-dependent exponential taper has a characteristic scale, Δ_ζ that varies as an inverse power-law of $\sigma_c - \sigma$ with a universal exponent of 1/2. Both of these constant do not depend on the particular choice of the threshold distribution, $p(\sigma)$, so long as it has a single maximum. This distribution is insensitive to the choice of threshold distribution conditional on this distribution yielding a single maximum in the average total force acting on the fiber bundle under monotonic strain loading.

At the critical point $\sigma = \sigma_c$, this distribution reduces to the pure power-law $\propto \Delta^{-\frac{5}{2}}$. The burst-size distribution for the next burst due to further strain loading from a stable configuration under load ϵ is (Pradhan, 2010, equation 175).

$$\begin{aligned} \frac{D(s,\sigma)}{N} &= C_2 \Delta^{-\frac{3}{2}} e^{-\frac{1}{2} m'(\sigma_c)^2 \frac{\Delta}{\Delta_\zeta}} \\ \Delta_\zeta &= (\sigma_c - \sigma)^{-\frac{1}{2}}, \end{aligned} \tag{44}$$

where C_2 is a different constant of threshold distribution defined as

$$C_2 = \frac{p(\sigma_c) m'(\sigma_c)}{\sqrt{2\pi}}. \tag{45}$$

This is a power-law distribution with an exponential taper characterised by two universal critical exponents; 3/2 defines the power-law scaling and 1/2 describes the inverse power-law stress dependency of the exponential taper. For some special cases of fiber stress threshold distributions the value of the universal power-law exponent depends on the details of the threshold distribution (Harris and Bourne, 2019).

A.2 Fiber bundle model with local load sharing

The global load sharing mechanism between surviving fibers is a simplification, as nearby fibers are more likely to carry most of the re-distributed load. Kloster et al. (1997) developed a theoretical solutions in the limit of nearest-neighbour load sharing in one dimension. This results in a failure size distribution that only approximates a pure power-law for sufficiently small failure sizes, and with a non-universal exponent that is larger than for global load sharing models and increases with the size of the system. The maximum load, F, prior to complete failure of the system also scales with the initial number of fibers, N, such that $F \propto N/\log N$. Local load sharing mechanisms do therefore create the possibility of further complexity in the frequency-magnitude distributions response to increasing external loads. In this example, the power-law exponent remains stress-invariant, but becomes scale-dependent. This possibility of greater complexity motivates us to test a wide variety of alternative earthquake magnitude distribution models for the Groningen field.

B Brittle failure as a percolation process

In this appendix we review the key theoretical results map brittle failure processes with negligible neighbour interactions onto a percolation process to find the frequency-size distribution of percolation cluster failure events follow a power-law distribution with a stress-dependent exponential taper.

When the variability in strength thresholds is much larger than the stress transfers from a failed cell to the surrounding cells due to elastic interactions the failure process is governed by the weakest cell first mechanism. Under these conditions of infinite threshold disorder, brittle failure is equivalent to a stochastic percolation process (Roux et al., 1988).

In this case, the probability distribution of failure sizes follows the distribution of percolation cluster sizes. This connection provides some general insights into the physical processes governing the form of the frequency-magnitude distribution of acoustic emissions and its evolution with increas-

ing probability of failure under increasing stress. This percolation problem can be solved analytically for processes embedded in a space with one dimension ($d = 1$) space, or in an infinite number of dimensions ($d = \infty$) within a Bethe lattice (*e.g.* Stauffer and Aharony, 1994).

B.1 Percolation in 1D

Starting with a 1D percolation process, where there is just a single geometric configuration for each scale of failure, the probability, $n_s(p)$ of failure size s occurring is

$$\begin{aligned} n_s(p) &= (p_c - p)^2 p^s \\ &= (p_c - p)^2 e^{s \log p} \\ &= (p_c - p)^2 e^{-\frac{s}{s_\zeta}} \end{aligned} \tag{46}$$

where p is the independent probability of failure within a single cell and the percolation probability $p_c = 1$. Within this system, the frequency-size distribution is just an exponential taper reflecting the simple multiplicative decline in probability with increasing failure size. The characteristic scale of this taper depends on the single-cell failure probability, p, such that $s_\zeta = -1/\log p$. The probability threshold for an infinitely extended percolation cluster is $p_c = 1$ since any intact cells will terminate the cluster. As the percolation threshold is approached, $p \to p_c$, the characteristic scale of the exponential taper diverges, $s_\zeta \to \infty$. Rewriting $\log p$ as $\log(1-(p_c-p))$ and approximating with the Taylor expansion around $p = p_c$ leads to the inverse power-law, $s_\zeta = (p_c - p)^{-1}$, with a universal exponent of 1. As failure probability will scale with stress or strain, the presence of a stress-dependent exponential taper within the failure-size distribution arises simply from the exponentially declining probability of larger collections of independent failures.

B.2 Percolation in many dimensions

In higher dimensions, the number of configurations of possible failure geometries increase rapidly with the size of the failure (Figure 33), so we may write a general expression for the cluster size distribution as

$$n_s(p) = \sum_t g_{s,t}(1-p)^t p^s, \tag{47}$$

where $g_{s,t}$ is the number of different lattice configurations, known as lattice animals, with size s (cluster area) and perimeter t. Now, the probability of larger failure clusters occurring, $n_s(p)$, depends on the competition between

the growth of alternative failure configurations and the exponential decline in the probability of collective failure. Ultimately, for sufficiently large failures, the exponential taper must dominate to ensure stability and a normalizable probability distribution, $n_s(p)$. Nonetheless, the body of this distribution may exhibit a much slower initial monotonic decline due to the population growth of lattice animals delaying the onset of the exponential tail. Another way to view this process, is that although larger failures are exponentially less probable, their larger external boundaries offer more possibilities for at least one more failure to occur. Counting lattice animals, becomes immensely difficult with increasing cluster size and percolation dimensions (Luther and Mertens, 2011). Nonetheless, some general bounds on any power-law scaling prior to the exponential tail are possible.

For $p < p_c$, the probability of a site failing is equivalent to the probability of that site being any of the sites within a finite cluster of any size, so

$$p = \sum_{s=1}^{\infty} s n_s(p) \text{ for } p < p_c. \tag{48}$$

Likewise, the probability, p_s of a given failed site being connected to a cluster of size, s, is

$$p_s = \frac{s n_s(p)}{p}. \tag{49}$$

consequently, the mean size of these clusters is

$$S(p) = \sum_{s=1}^{\infty} p_s s \tag{50}$$

Combining these last three results means

$$S(p) = \frac{\sum_{s=1}^{\infty} s^2 n_s(p)}{\sum_{s=1}^{\infty} s n_s(p)}. \tag{51}$$

By definition, as $p \to p_c$, then $S(p) \to \infty$, which in turn requires the numerator to diverge faster than the denominator. This requirement is satisfied by a general power-law scaling at the percolation threshold:

$$n_s(p_c) \propto s^{-\tau}, \tag{52}$$

for sufficiently large s such that the divergent numerator becomes

$$\sum_{s=1}^{\infty} s^{2-\tau} = \infty \tag{53}$$

This geometric progression only diverges if $2 - \tau \geq -1$, which establishes an upper bound on the power-law exponent of $\tau \leq 3$ to ensure an infinite cluster appears at the percolation threshold.

Similarly, below the percolation threshold, a lower bound exists from the requirement that a failed site must belong to a finite cluster. Rewriting (48) using $n_s(p) \propto s^{-\tau}$ means

$$\sum_{s=1}^{\infty} s^{1-\tau} = p. \tag{54}$$

This geometric progression only converges if $1 - \tau < -1$ meaning $\tau > 2$. Combining both bounds limits τ to the range

$$2 < \tau \leq 3. \tag{55}$$

At the percolation threshold, the percolating cluster geometry is a random fractal where the fractal dimension measured by the box-counting method is a non-integer (Stauffer and Aharony, 1994). Clusters above the percolation threshold are not fractal. Below the percolation threshold, the finite clusters are fractal on length-scales up to the correlation length-scale of the clusters. The associated fractal dimension, d_f, of these clusters is a universal constant that scales with τ as (Stauffer and Aharony, 1992)

$$\tau = 1 + \frac{d}{d_f}, \tag{56}$$

where d is the number of dimensions of the embedding space such that $d \geq d_f$. This is consistent with the lower bound, $\tau > 2$.

To connect this result back to the distribution of seismic moments, we first map the number of sites in the cluster to the seismic slip area, A, such that probability density distribution of slip area follows as

$$p(A) \propto A^{-\tau} dA. \tag{57}$$

Then, from the definition of seismic moment, $s = \mu A u$, where μ is the shear modulus, and u is the mean seismic slip, we see the distribution of seismic moments depends on the distributions of slip area and mean slip. In general, the mean slip scales as $u \propto A^{\alpha}$. In fracture mechanics, a circular crack with constant stress drop has a mean slip that scales with crack length, such that $\alpha = \frac{1}{2}$. Correspondingly, seismic moments scale with slip area as $s \propto A^{1+\alpha}$, so that:

$$p(A) \propto A^{-\tau} dA \propto s^{-\frac{\tau}{1+\alpha}} dA \propto s^{-\frac{\tau+\alpha}{1+\alpha}} ds \propto p(s). \tag{58}$$

Integration of this probability density leads to a survival function of the form

$$P(> s) \propto \int p(s) ds \propto \int s^{-\frac{\tau+\alpha}{1+\alpha}} ds \propto s^{-\frac{\tau-1}{1+\alpha}}, \tag{59}$$

and comparison with (3) shows, the power-law exponent for the distribution of seismic moments is

$$\beta = \frac{\tau - 1}{1 + \alpha}. \tag{60}$$

The upper and lower percolation bounds on τ given by (55), place bounds on β as

$$\frac{1}{1+\alpha} < \beta \leq \frac{2}{1+\alpha}. \tag{61}$$

For $\alpha = 1/2$ this means

$$\begin{aligned} \frac{2}{3} <& \beta \leq \frac{4}{3}, \\ 1 <& b < 2. \end{aligned} \tag{62}$$

The particular case of the lower bound, $\tau = 2$, corresponds to the usually observed value of $\beta = 2/3$.

King (1983) proposed an alternative relationship between β and the fractal dimension, d_f, of the active fault network geometry:

$$\beta = \frac{d_f}{d}, \tag{63}$$

This implies a more restrictive upper bound $\beta \leq 1$. However, King (1983) obtains (63), under the implicit assumption that all faults within the fractal fault network acquire their slip in single earthquake events. This one earthquake to one fault assumption means the frequency distribution of fault sizes determines the frequency distribution of earthquake sizes. However, an individual fault may host multiple earthquakes with a distribution of various seismic moments that sum to the total fault slip distribution. In this way, the distribution of earthquake sizes may not necessarily be equal to the distribution of fault sizes. This means the fractal dimension of fault network geometry, d_f, does not necessarily a strong constraint on the β-value of the seismic moment distribution.

`...A distribution of asperities over a fault network subject to rate and state frictional failures leads to a power-law distribution of failure sizes (Dublanchet et al., 2013)`

...I guess not entirely though. There is quite a good correlation of exponents for acoustic emissions and measured fracture lengths in Hatton, C.G., I.G. Main & P.G. Meredith (1993. A comparison of seismic and structural measurements of fractal dimension during tensile subcritical crack growth, J. Struct. Geol. 15, 1485-1495), just not an exact equivalence in the exponents.

...Hatton et al. (1993) showed there is some constraint, just not a straightforward equivalence.

B.3 Percolation in a Bethe lattice

In a Bethe lattice each site has z neighbours (Figure 33). For $z = 2$, the Bethe lattice reduces to a 1D lattice. Due to the branching structure, there are no closed loops of connected neighbours. Within any Bethe lattice there is a unique perimeter size t for a given cluster size s, and from inspection of Figure 33 we see that,

$$t = (z - 2)s + 2. \tag{64}$$

For large s the ratio of perimeter to cluster size is a constant, $t/s = z - 2$. A Bethe lattice shares these properties of no closed loops and a constant perimeter-size ratio within hyper-cube lattices in the limit $d \to \infty$.

The percolation threshold within a Bethe lattice also takes a simple form

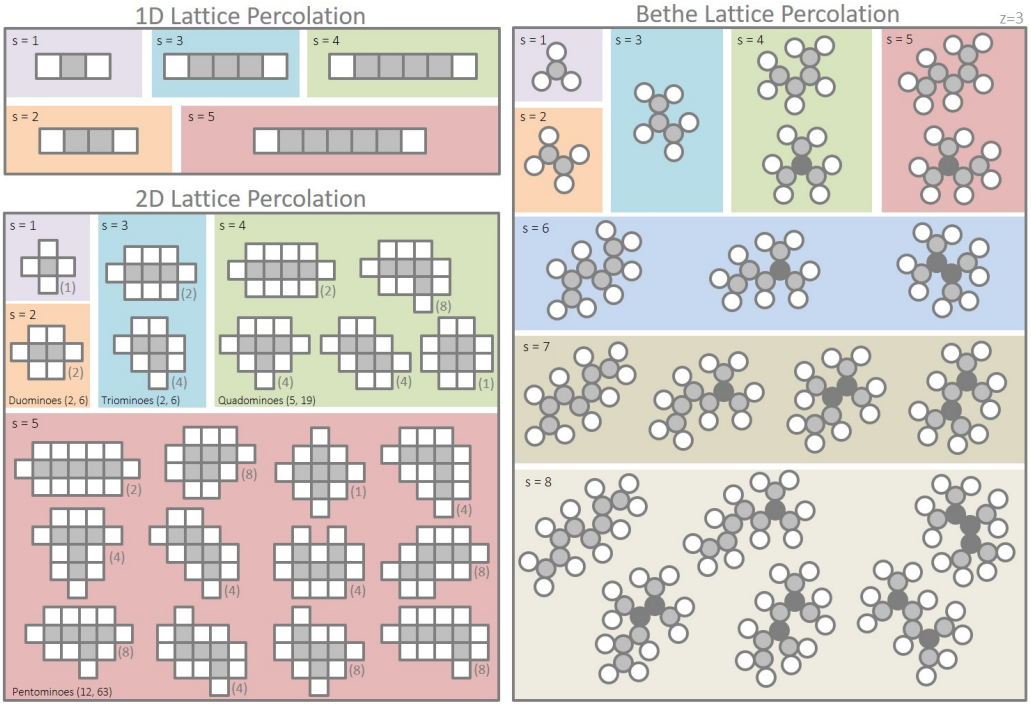

Figure 33: Illustration of percolation cluster geometries as a function of cluster size, s, for (a) 1D lattice percolation, (b) 2D lattice percolation, and (c) Bethe lattice percolation with a coordination number, $z = 3$. The number of alternative geometric configurations increases rapidly with the scale of failure for all except 1D percolation. Grey denotes the cluster of failed cells, white denotes the external boundary cluster of intact cells, and within the Bethe lattice, dark grey cells denotes failed cells surrounded by other failed cells to help distinguish the different geometries.

as a cluster may only extend to infinity if at least one of the sites connected to a failed site is also failed meaning $p_c(z-1)=1$, and so

$$p_c = \frac{1}{z-1}. \tag{65}$$

Because determining $g_{s,t}$ for large s is so difficult, let us avoid this by considering the cluster number probability, $n_s(p)$, relative the cluster number probability at the percolation threshold, $n_s(p_c)$. Combining (47), (64), and (65) this leads to

$$\frac{n_s(p)}{n_s(p_c)} = \left(\frac{1-p}{1-p_c}\right)^2 e^{-\frac{s}{s_\zeta}} \tag{66}$$

such that

$$\frac{1}{s_\zeta} = -\log\left(\frac{p}{p_c}\left(\frac{1-p}{1-p_c}\right)^{z-2}\right). \tag{67}$$

Taylor expansion of the function appearing inside the logarithm, $f(p)$, about the percolation threshold, $p=p_c$, which involves $f(p_c)=1$, $f'(p_c)=0$, and $f''(p_c)=-8$, and then using (65) and the approximation $\log(1+f(p))=f(p)$ leads to the result

$$s_\zeta = \frac{1}{4}(p_c-p)^{-2} \text{ as } p \to p_c. \tag{68}$$

The characteristic size of the exponential taper, s_ζ scales with the failure probability, p, as an inverse power-law, $(p_c-p)^{-2}$ with a universal exponent of 2. Combining (52) with the exponential taper appearing in (66) means the general form of the solution is:

$$n_s(p) \propto s^{-\tau} e^{-\frac{s}{s_\zeta}}, \tag{69}$$

where τ is still to be determined.

Previous general arguments about the mean cluster size, $S(p)$, placed bounds on τ given by (55). Within a Bethe lattice, the mean cluster size, $S(p)$, takes a simple exact form. Starting with a failed site at the origin and representing the average length of connected failed sites along each lattice branch leading away from the origin as T, it follows that

$$S(p) = 1 + zT. \tag{70}$$

As all sites are geometrically equivalent within an infinite Bethe lattice, this symmetry means T may be expressed as the failure probability of the first site in the chain multiplied by the average number of connected failed sites from this point along the chain. *i.e.*

$$T = p(1+(z-1)T). \tag{71}$$

Solving for T and combining with (65) and (70) yields

$$S(p) = \frac{1+p}{1-\frac{p}{p_c}} = (1+p)p_c(p_c-p)^{-1}. \tag{72}$$

As expected, if site failure probabilities increase towards the percolation threshold, $p \to p_c$, the mean cluster size diverges, according to an inverse-power law, $S(p) \sim (p_c - p)^{-1}$, with a universal scaling exponent of 1.

From (51) the mean cluster size may also be expressed as

$$\begin{aligned} S(p) &\propto \sum_{s=1}^{\infty} s^2 n_s(p) \\ &\propto \int_1^{\infty} s^{2-\tau} e^{-\frac{s}{s_\zeta}} ds \\ &\propto s_\zeta^{3-\tau} \text{ for } p \to p_c \end{aligned} \tag{73}$$

Substituting this result into (68) and equating with the previous result (72) means

$$S(p) \propto (p_c - p)^{2\tau-6} \propto (p_c - p)^{-1}, \tag{74}$$

which requires

$$\tau = \frac{5}{2}. \tag{75}$$

This is identical to the power-law exponent of the asymptotic distribution of failure sizes within the equal load sharing class of fibre bundle models, as expected given their isomorphism (Toussaint and Pride, 2005). The Bethe lattice percolation model of brittle failure predicts earthquake seismic moments will be distributed as a power-law with an exponential taper where the power-law exponent, β, is the constant given by (60) and (75).

C Poro-elastic thin-sheet model inference

Figure 34 shows the marginal posterior distributions of the poro-elastic thin-sheet intra-reservoir stress model parameters defined in section5.

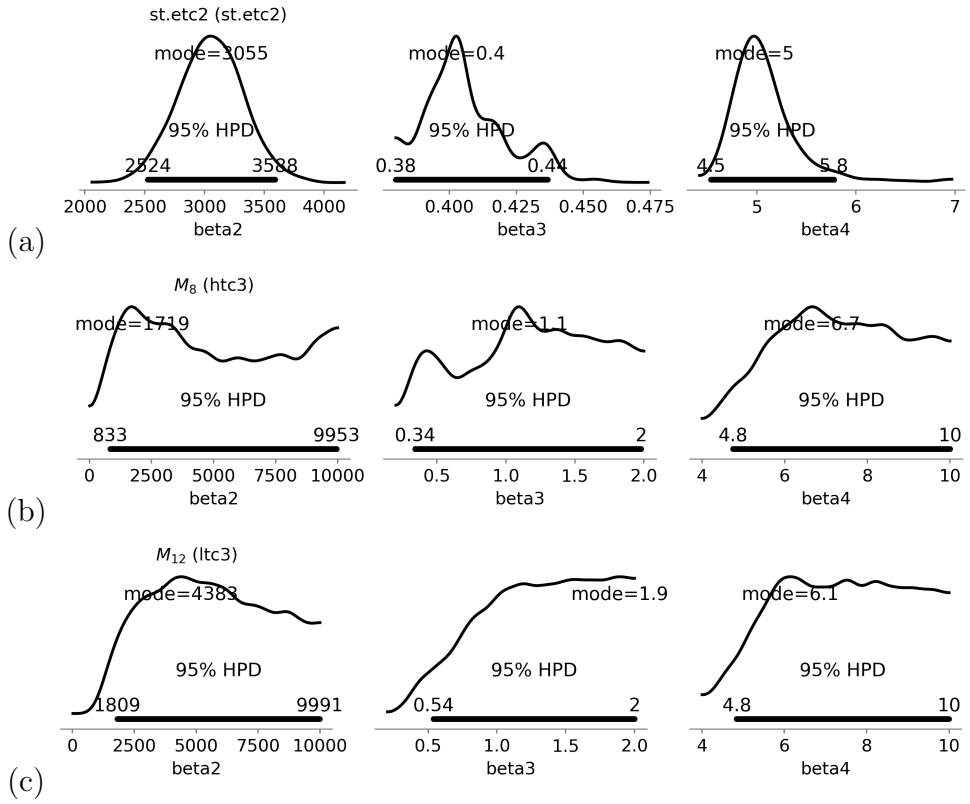

Figure 34: Marginal posterior distributions of the the poro-elastic thin-sheet intra-reservoir stress model parameters defined in section5 obtained in combination with (a) the extreme threshold failures model for space-time distribution of earthquake occurrence (st.etc2), (b) the stress-dependent β-model of earthquake magnitudes (M_8, htc3), and (c) the stress-dependent ζ-model of earthquake magnitudes (M_{11}, ltc3).